UCLA
UCLA Electronic Theses and Dissertations

Title

Performance-Based Design and Assessment of Controlled Rocking Steel Braced Frames

Permalink

Author

Dastmalchi, Shahrzad

Publication Date

2020

Peer reviewed|Thesis/dissertation

UNIVERSITY OF CALIFORNIA

Los Angeles

Performance-Based Design and Assessment of Controlled Rocking Steel Braced Frames

A dissertation submitted in partial satisfaction of the

requirements for the degree Doctor of Philosophy

in Civil Engineering

by

Shahrzad Dastmalchi

2020

ABSTRACT OF THE DISSERTATION

Performance-Based Design and Assessment of Controlled Rocking Steel Braced Frames

by

Shahrzad Dastmalchi

Doctor of Philosophy in Civil Engineering

University of California, Los Angeles, 2020

Professor Henry V. Burton, Chair

Controlled rocking steel braced frames (CRSBFs) have been developed with the goal of minimizing the post-earthquake impact of primary building functions. While there has been significant research to date to demonstrate the viability of the CRSBF as a high-performance system, much less has been accomplished in the development of performance-based design and assessment methods. This research is focused on developing models, tools and techniques for practicing engineers to analyze, design and assess the performance of CRSBFs. To avoid the computational expense of nonlinear response history analyses, an approximate method is formulated to estimate the CRSBF drift demands using the primary design parameters. Additionally, a reliability-based methodology for establishing the load and resistance factors for the force-controlled (braced frame) members is formulated. A key departure from previously developed capacity design approaches is the development of an explicit link between the effect of the failure of the force-controlled components and system level performance limit states (collapse and post-earthquake structural safety). The results from a case study applied to 3-, 6- and 9-story building cases show that the effect of force-controlled components is more significant for the collapse limit state compared to post-earthquake structural safety. Also, even when the resistance to load factor ratio (ϕ/γ) is increased to 1.8, the 50-year collapse probability remained below the 1% threshold prescribed by current

building codes. The effect of record-to-record and modeling uncertainty on the seismic response and performance assessment of CRSBFs is also studied. The results showed that the impact of modeling uncertainty on seismic performance increases with the building height. To enable practitioners to estimate the service life costs of potential designs, surrogate models are developed to assess earthquake-induced life cycle economic loss and environmental impacts. The effectiveness of the surrogate models is demonstrated by evaluating their accuracy on "unseen" (i.e., not used in the development of the surrogate models) designs.

The dissertation of Shahrzad Dastmalchi is approved.

John Wright Wallace

Ertugrul Taciroglu

Thomas Sabol

Henry V. Burton, Committee Chair

University of California, Los Angeles

2020

iv

To my family …

For their endless love, support and encouragement

Table of Contents

List of Tables

List of Figures

2001-2006   B.Sc. in Civil Engineering, Iran University of Science and Technology, Tehran, Iran

2006-2008   M.Sc. in Earthquake Engineering, University of Tehran, Tehran, Iran

2012-2014   M.Sc. in Structural Engineering, University of Maryland, College Park, Maryland

2014-2020   PhD Candidate in Structural Engineering, University of California Los Angeles

CHAPTER 1:   Introduction

1.1.   Motivation and Background

The vision for the next generation of buildings located in high seismic regions is that they are designed and constructed such that they can continue to provide their primary functions (e.g., safe shelter and critical operations) after a major earthquake. Several research programs have been directed towards developing high-performance systems that minimize structural damage and the resulting repair costs and downtime after an earthquake. One such category of seismic systems uses rocking action to resist earthquake effects. Enhanced performance is achieved through controlled rocking and self-centering of the lateral force resisting system, limiting structural damage to easily replaceable elements that provide energy dissipation through inelastic deformation.

The controlled rocking steel braced frame (CRSBF) has been the subject of numerous research investigations. Its predictable response and viability as a high-performance structural system has been demonstrated through component- and system-level physical experiments [e.g. Eatherton and Hajjar, 2010; Ma et al. 2011; Wiebe et al. 2013]. The effect of design parameters such as the aspect ratio, response modification factor and initial post-tensioning force has also been examined using numerical simulations [Hall et al. 2010; Eatherton and Hajjar, 2011; Steele et al. 2017; Moradi and Burton, 2018]. To enable its implementation in industry building projects, design methodologies and simplified analysis procedures for CRSBFs have been developed [e.g. Eatherton et al. 2014; Wiebe and Christopoulos, 2014; Steele and Wiebe 2016; Roke et al. 2010].

Despite the research that has been done on controlled rocking systems to date, there are a number of questions related to their design and assessment that have not been addressed. An

example of such an issue is the lack of availability of robust methods for estimating the maximum story drift demands in controlled rocking systems under different levels of earthquake shaking. This is a critical step in the design process, as the maximum story drift demand is strongly correlated with the extent of damage to both structural and non-structural systems. Another unresolved issue that is relevant to the design process is determining the appropriate demand-levels for sizing force-controlled components. The enhanced performance of the controlled rocking system is contingent on the elastic (or near elastic) response of the frame. As such, these force demands have strong implications to the overall performance of the system. The effect of key design variables (e.g. initial post-tensioning force, fuse strength, aspect ratio) and model uncertainty on seismic performance of CRSBFs has also never been studied. Also, strategies for achieving optimal designs of CRSBFs have not yet been developed. The proposed research will address the previously outlined questions towards the goal of establishing performance-based design and analysis criteria for CRSBFs.

1.2.   Objectives

The main goal of the proposed research is to develop the models and methods for performance-based design and assessment of controlled rocking steel braced frames. The detailed objectives are listed as follows:

1. Develop simplified analysis methods for estimating maximum story drift demands which are implementable in the context of engineering practice.

2. Determine the relationship between the key structural parameters and earthquake-induced losses in controlled rocking steel braced frames and use them to construct surrogate models for predicting the earthquake-induced impacts and develop performance-based optimal designs.

2

3. Examine the influence of modeling uncertainty on the seismic response and multi limit-state (i.e., immediate occupancy, reparability and collapse prevention) performance of CRSBFs .

4. Formulate a reliability-based methodology to study the effect of force-controlled component (beams, columns, and braces) failure on the overall performance of the controlled rocking steel braced frames (vulnerability- and risk-based assessments of the collapse and UPT) towards establishing load and resistance factors to be used for capacity design.

1.3. Organization and Outline

The main body of the current study consists of five chapters and the content of each chapter is elaborated below:

Chapter 2 presents a literature review, which summarizes previous experimental and numerical studies on controlled rocking braced frames, and previously developed approaches to estimating the seismic response of the structure.

Chapter 3 provides a summary of the design procedure for controlled rocking braced frames and a description of the prototype buildings used throughout the study.

Chapter 4 illustrates the numerical modeling approach for controlled rocking steel braced frames, which is verified using the results from large scale experiments.

Chapter 5 proposes predictive equations for estimating the median engineering demand parameters for controlled rocking steel frames.

Chapter 6 presents a reliability-based approach to determining the demand and capacity factors used to design the force-controlled components (braced frame elements) of CRSBFs.

Chapter 7 investigates the effect of record-to-record and modeling uncertainties on the seismic response and performance of the controlled rocking braced frames.

Chapter 8 investigates the effect of different design parameters on the seismic performance of CRSBFs and develops surrogate models for predicting earthquake-induced life cycle economic losses and environmental impacts (energy consumption and greenhouse gas emissions).

Chapter 9 summarizes the findings of the previous chapters and presents some ideas for potential future work.

CHAPTER 2:   Literature Review

2.1. Experimental and Numerical Studies on Rocking Structures

The dynamic behavior of a rigid block as an inverted pendulum was first studied by Housner (1963). He investigated the behavior of the SDOF block under horizontal excitations such as sine pulses and earthquake motions. He derived the analytical solution for the equations of motion that govern the response of the rigid block without considering sliding between the base and the bock.

Experimental and analytical responses of a three-story steel moment frame with and without column uplift was investigated by Clough and Huckelbridge (1977). Figure 2.1 shows the experimental setup of the rocking specimen. Two roller bearings aside of each column were used to ensure only vertical motion. Self-centering of the frame was provided by the self-weight. No PT cables or replaceable energy dissipating fuses were used.
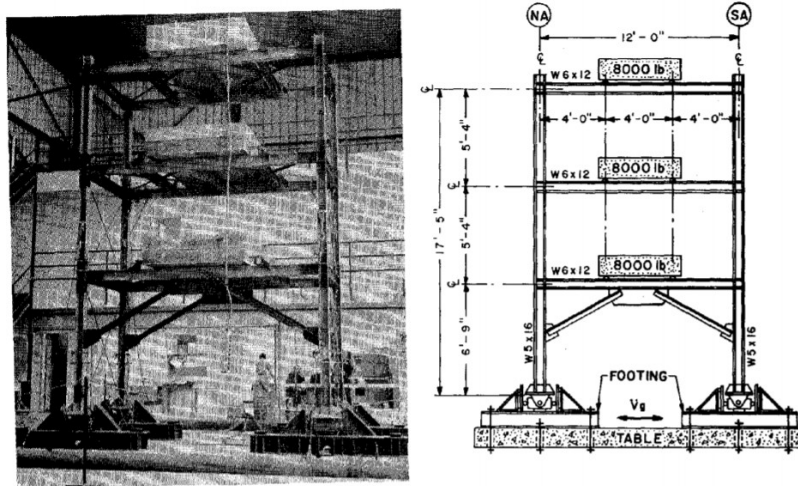
Figure 2.1. Test model by Clough and Huckelbridge (1977)

The results showed that the internal forces and maximum story drift was reduced in the frame with the uplifting columns. It was also noted that the stiffness of the impact pads beneath base columns changed the first mode period of the frame because of the contribution the higher

5

modes. The first mode period of the frame also decreased when the stiffness of the pads was increasing.

Priestley et al. (1978) verified Housner's equations for relating the between amplitude and frequency using a simple experimental model, and extended the method to predict the maximum displacement of the rocking block.

Wada (2001) used a yielding plate as an energy dissipater in the columns of a tall steel braced frame. The plate was installed in the column splices to allow rocking under enough tension and dissipate energy through yielding. A comparison between systems with conventional and the proposed joints is shown in Figure 2.2. This device limits the force in tension column and consequently reduces the compression demand on the columns and prevents collapse failure of columns.

(a)   (b)   (c)
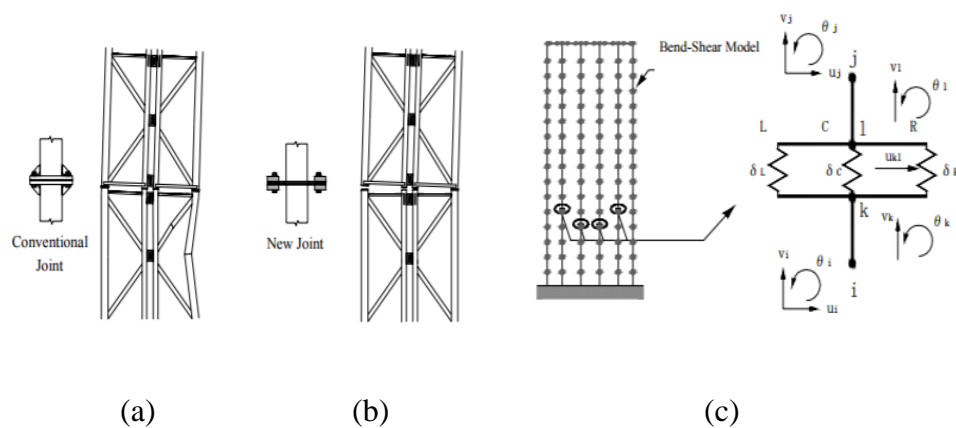
Figure 2.2. (a) Conventional joint (b) Proposed joint (c) Analytical model (Wada et al. 2001)

Another shake table test was done by Iwashita et al. (2002) with a 1/9 scale of rocking steel moment frame (Figure 2.3). The support distance was made to be adjustable to investigate different aspect ratios of 3.5 and 7. The results showed that when the column uplifted at higher ground motion intensities, the story shear force did not increase significantly.

Midorikawa et al. (2006) conducted a shake table test (½ scale) and numerical analyses of a three story steel braced frame with yielding base plate and compared the response with that

of a fixed-base frame (Figure 2.4). Two different plate thicknesses were tested for the base plate connection. The results showed that energy dissipation of the yielding base plate caused the displacement of the rocking frame and fixed frame to be almost the same. It also showed significant reduction in the story shear of the rocking frame compared to the fixed base connection. Moreover, the plate with the smaller yield strength showed more reduction in the base shear forces.

(a)   (b)

Figure 2.3. (a) Experimental model (b) Rocking base. (Iwashita et al. 2002)

(a)   (b)

Figure 2.4. (a) Rocking system with yielding base plate (b) Plan of yielding base plate (Midorikawa et al. 2006)

Pollino and Bruneau (2008) studied the retrofit of existing bridge piers by enabling rocking. Buckling restrained bars installed on the pier was used to dissipate energy and the gravity load provided the overturning resistance (Figure 2.5).
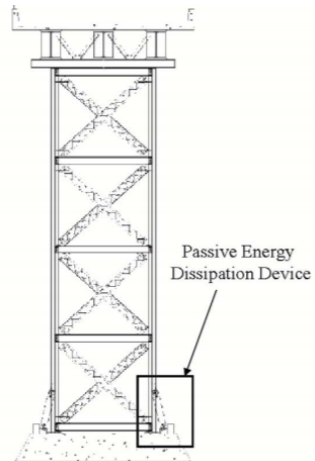
Figure 2.5. Retrofit bridge pier with energy dissipating device (Pollino and Bruneau, 2007)

Tremblay et al. (2008) examined the use of a viscous damping device between the column base and foundation. The damping element dissipated earthquake energy, which was shown to decreased the displacement demand. A ½ scale two story rocking steel braced frame with fluid damping was tested. A finite element model was also used to assess the performance of the structure (Figure 2.6). The results showed a reduction in the column uplift load and no structural damage occurred at the design ground motion level. Also, the displacement demand still remained within the acceptable code limit.
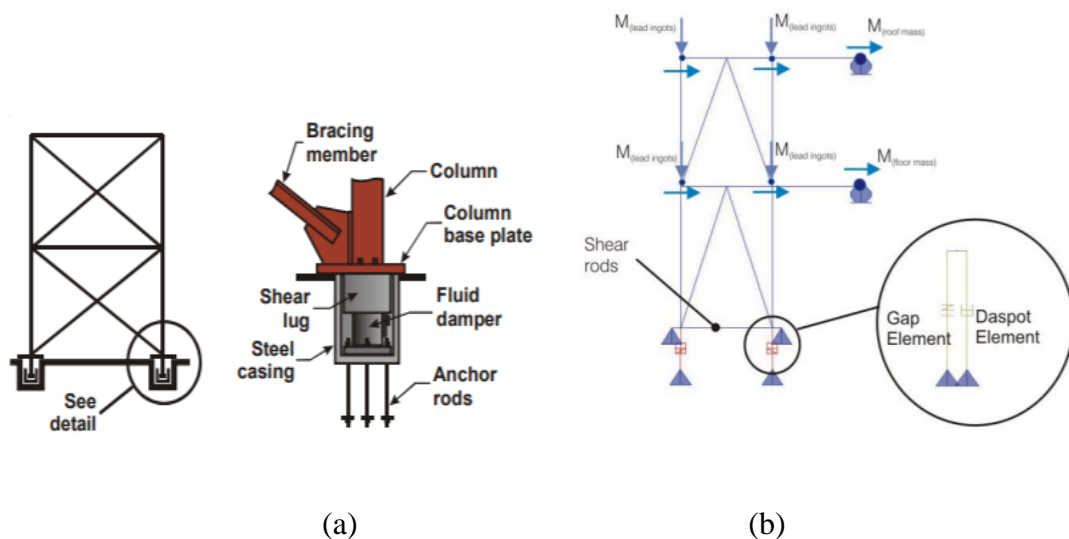
Figure 2.6. (a) Viscously damped controlled rocking steel braced frame system (b) Numerical model (Tremblay, et al. 2008)

2.2.　　　Experimental and Numerical Studies on Self-Centering Structures

Self-centering capability of rocking frames can be accomplished by post-tensioned strands which are connected to the foundation and roof level of rocking frames. Along with the dead loads on the frame, PT stands inserted at the center of the frame or at two end columns enable the structure to return to its original position and the end of its response history, thereby reducing residual drift demands during severe earthquakes. Figure 2.7 shows different configurations of the controlled rocking braced frames.

The concept of self-centering ability is illustrated in Figure 2.8. The energy dissipation parameter, β, has an inverse relationship with the self-centering ratio.
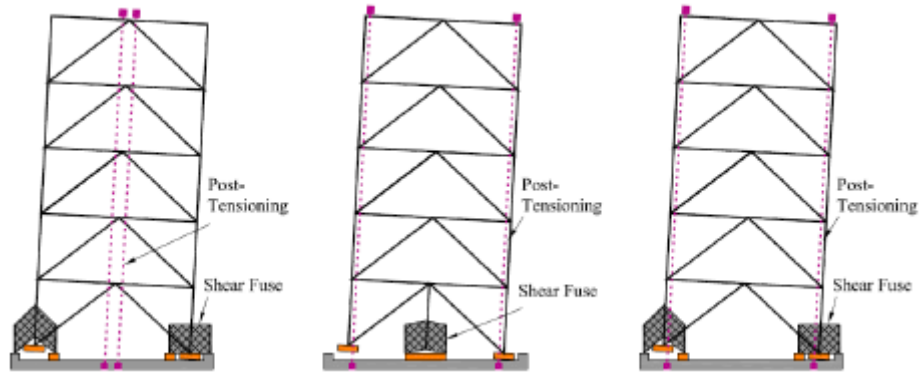
Figure 2.7. Controlled rocking steel braced frame configurations (Ma et al. 2011)
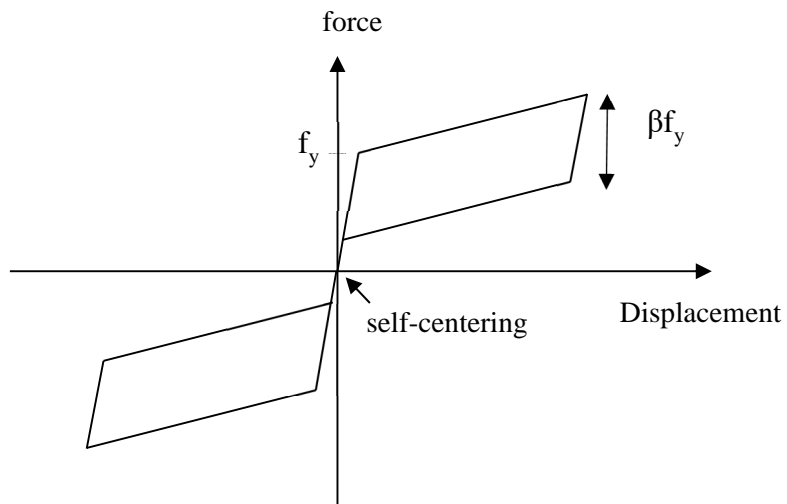
Figure 2.8. Hysteresis loop of rocking frame

Some experimental and computational studies have been performed to demonstrate the effectiveness of CRBFs (Ma et al. 2010 and Eatherton et al. 2010). A single-bay three story CRSBF was tested by Ma et al. (2010) with three types of fuses under various scaled ground motions up to the MCE level and beyond (1.25MCE). A comparison between the uplift ratio and drift demand indicates rigid body rotation of the three story CRBF. Also, the peak drift ratios were less than 2% at DBE and 3% at MCE level. There was no damage to the frame up to the MCE level, which demonstrates the capability of the CRBF to eliminate the residual drift and limit damage to the replaceable fuses.

Figure 2.9. shows the experimental specimen and numerical model in OpenSees conducted from the Ma et al. (2011) study. Eatherton et al. (2010) performed nine experiments on seven dual configurations and two single configurations of controlled rocking braced frames. Figure 2.10 shows one of the shake-table tests and the numerical model of the dual configuration controlled rocking braced frames. These results also showed no residual drift up to the MCE level and no yielding in the steel frame or post-tensioning. In other words, the inelastic response was limited to the replaceable fuse elements.

(a)

(b)

(c)

(d)
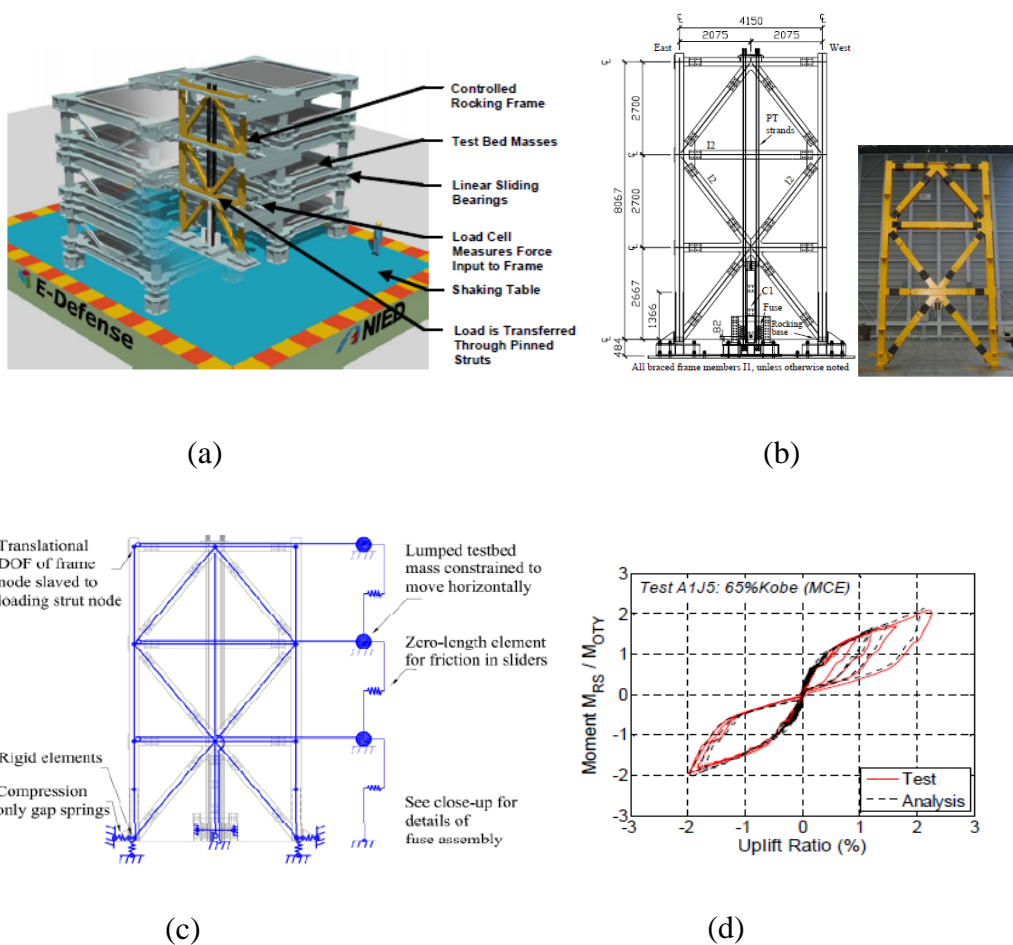
Figure 2.9. (a) 3D schematic of shake-table test (b) Braced frame specimen (c) OpenSees model (d) Hysteresis comparison of test and analyses (Ma et al. 2011)
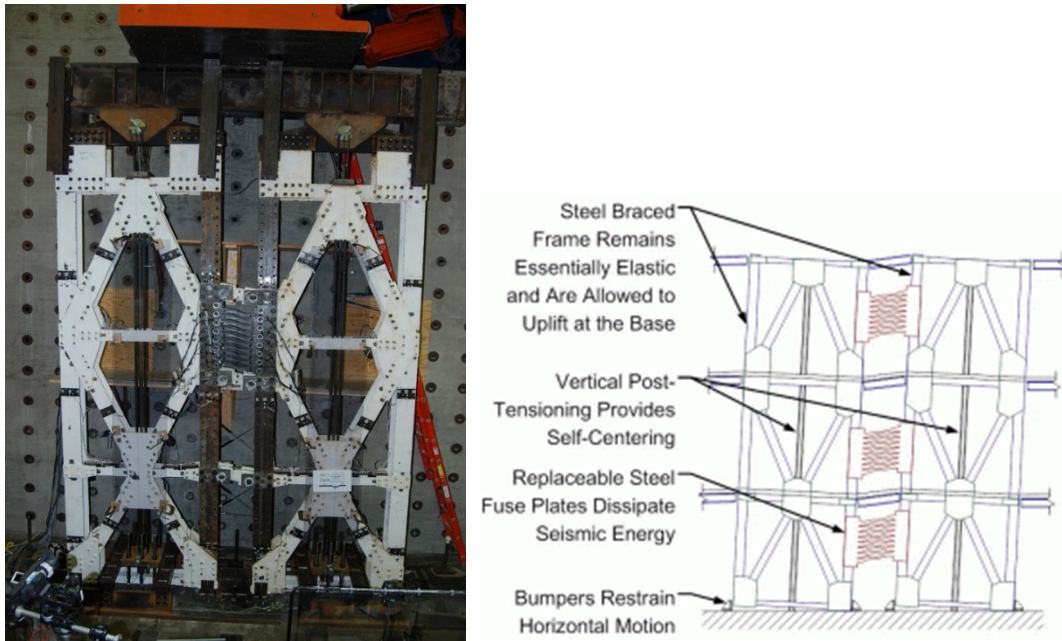
(a)

(b)
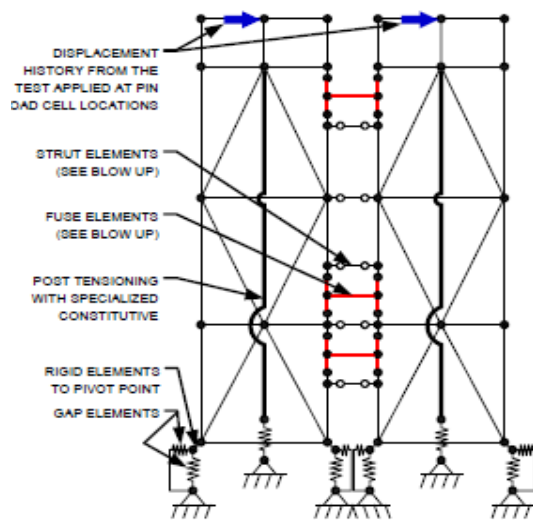
(c)
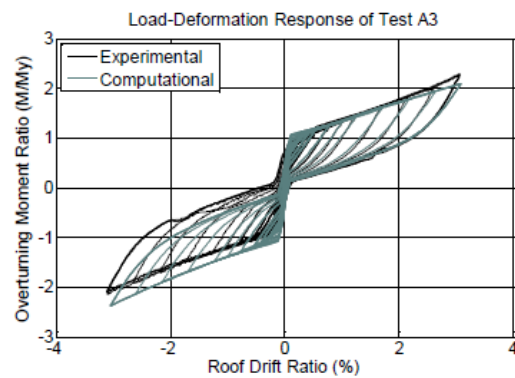
(d)

Figure 2.10. (a) Experimental specimen (b) Schematic of controlled rocking braced frame (c) OpenSees model (d) Load-Deformation response of specimen (Eatherton et al. 2011)

Wiebe and Christopoulos (2014a and 2014b) developed a performance-based design framework for CRSBFs. Single-degree-of-freedom (SDOF) idealization of the CRSBF was used to evaluate the base rocking joint with the goal of meeting a pre-defined performance objective. The study demonstrated that the contribution of higher mode effects amplifies the

member forces, and proposed using two or more joints above the base as a mitigation strategy. A shake-table test and numerical analyses were conducted on a 3/10 scale eight story CRSBF with multiple joint locations. The results showed reduced variability in peak seismic force demands which lead to improved capacity design of the frame.

2.2.1. Frame member design

Prior research has developed methods to predict the design forces of the CRBF members. Ma et al. (2010) developed an approach to estimate the shear force distribution along the frame height based on the prediction of maximum displacement. Eatherton and Hajjar (2010) developed a procedure based on multiple lateral load distributions along the height of the building to account for contribution of higher mode effects. The resulting member forces were conservative relative to those obtained from other lateral load distributions combined with the maximum PT and fuse forces applied to the frame. Roke et al. (2010) used the complete quadratic combinations (CQC) of member forces and derived a modification factor based on statistical analysis.

Steele and Wiebe (2016) developed dynamic and equivalent static methods for capacity-design of CRSBF members. The dynamic approach combines frame member forces associated with rocking and higher mode responses. The former is obtained from a response spectrum analysis of the CRSBF using modified boundary conditions. The equivalent static procedure uses the second derivative of the closed form equations for the overturning moment to compute the distribution of inertial loads along the height of the structure. Second and third mode lateral forces are also considered. Both the dynamic and static procedures use a modified square-root-sum-of-squares approach to combine the modal forces.

2.2.2. Collapse assessment

Several studies evaluated the collapse performance of CRSBFs. Ma et al. (2011) demonstrated the adequacy of using a response modification factor of R = 8 by performing collapse analyses. Rahgozar et al. (2016) also conducted collapse assessments to evaluate the effectiveness of the response modification coefficient,. The results showed that using an R = 8 to design the frame the MCE level provided a large margin of safety against collapse. In fact, R values greater than 8 were proposed for taller buildings. The over-strength factor and period based ductility were also quantified using nonlinear static analyses.

Steel and Wiebe (2017) examined the effect of higher response modification factors (R > 8), the energy dissipation parameter, PT prestress ratio, PT location, and additional rocking joint on collapse risk of controlled rocking steel braced frames. The results showed that the probability of collapse increased with R factor for 3- and 6- story buildings by factors of 20 and 30, respectively but were still within an acceptable range. The study also showed that reducing the PT prestress ratio decreased the probability of collapse. Additionally, moving the PT stands to the center of the frame significantly reduced the probability of collapse in 6-story models and increasing the hysteretic ED ratio decreased probability of collapse.

2.2.3. Estimating seismic response

Christopoulos et al. (2002) investigated the seismic response of self-centering SDOF systems. A parametric study was conducted to investigate the effect of post yield stiffness and the energy dissipation parameter of the flag-shaped hysteretic behavior on displacement ductility. The response of the flag-shape SDOF systems was compared with responses of similar elasto-plastic hysteretic SDOFs representative of steel moment resisting frames (MRFs). The study showed that the flag-shaped hysteretic SDOF system resulted in lower

ductility demands and eliminated residual drifts. Christopoulos et al. (2003) extended the study of the sensitivity of the residual drift to the various assigned hysteretic rule to MDOF systems.

Seo and Sause (2005) also quantified the ductility demands in self-centering single-degree-of-freedom (SDOF) systems. The effect of the strength reduction factor, post yield stiffness, and energy dissipation capacity were examined. The ductility demands were shown to be sensitive to the post-yielding stiffness and hysteretic energy dissipation capacity of the self-centering systems, and decreased when the post-yielding stiffness and hysteretic energy dissipation capacity were increased.

Ma et al. (2011) developed a method to estimate peak drift demands in CRSBFs at MCE level shaking. After making an initial guess of the maximum drift, θ_e, a secant stiffness, K_s , for the equivalent SDOF is computed based on an analytical pushover curve for the controlled rocking steel braced frame system (Figure 2.11). An effective stiffness ratio, λ, that is taken to be greater than 1 is applied to the secant stiffness. This assumes that the effective stiffness, K_e, is larger, since the secant stiffness is associated with the peak response, and a larger stiffness is considered more representative over the duration of the earthquake. The equivalent period of the SDOF is computed based on this effective stiffness and a displacement response spectrum is used to update the estimate of the maximum drift demand. As with the approach proposed in the direct displacement-based design methodology (Priestley, 2000), the process is repeated until the drift values converge. The effective stiffness ratio used in this method is based on calibration to nonlinear dynamic analyses. An effective stiffness ratio of 1.8 was used by Ma et al. (2011) based on the results of NLRHA conducted on six building cases.
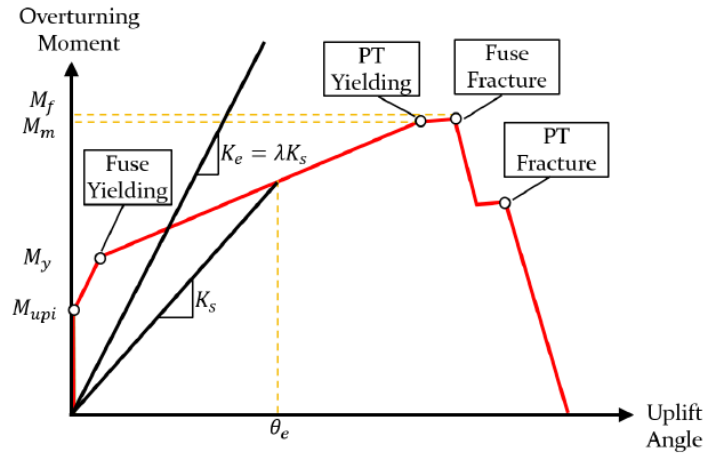
Figure 2.11. Effective stiffness used for drift prediction adopted from Ma et al. (2011)

Rahgozar et al. (2016) developed constant-strength (C_R) spectra for self-centering controlled rocking systems to estimate the ratio of the maximum inelastic to maximum elastic displacement. SDOF models with flag shaped behavior were analyzed under near-field pulse-like (NF-pulse) ground motions. Regression analyses were used to develop analytical equations for estimating the C_R spectra. Zhang et al. (2018) extended the previous SDOF studies for self-centering systems to consider the effect of higher response modification coefficients (larger than R = 10), negative secondary stiffness, and a tangent stiffness proportional damping model, on displacement demands. An equation was also proposed to estimate the displacement demands in the self-centering SDOF based on the hysteresis loop parameters, such as initial and secondary period (or initial and secondary stiffness), response modification parameter, R, Hysteretic energy dissipation ratio, β, and damping ratio, ξ.

Martin et al. (2018) used the same approach proposed by Ma et al. (2011), the only difference is to predict the maximum roof drift displacement instead of the maximum uplift of the CRSBFs.

The effect of design parameters such as the aspect ratio, response modification factor and initial post-tensioning force has also been examined using numerical simulations (Hall et al. 2010; Eatherton and Hajjar, 2011; Steele et al. 2017; Moradi and Burton, 2018).

16

CHAPTER 3: Design of Controlled Rocking Steel Braced Frame System

3.1. Design Procedure

Controlled rocking braced frames are constructed from post tensioning strands (PT), replaceable fuse, and braced frame members (i.e., beams, columns, and braces). Frame members are designed to remain essentially elastic during earthquake, the PT are also designed to remain elastic up to specific intensity level, and fuse yields to dissipate energy during earthquake shaking limits the forces transferred to the other components. The following sections summarizes the design procedure for CRSBFs based on Ma et al. (2011).

3.1.1. Design of post-tensioning strands and fuse

3.1.1.1. Post-tensioning and fuse required strength

Figure 3.1(a) shows the loads and resisting forces that are present in the CRSBF during earthquake including the dead load, the PT force, the fuse force, and lateral earthquake loads. Figure 3.1(b) and (c) show the idealized load-deformation of the PT and fuse respectively, and Figure 3.1(d) demonstrate the flag-shaped hysteretic behavior of the CRSBF based on the combined PT and fuse load-deformation. The PT force and dead load are downward and provide overturning resistance (i.e., restores the frame to its original position) (Figure 3.1(b)). The fuse force is downward during earthquake loading and also provides overturning resistance moment. However after yielding, the fuse force is in the upward direction (i.e. adds to the overturning demand) during unloading (Figure 3.1(c)). Point "a" allocated to the uplifting of the CRSBF that happens after columns decompression, where elastic deformation occurs in columns, PT , and fuse. Point "b" associated to the fuse yielding.
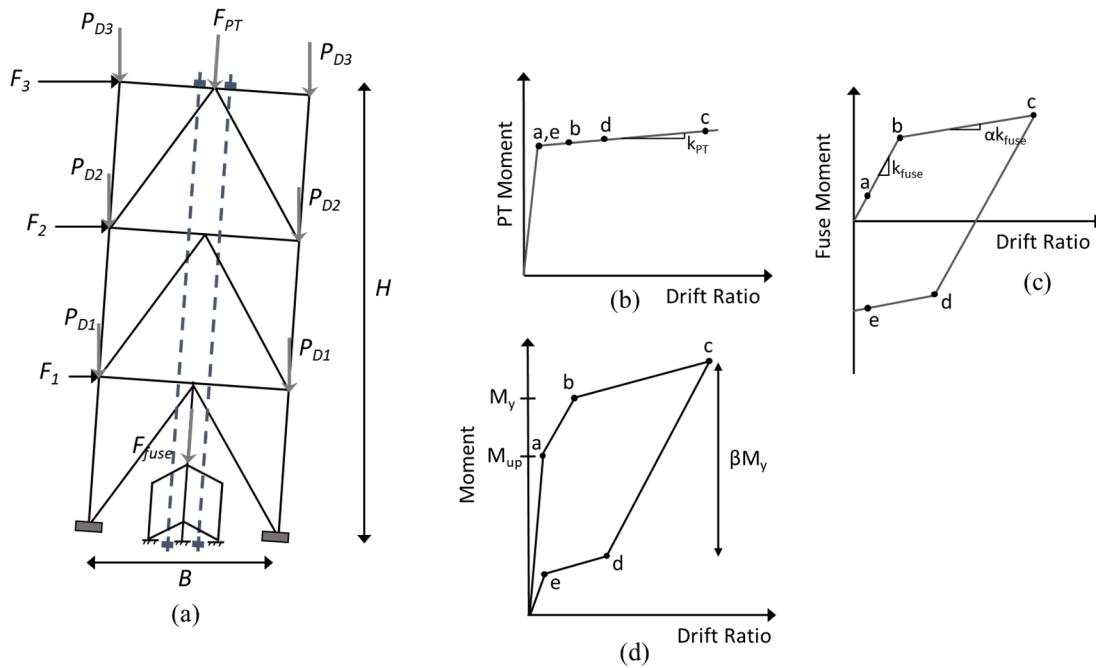
Figure 3.1. (a) Controlled rocking steel braced frame forces (b) force-deformation behavior of post-tensioning (c) force-deformation behavior of fuse (d) force-deformation behavior of combined system

The minimum required strength of the CRSBF is obtained from the equivalent lateral forces of ASCE 7-16 (ASCE 2016). Rigid body rotation dominates the rocking frame response of CRSBFs, especially for low and mid-rise buildings. As such, the lateral load distribution is based on a first mode deflection. The distributed inverse triangular lateral loads are computed based on the seismic weight and seismic response coefficients which obtained from the spectral parameters for the specific site (ASCE-Section 12.8.2.1). The distributed lateral forces are shown in Figure 3.1(a). The period of the structure is based on the equation specified in ASCE 7-16 for "other structures", which is amplified by 1.4 ($T = 1.4\,(0.02H)^{0.75}$). A response modification coefficient (R) of 8 is used. Note that there have been some studies that have concluded that an "R" factor equal to 8 or larger is sufficient enough for CRSBFs (e.g., Ma et al. 2011; Rahgozar et al. 2016; Steele & Wiebe 2016).

The overturning moment caused by the lateral forces is resisted by the restoring moments from the PT, fuse, and dead load. The minimum required overturning strength of the frame is based on the nominal overturning resisting moment times the resistance factor ($\varphi M_{ot,n}$). The nominal overturning resisting moment is based on fuse yielding. Although the overturning resistance is increases with the frame uplift, this effect is conservatively ignored.

$$M_{ot,n} = \frac{F_{PT}B}{2} + \frac{F_{yf}B}{2} + P_D B \tag{3.1}$$

where F_{PT} and F_{yf} are the initial PT force and fuse yield strength, P_D is the sum of the dead load attributed to one column of the rocking frame, and B is the rocking frame bay width. The required (demand) overturning moment ($M_{ot,u}$) is computed based on the story forces obtained from the equivalent lateral force (ELF) procedure. The nominal overturning resisting moment and the required overturning moment must satisfy the following inequality.

$$\varphi M_{ot,n} \geq M_{ot,u} \tag{3.2}$$

To define PT and fuse strength, the self-centering ratio, *SC* is considered. The *SC* ratio is an indicator of the capability of the rocking frame to be restored to its original position after overturning. It is the ratio of the overturning resistance provided by the PT and dead load and the overturning resistance provided by the fuse. As noted earlier, after fuse yielding, the unloading is directed upwards, therefore, to enhance the ability of the structure to return to the original position, the self-centering ratio should be greater than one.

$$SC = \frac{F_{PT} + 2P_D}{F_{yf}} \tag{3.3}$$

Substituting Equations 3.3 and 3.1 in Equation 3.2 with $\varphi = 0.9$, the minimum required PT and fuse strength is obtained from Equations 3.4 and 3.5, respectively.

$$F_{PT} = \frac{SC}{1 + SC} \frac{M_{ot,u}}{0.9B/2} - 2P_D \tag{3.4}$$

$$F_{yf} = \frac{1}{1+SC} \frac{M_{ot,u}}{0.9B/2} \tag{3.5}$$

To estimate the minimum required strength of the PT and fuse, first a value greater than one for the self-centering ratio is assumed. In addition, the energy dissipation ratio, β (shown in Figure 3.1(d)) is approximately related to the self-centering ratio (Eatherton et al. 2014) as follows.

$$\beta = \frac{1}{1+SC} \tag{3.6}$$

Eatherton et al. (2014) suggested using an energy dissipation ratio between 1 and 0.25 (i.e., $1 \leq SC \leq 3$).

3.1.1.2. Number of post-tensioning strands and fuse links

The number of PT strands is calculated based on its yield strength.

$$\frac{F_{PT}}{A_s} + E_{PT}\varepsilon_m \leq f_{PT,y} \tag{3.7}$$

Where ε_m is the strain of the PT strands at a target uplift ratio (θ_m) equal to $\frac{B\theta_m}{2H}$ based on the rigid body rotation behavior of the CRSBF, $f_{PT,y}$ is the yield stress of the PT strands (1.68 kN/mm^2), and E_{PT} is the modulus elasticity of PT (195.0 kN/mm^2). The minimum required PT strand area (A_s) is obtained using Equation 3.8 based on the target uplift ratio.

$$A_s = \frac{F_{PT}}{f_{PT,y} - E_{PT}\frac{B\theta_m}{2H}} \tag{3.8}$$

The number of PT strands is computed by dividing the area of a single strand (140.0 mm^2). Once the number (area) of PT strands is determined, the stiffness of the PT strands (unit of force/displacement) is calculated using Equation 3.9.

$$K_{PT} = \frac{A_s E_{PT}}{H} \tag{3.9}$$

The length of the fuse links are computed to limit its shear deformation to 20% at the peak uplift ratio (θ_m). The shear deformation of the fuse is computed using the rigid body rotation behavior, $L_{link} = \frac{\theta_m B}{2\,(0.2)}$.

Required number of butterfly fuses (n_L) is calculated based on the geometry of the links and the fuse strength using Equation 3.10.

$$n_L = \frac{9F_{yf}L_{link}}{4b^2 t_f \sigma_y} \tag{3.10}$$

Where b is the width of the butterfly fuse link at the end section; t_f is the link thickness; n_L is the number of the shear links; L_{link} is the link length; σ_y is yield stress. Ma et al (2011) determined that the optimal ratio of the width-to-thickness, $\frac{b}{t_f}$ is between 2 and 10, and $\frac{a}{b} = 1/3$, where a is the width of the butterfly fuse link at the middle section, to assure that buckling does not occur up to shear deformations of 30%.

The stiffness of the butterfly fuse (unit of force/displacement) is computed using the following equation based on the geometry of the fuse links.

$$K_{fuse} = \frac{1}{1 + \frac{2.8c}{L_{link}}} 0.47 n_L E t_f \left(\frac{b}{L_{link}}\right)^3 \tag{3.11}$$

Where E is Young's modulus and α is the strain hardening ratio, as shown in Figure 3.1(c).

Once the post-tensioning strands and fuse are designed, the next step is to check the self-centering ratio (SC^*) at unloading which accounts for PT loss due to yielding and strain hardening of the fuse (Eatherton et al. 2014). It should be noted that the PT peak strain ($\frac{B\theta_m}{2H}$) needs to be less than the strain corresponding to the limit state of interest.

$$SC^* = \frac{\left(f_{PT,y} - \frac{E_{PT}\theta_m B}{2H}\right)A_s + 2P_D}{F_{yf} + \left(\frac{\theta_m B}{2} - \frac{F_{yf}}{K_{fuse}}\right)\alpha K_{fuse}} \tag{3.12}$$

Once the PT and fuse are designed, the maximum story drift ratio needs to be estimated and checked against the code limit. Prior research has developed a methodology to predict maximum roof drift ratio based on SDOF equivalent properties. This is described in section 2.2.3 and the approach developed in the current study is presented in Chapter 5.

3.2. Prototype Buildings

This section describes the details of the protype buildings that will be used for this study in the next chapters.

3.2.1. Description of building cases

The buildings considered in this study range from 3 to 9 stories and have identical plan dimensions, story heights, gravity loads. The 3-, 6-, and 9-story are used for the primary design cases and the 4- and 8-story are used to evaluate the surrogate models. The typical plan dimension is shown in Figure 3.2 where all bays are 6.1m wide and the typical story height is 3.96 m. The rocking frames are all located on the perimeter of the building with two or four (depending on the building height) being used in each direction (see relevant chapter/study for details). The weight of a typical floor and the roof are 4251 kN and 4611 kN, respectively. The PT are located at the center of the bay and a single shear fuse located mid-bay at the base of the structure is used in each frame for all building cases. Two types of CRSBF brace frame layouts, chevron and X-brace configuration, are considered in this study (shown in Figure 3.3). Since the fuse force is applied to mid-span of the first-beam, compared to the X-brace, the chevron configuration results in higher shear and flexural demands in that beam.
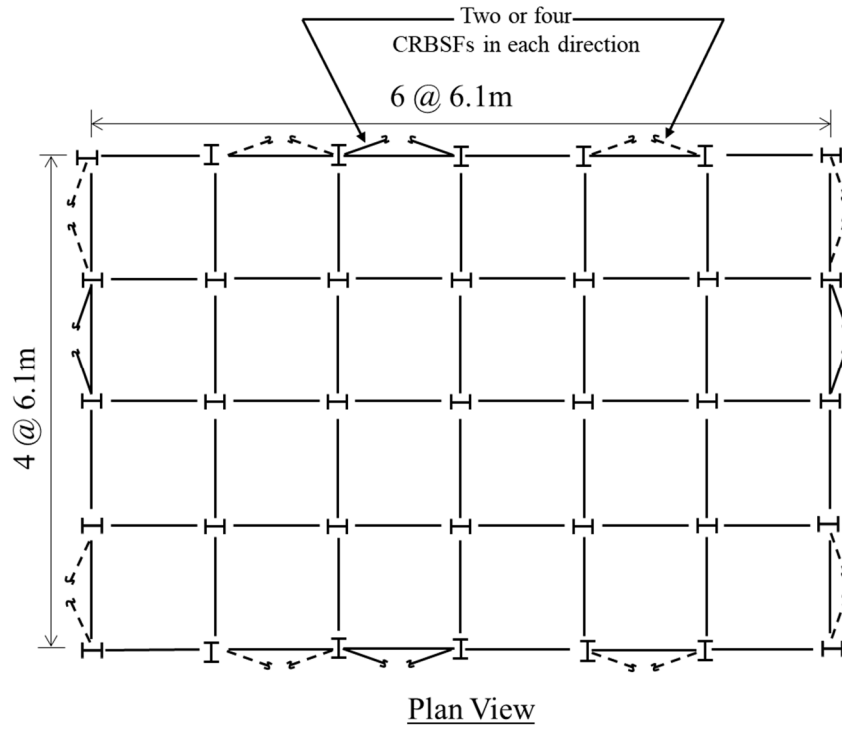
Figure 3.2. Typical floor plan for the considered building cases

(a)   (b)
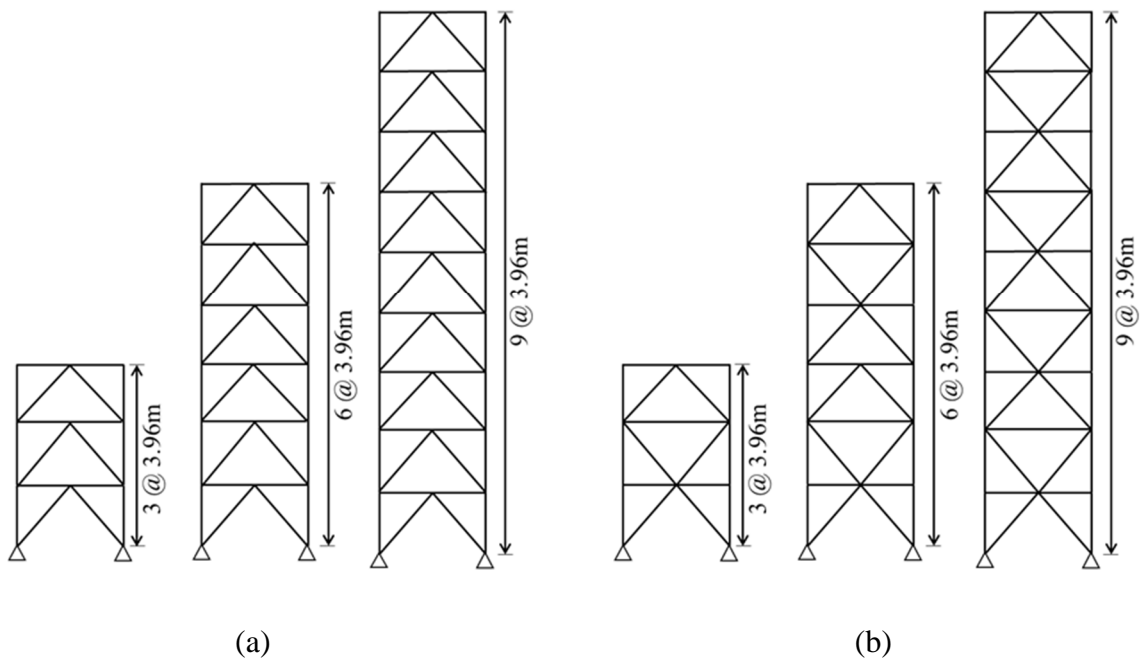
Figure 3.3. Braced frame configuration for 3-, 6- and 9-story CRSBFs: (a) chevron and (b) X-brace

3.2.2. Design of building cases

The design loads are based on the ASCE 7-16 (ASCE, 2016) standard and the seismicity parameters are taken as $S_S = 1.5$ and $S_1 = 0.6$ with Site Class D (stiff) soil. The designs are based on Risk Category II and Seismic Design Category D with a response modification factor $R = 8$, drift amplification factor $C_D = 5$, and importance factor, $I = 1.0$.

With the exception of the approach used to compute the forces in the beams, columns and braces of the rocking frame, the design procedure presented in Ma et al. (2011) is adopted, and is described in the last section. The required overturning strength is computed based on the story forces obtained from the equivalent lateral force (ELF) procedure. The dead load on the rocking frames (P_D) is primarily controlled by the framing plan configuration. The nominal strength of the fuse (F_{yf}) and the initial pretension force (F_{PT}) are allocated such that the minimum required overturning strength is achieved assuming a resistance factor of $\phi = 0.9$. The ratio of F_{PT} and dead load moments to F_{yf} moment is chosen such that the self-centering ratio of the CRSBF system is not less than 1.5 (Ma et al. 2011). The number and size of the PT strands are selected such that they will remain elastic for an uplift ratio corresponding to the drift limit at the maximum considered earthquake (MCE) hazard level, $\theta_{MCE} = 2.5\%$. The expected yield stress $(f_{PT,y})$, initial fracture stress $(f_{PT,u})$ and elastic modulus of the PT material (E_{PT}) are $1657.4\ N/mm^2$, $1861.6\ N/mm^2$ and $195\ KN/mm^2$, respectively. The effective width of the fuse is determined such that the shear deformation demand corresponding to θ_{MCE} does not exceed 20% (Ma et al. 2011). The design drifts are estimated using the iterative approach developed by Ma et al (2011). Table 3.1 listed the structural properties, PT, and fuse design for three baseline buildings.

Table 3.1. Summary of key design parameters for the 3-, 6- and 9-story building cases

Building ID	No. of Stories	T_a (s)	C_s	$M_{ot,u}$ (kN.m)	SC	P_D (kN)	F_{PT} (kN)	N_{PT}	F_{yf} (kN)	n_L
CRSBF-3S	3	0.44	0.13	7665	1.5	273	952	18	1168	38
CRSBF-6S	6	0.73	0.13	14244	1.5	539	2037	14	2091	68
CRSBF-9S	9	1.00	0.08	19042	1.5	805	2556	23	2829	92

T_a: Approximate period (ASCE 7-16 Equation 12.8-7)

The equivalent static procedure developed by Steele and Wiebe (2016) is used to compute the design forces for the beams, columns and braces of the rocking frame. For each rocking frame (one for each building), a linear elastic model is developed in MASTAN2 (Ziemian and McGuire, 2007) with a pinned support at the pivot-point and vertical springs at the PT anchor-point. The elastic axial stiffness of the PT is applied to the vertical spring. Square-root-sum-of-squares-combined story forces corresponding to the first three modes are applied to the structure. The first modal periods is listed in Table 3.2 for three building cases along with the Sa_{T1} corresponding to the MCE hazard level (S_{MT}). The first-mode forces, which are based on the ELF procedure, are amplified by the ratio (Ω) of the maximum expected (M_{max}) to the minimum required (M_{min}) overturning moment at the base. M_{min} is the overturning moment computed from the ELF story forces and M_{max} corresponds to the fuse and PT at ultimate strength. The second- and third-mode story force profile are computed using Eqs. 13 and 14 from Steele and Wiebe (2016). The ultimate post-tensioning force, $F_{PT,u}$, and the maximum expected fuse force, $F_{f,u}$, are also applied to the structure. Table 3.2 listed a summary of the ultimate forces and moments for capacity design of frame members.

Table 3.2. Base rocking joint parameters for the 3-, 6- and 9-story building cases

Building ID	Model Periods, T_i (s)			S_{MT}	$F_{PT,u}$ (kN)	$F_{f,u}$ (kN)	M_{min} (kN.m)	M_{max} (kN.m)	Ω
	Mode 1	Mode 2	Mode 3						
CRSBF-3S	0.44	0.15	0.09	1.50	4691	2267	7665	22874	2.98
CRSBF-6S	0.73	0.24	0.15	1.23	3649	4057	14244	26771	1.88
CRSBF-9S	1.00	0.33	0.20	0.90	5994	5489	19042	39904	2.10

S_{MT}: Maximum considered earthquake spectral acceleration at mode1 period

Once the combined forces for each members are obtained, member sizes can be obtained based on the steel compression components, which is specified in Chapter E of AISC-341 (AISC 2016).

CHAPTER 4:   Structural Modeling

4.1.   Numerical Modeling

Two-dimensional nonlinear structural models are developed in OpenSees (McKenna, 1999). Figure 4.1 shows a schematic representation of the numerical model for the 3-story building case with chevron braces.

The beams, columns and braces are modeled using fiber elements with the Giufrré–Menegotto–Pinto material with 0.3% strain hardening. Corotational transformation and initial imperfections are used in the braces to capture inelastic buckling. The recommendations by Uriz et al. (2008) are used as the basis for specifying the initial out-of-plane imperfection, the discretization and number of integration points along the brace length and the number of fibers over the cross section. More specifically, an initial imperfection of 0.1% of the brace length is used and as shown in Figure 4.1, the brace is discretized into twelve elements along its length. Five integration points are used along the brace length and sixteen by four fibers are used along the length and thickness of the web and flange cross sections, respectively. The same number of integration points and fibers are used in the beams and columns. Rigid elements are placed at the ends of the braces, beams and columns to reflect the presence of the panel zones and gusset plates. Pinned connections are used at the end of the braces and beam-column connections.

Rocking behavior is simulated using compression-only gap elements placed at the base of each column. These gap elements have zero tensile stiffness and are near-rigid in compression. Rayleigh damping is used with 2% of critical damping applied to the first and third modes. A leaning column is placed on each side of the rocking frame to capture the destabilizing effect

of gravity loads on frames not included in the structural model. Pin-ended strut elements are used to connect the rocking frame to the leaning columns.

The PT strands are modeled using corotational trusses with hook elements (tension only) and a multilinear material to capture initial and complete fracture (Ma et al. 2011). Figure 4.2(a) shows the PT model in OpenSees and Figure 4.2(b) shows the material used for the PT. Two material models (Material A and Material B) combined in series were used to model the PT (Ma et al. 2011). Material A is elastic perfectly plastic with initial strain equal to the PT initial strain. A large yield strain is defined to keep the material behavior elastically. Material B is a Hysteretic material with ε_1 and ε_2 corresponding to the PT yield and ultimate stresses, respectively. The properties of the materials are listed in Table 4.1. The associated parameters include the elastic modulus ($E_{PT} = 195 kN/mm^2$), the expected yield $\left(f_{PT,y} = 1.7 kN/mm^2\right)$ and fracture stress $\left(f_{PT,u} = 1.9 kN/mm^2\right)$ and the corresponding strain values, which are $\varepsilon_{yPT} = 0.87\%$ and $\varepsilon_{uPT} = 1\%$, receptively. When fracture occurs, the PT stress degrades to zero at 5% strain.
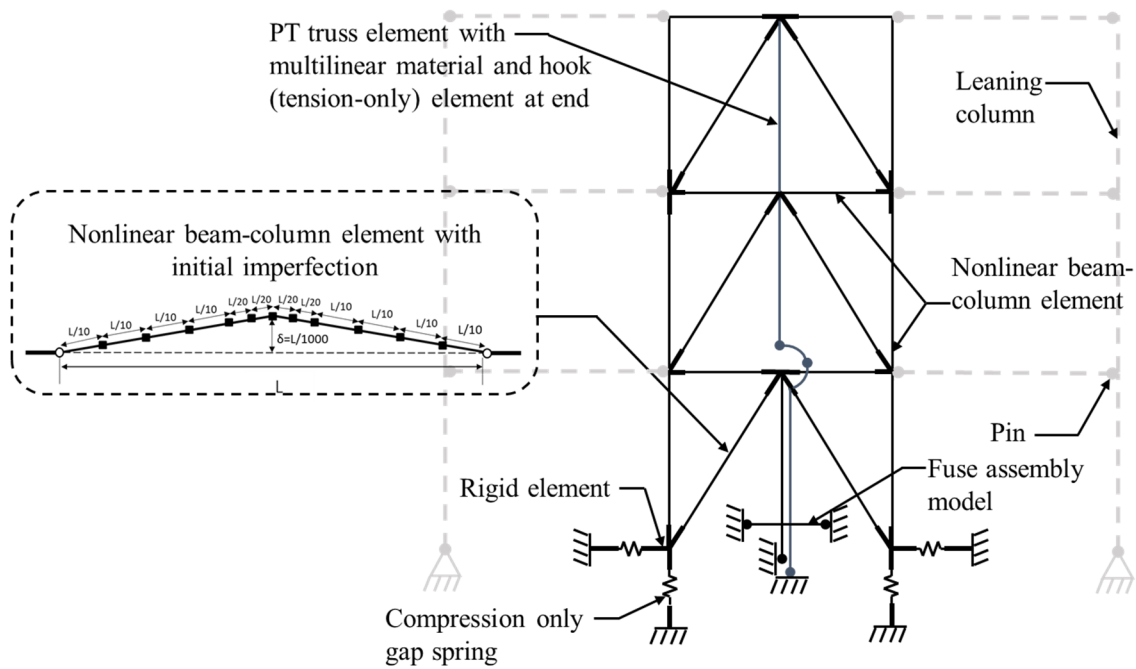
Figure 4.1. Schematic representation of the numerical model for the 3-story CRSBF
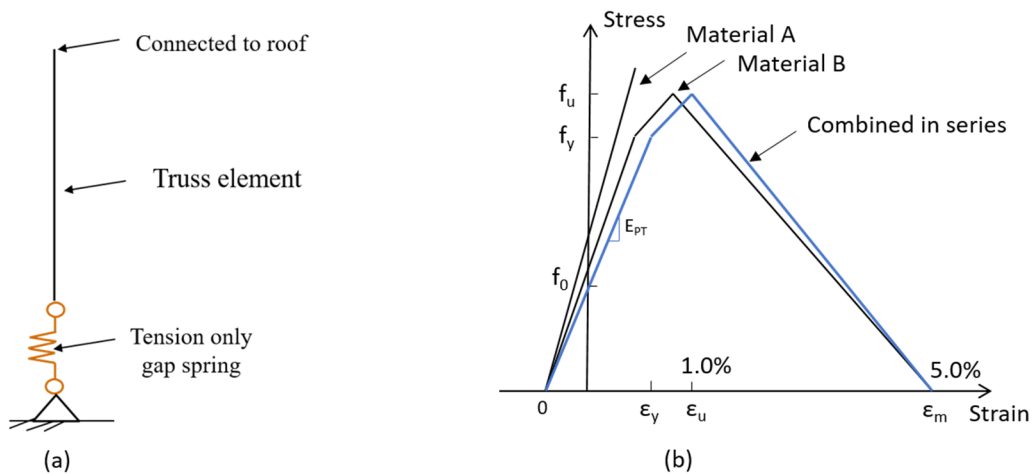
Figure 4.2. (a) PT model in OpenSees (b) PT material model in OpenSees (Ma et al. 2011)

Table 4.1. Material properties in OpenSees model (Ma et al. 2011)

Material A (EPP)	Material B (Hysteretic Material)
$E_A = 2E_{PT}$	$\varepsilon_1 = f_y/2E_{PT}$
$\varepsilon_{y,A} = 1.0$	$\varepsilon_2 = \varepsilon_u - f_u/2E_{PT}$

The behavior of the energy-dissipating fuses is represented using the assembly model proposed by Ma et al. (2011) (Figure 4.3(a)). Instead of modeling all the links, one link on each side is modeled. These fuse link models are represented by two elements. One captures the axial behavior and the second element is used to model the flexural behavior of the fuse. The axial element is implemented as the "dispBeamColumn" with "Steel02" material in OpenSees (Figure 4.3(c)). The flexural element is modeled with a beam-column element with large flexural stiffness and rotational springs on both ends. The rotational springs, which are constrained to axial elements, are modeled using "zero Length" springs with the moment-rotation relationship shown in Figure 4.3(d).
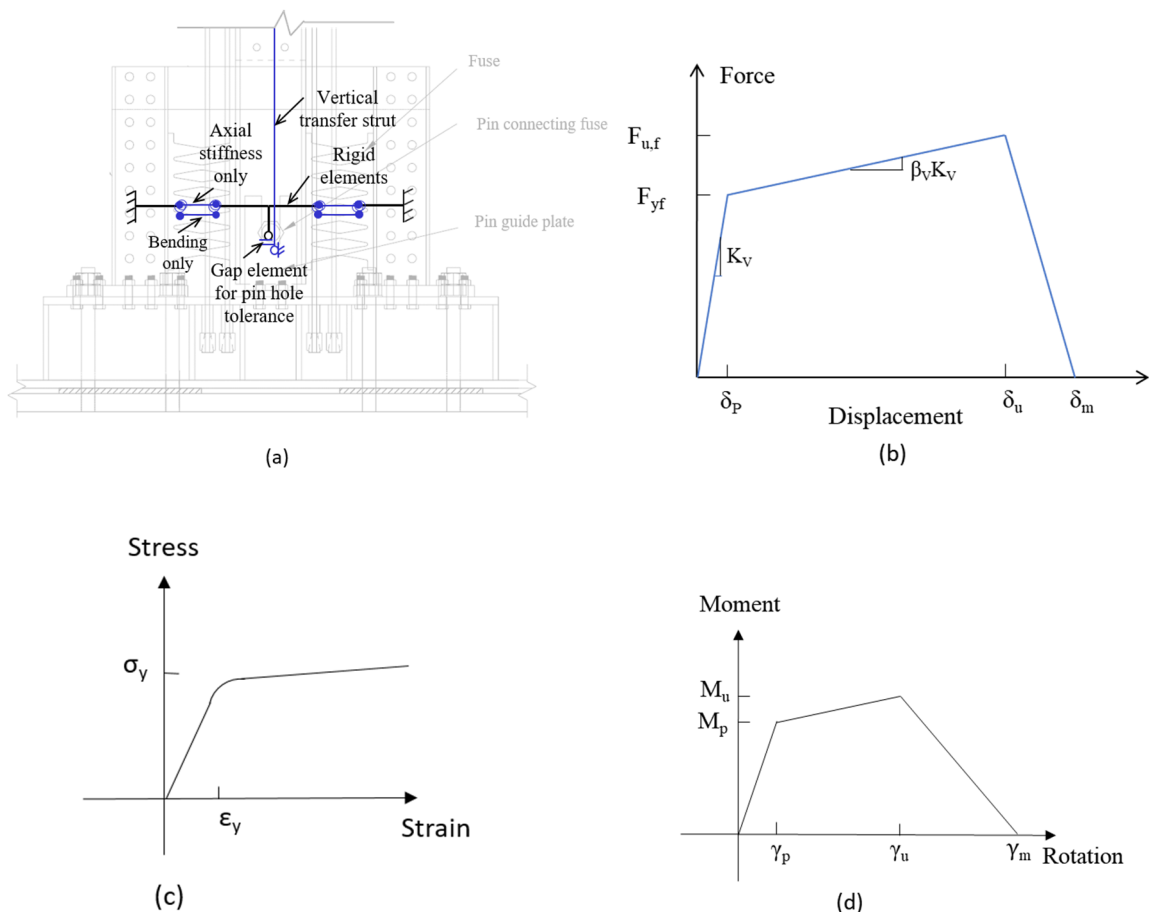
Figure 4.3. (a) Fuse assembly in OpenSees model (Ma et al. 2011) (b) Fuse material model (c) fuse axial only material in OpenSees (d) Bending model in OpenSees

Table 4.2. Fuse bending model properties

M_p	γ_p	M_u	γ_u	γ_m
$F_{yf}L_e/4$	F_{yf}/K_vL_e	$F_{f,u}L_e/4$	0.35	0.5

Table 4.2 shows the values of the moment-rotation relationship for degrading fuse. Yield and ultimate moments (M_p and M_u) are based on the nominal and ultimate fuse strength (F_{yf} and $F_{f,u}$) and the yield rotation corresponds to a shear displacement (δ_p) equal to F_{yf}/K_v. The shear deformation at initial and ultimate fuse fracture (zero stress) are $\gamma_u = 0.35$ and $\gamma_m = 0.5$, respectively (Ma et al. 2011). The "Hysteretic" material in OpenSees is used to model rotational spring material.

4.2. Verifying Structural Modeling in OpenSees

To verify the modeling approach adopted for the CRSBF, the nonlinear response history from the two shake-table from Ma et al. (2011) are compared to the responses from a numerical analysis. Figure 4.4(a) and (b) show the responses from the experiment and numerical models. The overturning moment hysteresis comparison for test BJ6 and BJ3 of specimens B subjected to 60% and 30% Kobe ground motion are shown in Figure 4.5. Both show a reasonable match between the experimental and numerical responses. The hysteresis represents the moment ratio versus the uplift ratio, where the former is the ratio of the overturning moment based on the PT and fuse forces (M_{RS}) to the yield overturning moment (M_{OTY}). In order to compare the numerical and experimental responses quantitively, the energy dissipation of two models are shown in Figure 4.6, which is the area of the hysteresis responses of Figure 4.5(b) for both models.
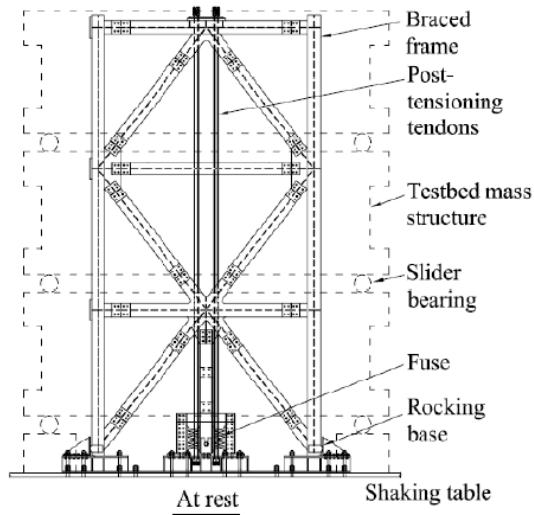
Figure 4.4. Elevation view of shake-table test specimen (Ma et al. 2011)

(a)

(b)
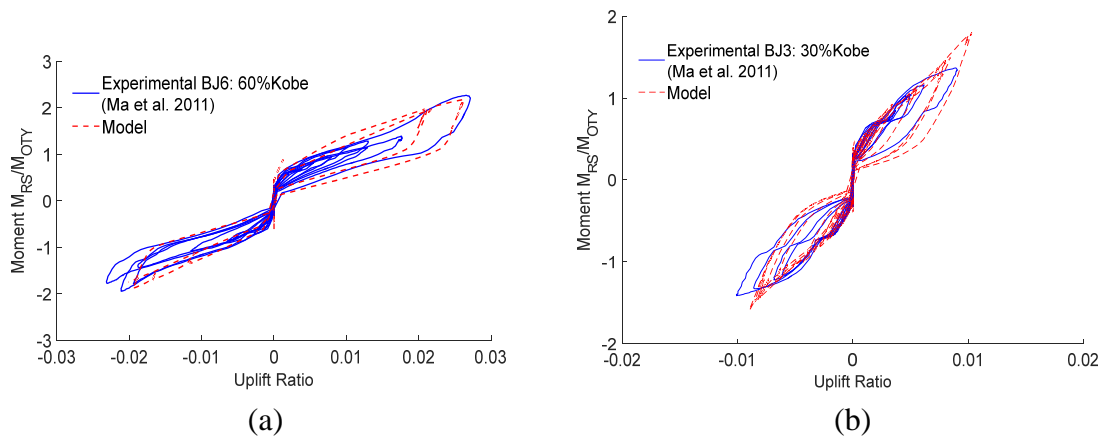
Figure 4.5. Comparison of experimental response with numerical modeling response
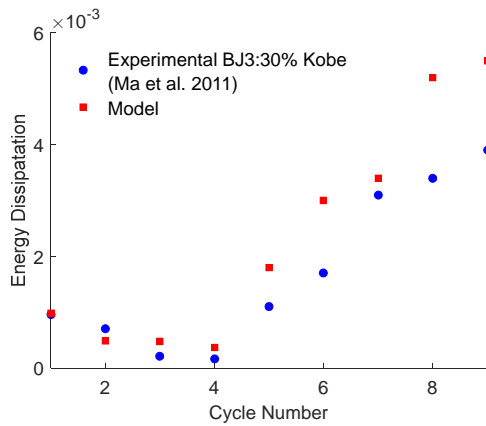
Figure 4.6. Comparison of experimental and numerical energy dissipation

32

CHAPTER 5:   Estimating Maximum Engineering Demand Parameters (EDPs)

5.1.   Overview of Approach used to Estimate CRSBF Peak Response

Figure 5.1 shows an overview of the methodology used to predict the engineering demand parameters (EDPs) in the CRSBF. The first step is to identify the effective design variables to be used as input parameters. The key design variables that are considered in this study are the dead load on the rocking frame (P_D), the initial PT force (F_{PT}), the fuse yield strength (F_{yf}), the fuse strain hardening ratio (α), and the frame aspect ratio (i.e., the bay width-t-height ratio) (*B/H*). Once the primary design variables have established, a sampling plan needs to be developed to provide a combination of key design variables(details discussed in section 5.3.1). A set of CRSBF buildings are designed based on the parameter combinations identified in the sampling plan and the nonlinear response history analyses of the associated structural models are performed to obtain the peak response demands (i.e., maximum story drift ratio, peak floor acceleration, and maximum residual drift). The spectral acceleration at the effective period, which is one of the input variables used to estimate the response demands, is obtained from each considered ground motion and an equivalent single degree of freedom (SDOF) of the CRSBF (the sub steps is explained in section 5.4). The selection, training, and validation of the surrogate models are the next steps in the process which are explained in section 5.5.
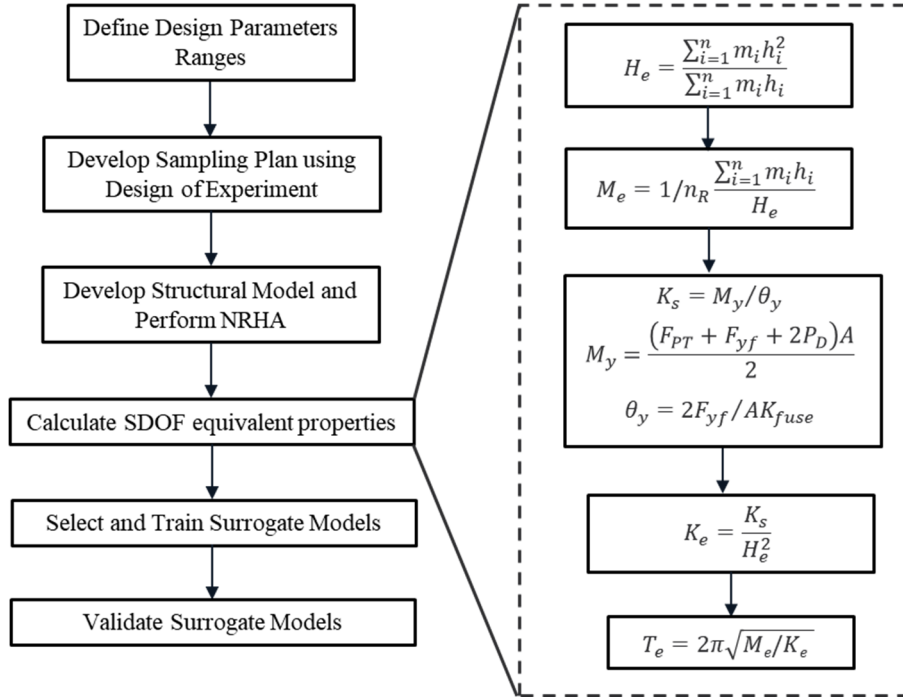
Figure 5.1. Overview methodology to predict the peak structural responses in the CRSBF

The plan configuration shown in Figure 3.2 is used and the surrogate models are trained using data from 3-, 6- and 9-story buildings and tested on data generated from 4- and 8-story buildings. The chevron brace configuration shown in Figure 3.3(a) is considered.

5.2. Statistical Surrogate Models

The seismic response of 3-, 6-, and 9- story CRBFs buildings with combinations of various design factors are considered to predict the maximum interstory drift ratio, peak floor acceleration, and residual story drift ratio. Nonlinear response history analyses are performed on 129 CRBFs, which includes 43 models for each of 3-, 6-, and 9- story cases.

5.2.1. Key design parameters

There are several design parameters that effect seismic response of CRSBFs. The initial post-tensioning (PT) force (F_{PT}), fuse yielding strength (F_{yf}), frame aspect ratio (i.e., the bay width to the height ratio (B/H)), fuse strain hardening ratio (α), and dead load applied on each

34

column of CRSBF (P_D) are the five parameters that are considered in each 3-, 6-, and 9-story buildings. The tributary seismic weight of the floor and the height story of the cases remains the same for all the cases. The PT force, fuse yield strength and rocking frame dead load are are normalized to the seismic weight of the building (W_s). The considered parameter ranges are defined by the upper and lower limit listed in Table 5.1. The upper and lower levels are based on reasonable hysteretic energy dissipation ratios ($0.25 \leq \beta \leq 0.5$) or having the self-centering ratio greater than 1.0. The center levels are the average of the upper and lower levels.

Table 5.1. Ranges of normalized design key factors

Factor	Symbol	Lower level	Central level	Higher level
Normalized initial PT force	F_{PT}/W_s	0.15	0.225	0.3
Normalized Fuse yield stress	Fyf/W_s	0.3	0.4	0.5
Normalized gravity load on a rocking column	P_D/W_s	0.15	0.225	0.3
Fuse strain hardening ratio	α	0.02	0.04	0.06
Frame aspect ratio	B/H	0.2	0.35	0.5

The factor combinations are defined using Design of Experiment (DOE) method (Moradi et al. 2018). For k factors, a CCD consists of a two-level factorial design (2k factorial runs), 2k axial or star runs, and one or more center run(s). For five factor (k=5), 25 axial runs, 2×5 axial runs, and one center point is resulted to 43 models for each 3, 6, and 9 story CRSBFs. Table 5.2 shows the factor combinations generated using the Design-Expert software where the values −1, 0, and +1 denote the lower, central, and higher levels of the input parameters, respectively (Moradi et al. 2018).

Table 5.2. Factor combination in coded units

Combination no.	Design key parameter				
	F_{PT}/ W_s	F_{yf}/ W_s	P_D/ W_s	α	B/H
1	-1	-1	-1	-1	-1
2	-1	-1	1	-1	-1
3	1	-1	-1	-1	-1
4	1	-1	1	-1	-1
5	-1	1	-1	-1	-1
6	-1	1	1	-1	-1
7	1	1	-1	-1	-1
8	1	1	1	-1	-1
9	-1	-1	-1	-1	1
10	-1	-1	1	-1	1
11	1	-1	-1	-1	1
12	1	-1	1	-1	1
13	-1	1	-1	-1	1
14	-1	1	1	-1	1
15	1	1	-1	-1	1
16	1	1	1	-1	1
17	-1	-1	-1	1	-1
18	-1	-1	1	1	-1
19	1	-1	-1	1	-1
20	1	-1	1	1	-1
21	-1	1	-1	1	-1

22	-1	1	1	1	-1
23	1	1	-1	1	-1
24	1	1	1	1	-1
25	-1	-1	-1	1	1
26	-1	-1	1	1	1
27	1	-1	-1	1	1
28	1	-1	1	1	1
29	-1	1	-1	1	1
30	-1	1	1	1	1
31	1	1	-1	1	1
32	1	1	1	1	1
33	0	0	-1	0	0
34	0	0	1	0	0
35	-1	0	0	0	0
36	1	0	0	0	0
37	0	-1	0	0	0
38	0	1	0	0	0
39	0	0	0	0	-1
40	0	0	0	0	1
41	0	0	0	-1	0
42	0	0	0	1	0
43	0	0	0	0	0

5.2.2. Ground motions

80 unscaled ground motion records are used for the analyses of each model of sampling point. These ground motions are selected for stiff soil conditions (i.e. ASCE 7 site class D) from set #1A of the PEER transportation systems research program (Jack Baker et al. 2011). These ground motions selected such that their response spectra match the median and log standard deviations predicted for a magnitude 7 strike slip earthquake at a distance of 10 km. The elastic acceleration response spectra for the individual motions along with the median spectra are shown in Figure 5.2. A total of 10,320 nonlinear response history analyses (129 combinations of input parameters subject to 80 ground motions) are performed to obtain the statistical data used for the regression procedure.
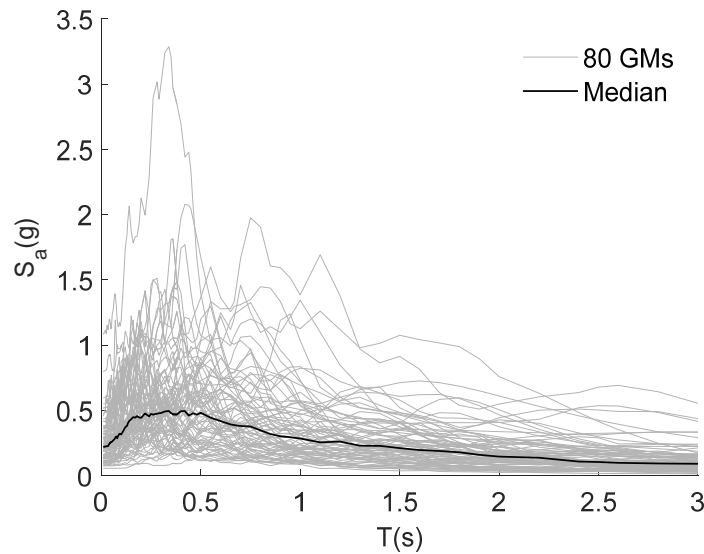
Figure 5.2. 5% damped elastic spectral acceleration of the ground motions used to develop the surrogate model

5.3.   Estimating Effective Period

As it was mentioned earlier, the goal of this chapter is to propose surrogate models to predict the peak response demands in the CRSBF, including the maximum interstory drift ratio (SDR_{max}), the residual story drift ratio (RDR_{max}), and the peak floor acceleration(PFA)).

Therefore, the responses are outputs and there are five key design parameters (P_D/W, F_{pt}/W, F_{yf}/W, B/H, and α) described earlier, are inputs. The number of the stories and spectral acceleration (S_a) are also considered as input parameters. Due to rigid body rotation characteristics of the CRSBF, an equivalent SDOF procedure is used to estimate the period of the CRSBF and eventually the spectral acceleration of each ground motion associated with the equivalent SDOF period. The procedure of estimating the equivalent SDOF period is shown in the following steps:

1) Compute the equivalent SDOF height from building properties (Priestley et al. 2007):

$$H_e = \frac{\sum_{i=1}^{n} m_i h_i^2}{\sum_{i=1}^{n} m_i h_i} \quad (5.1)$$

where, i is the floor number, m_i and h_i are the floor mass and height, and n is the number of the stories.

2) Compute the equivalent SDOF mass:

$$M_e = \frac{1}{n_R} \frac{\sum_{i=1}^{n} m_i h_i}{H_e} \quad (5.2)$$

where n_R is the number of the controlled rocking frame in each direction.

3) Compute equivalent SDOF stiffness:

Figure 5.3 shows the backbone curve of a CRBF which includes initial uplift (M_{up}, θ_{up}), resisted by the initial post tensioning force and dead load, yielding of the fuse element (M_y, θ_y), and the maximum drift, which is considered as the MCE deformation (M_{MCE}, θ_{MCE}). The secant stiffness is obtained as the ratio of the overturning moment to the uplift ratio at the yield point,

$K_s = \dfrac{M_y}{q_y}$. The equivalent SDOF stiffness, K_e, can be obtained based on the equality between

the overturning moment in the MDOF system and the SDOF model (Ma et al. 2011),

$K_e q = K_s (H_e q) H_e$. The equivalent SDOF stiffness is then computed as

$$K_e = \frac{K_s}{H_e^2} \tag{5.3}$$

    4) Compute the equivalent SDOF period:

$$T_e = 2p \sqrt{\frac{M_e}{K_e}} \tag{5.4}$$
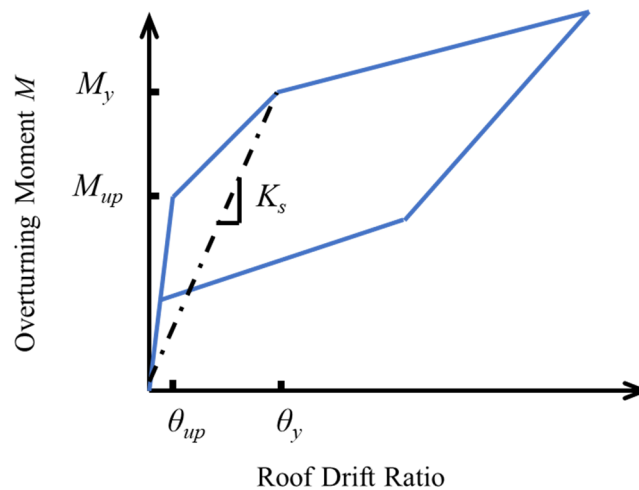
Figure 5.3. Rocking brace frame moment-rotation behavior and initial stiffness

5.4.   **Surrogate Models Development**

A total of 129 CRSBFs are designed based on the 43 sampling point (Table 5.2) for each

of the 3-story, 6-story, and 9-story buildings, and nonlinear response history analysis is

performed for the unscaled 80 ground motions to obtain the maximum story drift ratio, residual

story drift ratio, and peak floor acceleration (EDPs). The surrogate models are developed to

represent the relationship between the input parameters (P_D/W, F_{pt}/W, F_{yf}/W, B/H, α, N, and S_a) and the response variables (peak structural demands).

The 80 unscaled ground motions (Figure 5.2) used in the analysis is divided into bins of different sizes (2, 4, 6, 8, and 10 partitions) based on the sorted S_a at T_e . The median S_a of each bin is used to develop the surrogate models i.e. one model per bin size. The goal here is to evaluate the effect of bin size on the efficacy of the predictive model.

To investigate the accuracy of the surrogate models, the same set of ground motions are scaled to four hazard levels including the service level earthquake (SLE), design based earthquake (DBE), maximum considered earthquake (MCE), and (OVE). The return period of SLE, DBE, MCE, and OVE is 43, 475, 2475, 4975 and respectively. Figure 5.4 shows the spectral acceleration for the four selected hazard levels.
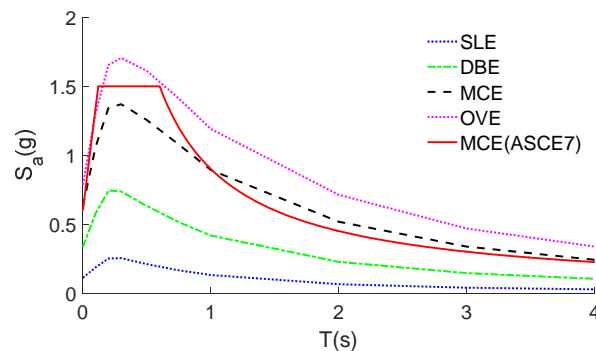
Figure 5.4. Acceleration spectra for DBE, MCE, OVE, and MCE (ASCE7)

The effective period of each sampling point (CRSBF) is used to obtain the spectral acceleration for each hazard level (Figure 5.4) and the ratio between the each hazard level and MCE (ASCE7) obtained for each sampling point.. Table 5.3 shows the mean and standard deviation of the ratios between each hazard level and the MCE level. The mean ratios are used as scale factors relative to the MCE level for all the sampling points

41

Table 5.3. Ratio of four hazard levels to MCE hazard level

	SLE/MCE	DBE/MCE	OVE/MCE	MCE(ASCE)/MCE	DBE(ASCE)/DBE
Mean	0.18	0.52	1.26	1.14	1.47
STD	0.01	0.022	0.023	0.056	0.12

The nonlinear model for each surrogate model is in form of Equation 5.5:

$$y = b_0 \prod_{i=1}^{k} x_i^{b_i} \tag{5.5}$$

where β's are the unknown regression coefficients and the x_i's are the seven input parameters (i.e. P_D/W, F_{PT}/W, F_{yf}/W, B/H, α, N, and S_a). The unknown coefficients are obtained using "fitlm" function in MATLAB.

5.4.1. Maximum story drift ratio (SDR_{max})

Nonlinear response history analyses of the 129 CRBFs subjected to 80 unscaled ground motions are performed and the maximum story drift ratios are recorded. The spectral acceleration of 80 ground motions are sorted, and divided to bins based on 2, 4, 6, 8, and 10 partitions. The median maximum story drift ratio for each partition is used as output parameter (y) of the Equation 5.5. Table 5.4 shows the regression coefficient (β_i) of each input parameter for different numbers of partitions.

Table 5.4. Regression coefficients for maximum story drif ratio (SDR_{max})

i	Input parameter, x_i	2Bins	4Bins	6Bins	8Bins	10Bins
0	β_0	0.0054	0.0058	0.0058	0.0057	0.0057
1	S_a	0.937	0.886	0.873	0.842	0.843
2	P_D/W	-0.110	-0.119	-0.132	-0.102	-0.116
3	F_{PT}/W	-0.050	-0.049	-0.046	-0.041	-0.039
4	F_{yf}/W	-0.414	-0.415	-0.390	-0.405	-0.406
5	B/H	-0.732	-0.796	-0.808	-0.796	-0.798
6	α	-0.076	-0.080	-0.083	-0.080	-0.083
7	N	-0.358	-0.439	-0.447	-0.422	-0.433

All the 129 models are analyzed using the same ground motion set, which are scaled to the four different hazard levels (SLE, DBE, MCE, and OVE), and the median maximum story drift

ratio for non-collapsed ground motions are used to assess the accuracy of the proposed prediction equation for five different bins equations. The coefficient of determination (R^2) and median absolute relative deviation (*MARD*) are used as the metrics of the model performance. The latter is computed as the median of the absolute difference between the predicted and actual response variables normalized by the actual values (Sun et al. 2017). The results for both metrics are shown in Table 5.5. The training (unscaled ground motions) and testing models (scaled ground motions) have acceptable accuracy with MARD values of approximately 20% or less. A slight decrease in accuracy is obtained when the number of the bins is reduced.

Table 5.5. Surrogate model verification for SDR_{max}

Number of Bins	Training		Testing	
	R^2	MARD	R^2	MARD
2	0.9	0.10	0.60	0.17
4	0.85	0.09	0.63	0.19
6	0.83	0.11	0.62	0.19
8	0.83	0.12	0.58	0.21
10	0.81	0.14	0.59	0.21

Figure 5.5 shows the SDR_{max} MARD as a function of the hazard level for each bin size. It shows that the predictive accuracy is reasonable for almost the bin sizes. The most accurate SDR_{max} prediction is at the DBE hazard level with a MARD of approximately 0.1. Also, the MARD values increase with the hazard level. This is not surprising as the responses used for training are based on unscaled ground motions.
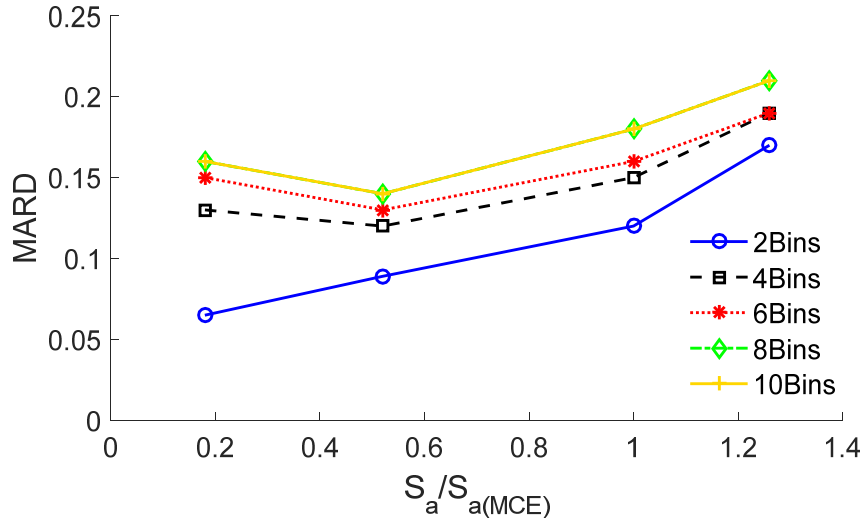
Figure 5.5. *SDRmax* MARD as a function of the hazard level and bin size

5.4.2. Peak floor acceleration (*PFA*)

The same procedure is used for the peak floor acceleration surrogate model. Table 5.6 shows the regression coefficients for each input parameter and bin size. Table 5.7 shows the accuracy of the training and testing models, which is less than maximum story drift ratio prediction, but still reasonable. Figure 5.6 shows the *PFA* MARD as a function of the hazard level for each bin size. It is observed that the number of the bins does not have a significant effect on the accuracy of the peak floor acceleration, and the maximum MARD is approximately 0.2.

Table 5.6. Regression coefficients for peak floor acceleration (*PFA*)

i	Input parameter, x_i	2Bins	4Bins	6Bins	8Bins	10Bins
0	β_0	2.170	2.114	2.177	2.090	2.187
1	S_a	0.834	0.818	0.817	0.801	0.806
2	P_D/W	-0.137	-0.152	-0.193	-0.174	-0.177
3	F_{PT}/W	-0.001	-0.003	-0.005	0.002	0.002
4	F_{yf}/W	0.278	0.250	0.297	0.275	0.283
5	B/H	0.113	0.132	0.104	0.106	0.111
6	α	0.125	0.115	0.116	0.113	0.114
7	N	0.213	0.196	0.158	0.174	0.164

Table 5.7. Surrogate model verification for *PFA*

Number of Bins	Training		Testing	
	R^2	MARD	R^2	MARD
2	0.73	0.15	0.76	0.17
4	0.71	0.14	0.76	0.19
6	0.69	0.14	0.74	0.19
8	0.72	0.16	0.74	0.19
10	0.68	0.16	0.74	0.19
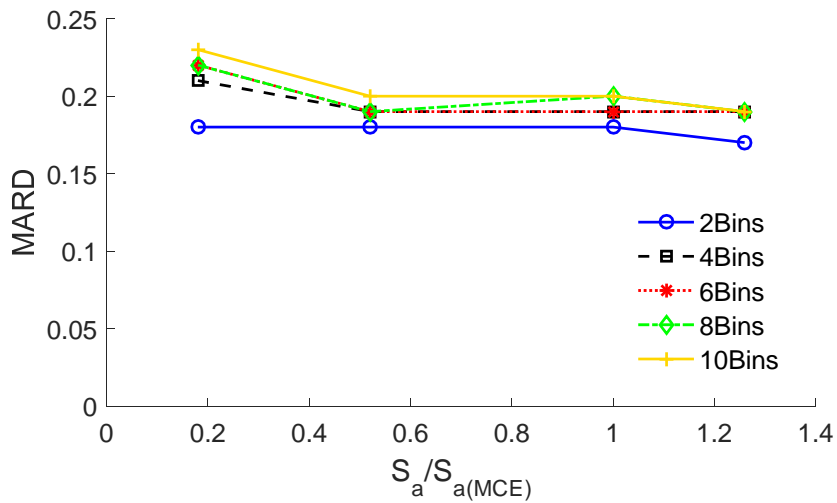
Figure 5.6. *PFA* MARD as a function of the hazard level and bin size

5.4.3. Maximum residual story drift ratio (*RDR_{max}*)

The surrogate model coefficients for the maximum residual drift is shown in Table 5.8 for the different bin sizes. Table 5.9 shows the R^2 and *MARD* values for the different bin sizes and Figure 5.7 shows the MARD as a function of the hazard level and bin size. The results show that the *RDR_{max}* surrogate model does not perform well in terms of predictive performance. This is not surprising since the residual demands are small which makes it difficult to develop a strong predictive model (Table 5.9).

Table 5.8. Regression powers for maximum residual story drift ratio *(RDR_max)*

i	Input parameter, x_i	2Bins	4Bins	6Bins	8Bins	10Bins
0	β_0	0.001	0.001	0.001	0.001	0.001
1	S_a	1.261	1.179	1.156	1.083	1.075
2	P_D/W	0.025	0.039	0.029	0.082	0.068
3	F_{PT}/W	-0.137	-0.135	-0.128	-0.099	-0.094
4	F_{yf}/W	-1.236	-1.268	-1.187	-1.156	-1.180
5	B/H	-1.035	-1.082	-1.089	-1.015	-1.047
6	α	-0.347	-0.324	-0.338	-0.338	-0.352
7	N	-0.929	-0.920	-0.926	-0.805	-0.885

Table 5.9. Surrogate model verification for *RDR_max*

Number of Bins	Training		Testing	
	R^2	MARD	R^2	MARD
2	0.71	0.32	0.25	0.37
4	0.63	0.35	0.27	0.44
6	0.60	0.35	0.25	0.45
8	0.56	0.37	0.17	0.46
10	0.56	0.37	0.18	0.46
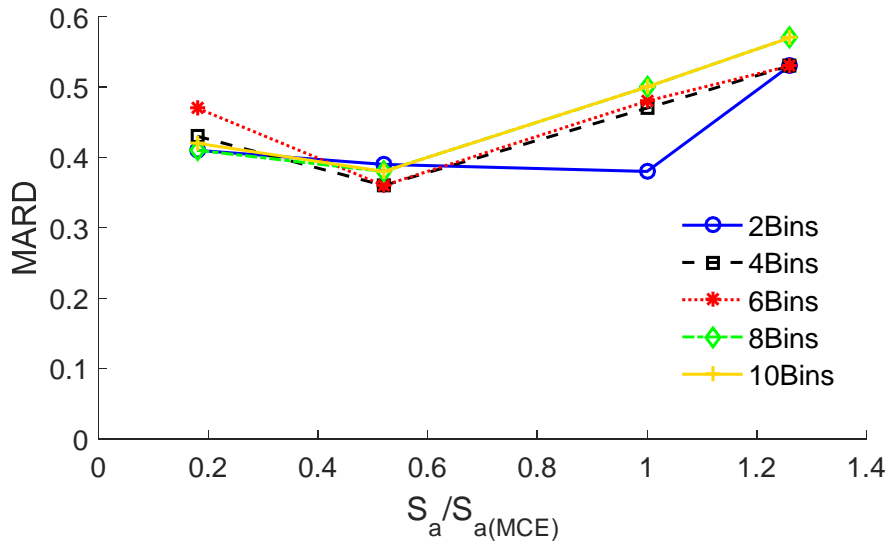
Figure 5.7. *RDR_max* MARD versus hazard level for different bin sizes

5.4.4. Verification Models

To assess the predictive performance of the surrogate models, 13 additional CRSBs are designed for different heights and parameter combinations. Eight 4-story cases and five 8-story cases with practical (but different from the ones used in the training set) design parameters values (i.e. P_D/W, F_{PT}/W, F_{yf}/W, B/H, and α) (Table 5.10) are used for this purpose.

Table 5.10. Input parameters for verification models

Model	P_D/W	F_{pt}/W	F_{yf}/W	B/H	α	N
1	0.04	0.2	0.25	0.4	0.04	4
2	0.05	0.15	0.2	0.5	0.03	4
3	0.06	0.1	0.15	0.6	0.02	4
4	0.15	0.15	0.3	0.55	0.04	4
5	0.2	0.2	0.35	0.45	0.02	4
6	0.3	0.25	0.45	0.4	0.03	4
7	0.255	0.15	0.4	0.5	0.04	4
8	0.15	0.3	0.4	0.3	0.03	4
9	0.05	0.2	0.3	0.3	0.02	8
10	0.06	0.3	0.35	0.25	0.03	8
11	0.15	0.3	0.45	0.2	0.02	8
12	0.2	0.25	0.4	0.35	0.04	8
13	0.25	0.225	0.5	0.3	0.035	8

Nonlinear response history analyses of 13 models are performed using the 80 records scaled to the four different hazard levels. The three peak responses demand parameters (SDR_{max}, PFA, and RDR_{max}) are recorded and compared with the surrogate models results obtained in the previous sections. Figure 5.8(a) and (b) the SDR_{max} and PFA MARD, respectively, as a function of the hazard level and bin size. Figure 5.8(a) shows that the accuracy of the predicted SDR_{max} is lower at higher hazard levels, which is consistent with the earlier results. For the SLE level, the MARD ranges from 0.05 to 0.12 for different bin sizes. The median MARD for the DBE, MCE, and OVE levels are approximately 0.2, 0.25, and 0.30 respectively. The accuracy of PFA is better than SDR_{max} with a MARD of approximately 0.2,

which does not change significantly with the hazard level (shown in Figure 5.8(b)). The RDR_{max} model did not perform well and is not shown.
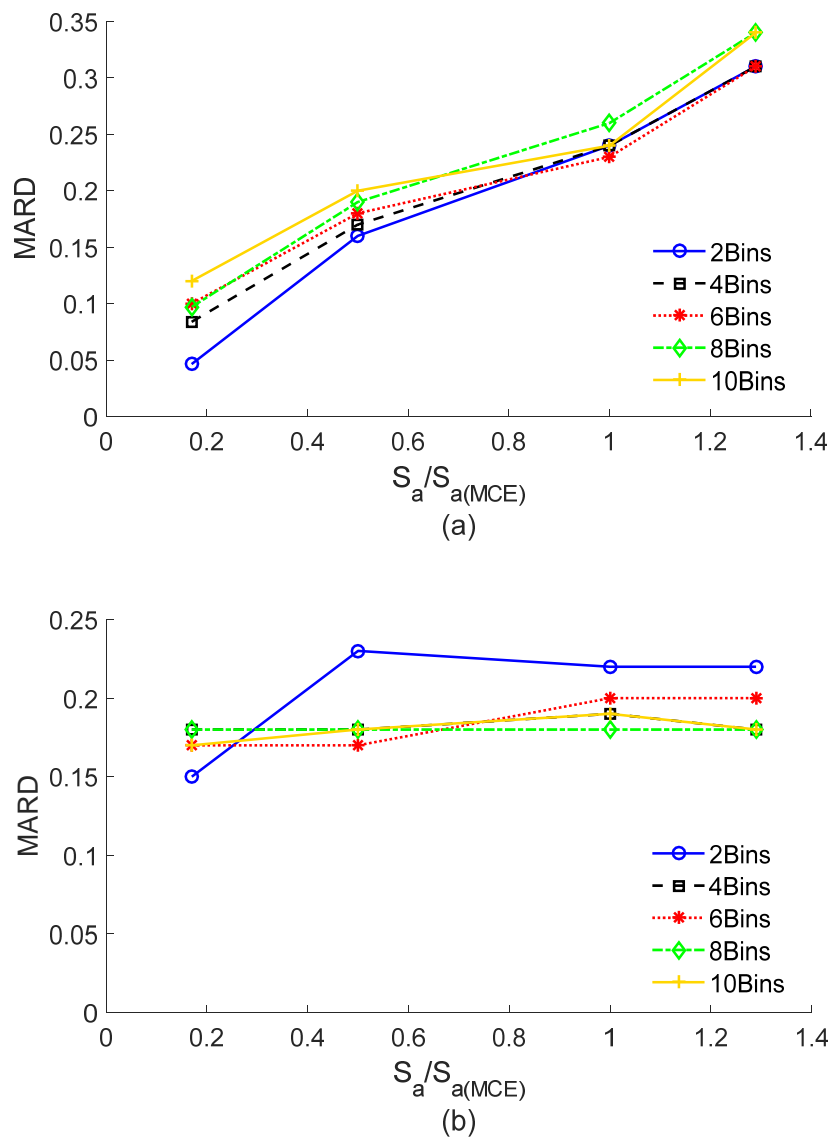
Figure 5.8. Median absolute relative deviation of verification models for various IMs and bins (a) SDR_{max} and (b) PFA

5.5.   Conclusion

A statistical approach to estimating the peak response demands in CRSBFs is proposed in this chapter. The frame aspect ratio (bay width to height ratio), *B/H*, the dead load on each column of the rocking frame, (P_D), the initial post-tensioning (*PT*) force (F_{pt}), fuse strength (F_{yf}), fuse strain hardening ratio (α), the number of stories (*N*), and the spectral acceleration at

effective period ($S_{a,Te}$), are considered as input parameters. The P_D, F_{pt} and F_{yf} are normalized by the tributary seismic weight (W). The effective period is obtained from the effective stiffness and mass of an equivalent SDOF of the CRSBF. Nonlinear response history analyses (NRHAs) of the CRBF subjected to 80 unscaled ground motions are used to obtain a training dataset of maximum story drift ratio, peak floor accelerations, and maximum residual drift. Regression analyses are used to develop the surrogate models, which serve as a compact statistical link between the structural design parameters and the maximum structural response demands. In order to consider the spectral acceleration as an input parameter, value associated with each ground motion and model effective period are sorted and grouped into bins based on different numbers of partitions (2,4,6,8, and 10). Surrogate models were constructed for each bin size and response demand parameter. To verify the surrogate models, the models are analyzed using the same ground motion set scaled to four different intensity levels: SLE, DBE, MCE, and OVE. The median of the maximum seismic demands of the 80 ground motions at each hazard level is compared to the surrogate model results. Reasonable accuracy is obtained for the maximum story drift ratio and peak floor acceleration models. However, the residual drift model was found to be unreliable. An additional verification was using 13 "unseen" building cases (4-story and 8-story). On this verification set, the surrogate models predicted the maximum story drift ratio (SDR_{max}) and peak floor acceleration (PFA) with median MARD of approximately 0.25 and 0.2 at MCE level, respectively.

CHAPTER 6:   Reliability-Based Design Methodology

Despite the significant amount of research that has been done on CRSBFs to date, there are several questions related to their design and assessment that have not been addressed. One of the least-studied aspects of CRSBFs is the ability of the braced frame components (beams, columns and braces) to avoid damage when the system experiences moderate-to-severe levels of earthquake shaking. Unlike the fuse and (to a lesser extent) post-tensioning (PT) strands, which are designed and constructed to be replaceable, repairing or replacing elements of the braced frame after an earthquake is a significant undertaking that has strong implications to direct and indirect (due to downtime) economic losses. Therefore, these components are designed using capacity-designed principles with the intent that they remain essentially elastic during moderate-to-severe ground shaking.

The research that has been done to date on the braced frame components of CRSBFs has focused on developing methodologies to estimate their design forces and mitigating the effects of higher mode response in taller buildings. In a two-part study, Wiebe and Christopoulos (2014a and 2014b) developed a performance-based design framework for CRSBFs. The first part employed a single-degree-of-freedom (SDOF) idealization of the CRSBF to design the base rocking joint with the goal of meeting a pre-defined performance objective. Part two of the study proposed a methodology for estimating peak forces in the frame elements and introduced additional mechanisms to limit the effects of higher modes. Estimating the peak force demands in the braced frame elements begins with calculating the overturning moment associated with the maximum expected rotation. After determining the appropriate number of modes to be considered and their associated modal periods, a set of equations for computing the modal contributions of the story shear and overturning moment are proposed. The modal demands are then combined using an appropriate rule. The mitigation of higher mode effects

is achieved by introducing rocking joints in the upper stories of the building or by utilizing nonlinear braces. In a follow-up study, Steele and Wiebe (2016) developed dynamic and equivalent static methodologies for capacity-design of CRSBFs. The dynamic approach combines frame member forces associated with rocking and higher mode responses. The former is obtained from a response spectrum analysis of the CRSBF using modified boundary conditions. The equivalent static procedure uses the second derivative of the closed form equations for the overturning moment to compute the distribution of inertial loads along the height of the structure. Second and third mode lateral forces are also considered. Both the dynamic and static procedures use a modified square-root-sum-of-squares approach to combine the modal forces. An alternative approach for estimating brace component demands was proposed by Martin et al. (2018). Termed the modified modal superposition (MMS) methodology, one of the key departures from the Steel and Wiebe approach was the consideration of an idealized inelastic fuse response instead of using its ultimate strength when computing the expected overturning capacity of the CRSBF. A reliability-based assessment of the force-controlled components was performed, however, the implications to system-level performance was not addressed.

This chapter proposes a reliability-based approach to determining the demand and capacity levels used to design the force-controlled components (braced frame elements) of CRSBFs. A key departure from the studies highlighted on this topic is that an explicit link between the force-controlled component behavior and system-level performance (collapse and post-earthquake structural safety). This probabilistic relationship directly informs the demand levels and (if necessary) resistance factors used to design the rocking frame elements.

6.1. Background and Relationship to Prior Work

Capacity-design principles are used to design the beams, columns and braces of the rocking frame to maximize energy dissipation and ensure that the CRSBF system responds in a ductile manner. In other words, significant inelastic deformations are restricted to the fuse and the rocking braced frame elements are designed with sufficient strength to remain essentially elastic. Unlike conventional seismic lateral force resisting systems, the CRSBF is configured such that the fuse elements are easily replaceable to minimize the direct and indirect (due to downtime) cost of structural damage. Therefore, if the elements of the rocking braced frame are damaged to the extent that repair/replacement is needed, the viability of the CRSBF as a high-performance system is compromised.

Victorsson et al. (2011) proposed a reliability-based approach to establishing capacity-design criteria for connections in steel special concentrically braced frames (SCBFs). Central to this methodology is the ability to quantify the probabilistic link between the "failure" of the force-controlled (or capacity-designed) components (e.g. SCBF connection) and system-level performance (e.g. collapse safety). Failure in this context implies that the force demands imposed on the capacity-designed component exceed its strength. These demands are generally based on the capacities of the deformation-controlled components, which are modified to incorporate uncertainties in material strength, strain hardening and other factors that can lead to actual strengths being greater than the nominal strength. In contrast to the Load and Resistance Factor Design (LRFD) methodology, which focusses only on component-level reliability, Victorsson et al. (2011) advocated for considering the impact of capacity-designed-component-failure on the performance of the entire structural system. The ultimate goal is to establish is a set of demand and capacity factors for force-controlled components that are consistent with a target system level performance.

The current study adapts the Victorsson et al. (2011) methodology to develop reliability-based capacity-design principles for CRSBFs. However, it is important to note that, aside from the difference in the considered lateral force resisting system (i.e. CRSBF versus SCBF), there are other departures from the previously developed methodology. First, in the case of SCBF brace connections, the demands are solely based on the strength of the adjacent deformation-controlled brace. However, for CRSBFs, the forces in the braced frame elements are influenced by the overturning resistance provided by the fuse, post-tensioning (PT) strands and gravity load on the frame. Furthermore, due to the rocking behavior, the relationship between these three sources of overturning resistance and the force demands in the braced frame elements is highly indeterminate. It is also noteworthy that Victorsson et al. only considered the impact of brace connection failure on SCBF collapse performance. In the current study, the post-earthquake structural safety limit is considered in addition to collapse since the CRSBF has been developed as an enhanced seismic system.

6.2. Overview of Proposed Methodology

An overview of the proposed reliability-based methodology is presented in Figure 6.1. Relevant aspects of the FEMA P695 guidelines (FEMA, 2009) (for assessing collapse performance), the FEMA P58 [FEMA, 2012] framework (for assessing post-earthquake structural safety or unsafe placard assignment) and the LRFD component reliability methodology are integrated. The goal is to determine appropriate load (γ) and resistance (ϕ) factors for the beams, columns and braces of the rocking frame that are consistent with the targets set for system level reliability. Assuming a lognormal distribution governs the probabilistic demands and capacities of the braced frame elements (Galambos et al. 1982), the LRFD methodology describes the relationship between the component reliability index (β), the load and resistance factors and the statistical demand and capacity parameters using the following equation (Victorsson, 2011).

$$\frac{\gamma}{\phi} = \frac{D_m}{D_n}\frac{C_n}{C_m} exp\left(\beta\sqrt{\sigma_{lnC}^2 + \sigma_{lnD}^2 - 2\rho\sigma_{lnC}\sigma_{lnD}}\right) \qquad (6.1)$$

D_m and C_m and D_n and C_n are the median and nominal values of the component demand and capacity, respectively, σ_{lnC} and σ_{lnD} are the lognormal standard deviations and ρ is the correlation between the demand and capacity.

Equation 6.1 can be rearranged to compute the β value that corresponds to the γ/ϕ used to design the CRSBF braced frame elements. For a predefined ground motion intensity level, D_m can be obtained from nonlinear response history analyses (NRHAs) using a median structural model that incorporates expected strengths for the yielding elements. D_n is the nominal demand on the rocking frame elements, which is computed based on the maximum expected overturning resistance provided by the PT $\left(F_{pt}\right)$ and fuse force $\left(F_f\right)$ and the gravity load on the frame (P_D). The equivalent static procedure developed by Steele and Wiebe (2016) is adopted for this purpose.

C_m/C_n represents the ratio between the median and nominal capacity of the force-controlled elements and is obtained from statistical analysis of experimental data, which is also used to determine the dispersion in the capacity of the force-controlled component (σ_{lnC}). The dispersion in the force-controlled component demand (σ_{lnD}) can include record-to-record (obtained from NRHAs) and other sources (e.g. material strength parameter) of uncertainty. However, only the former is considered in this study. Since the data needed to quantify the correlation between the demand and capacity (ρ) is unavailable, they are initially assumed uncorrelated. The effect of other assumed non-zero correlation values on the performance-outcome is also examined.

Having determined the values of the parameters in Equation 6.1, β is used to compute the failure probability for the force-controlled component of interest $[P(D > C) = \Phi(-\beta)]$, where $\Phi()$ is the standard normal cumulative distribution function. The next step is to compute the

probability of exceeding some system-level limit state when the failure of the force-controlled components is included, $P(LS_i|IM)$, (adapted from Victorsson, 2011).

$$P(LS_i|IM) = P(LS_{i,Sys}|IM) + P(LS_{i,D>C}|D > C)P(D > C|IM) \tag{6.2}$$

$P(LS_{i,Sys}|IM)$ is the probability that limit state i is exceeded conditioned on the intensity level, IM, when the failure of force-controlled components are excluded. $i = 1$ corresponds to an unsafe placard being triggered because of structural damage and $i = 2$ represents collapse. $P(LS_{i,D>C}|D > C)$ is the probability that limit state i is exceeded because of the demand exceeding the capacity in the force-controlled component and $P(D > C|IM)$ is the probability of demand exceeding capacity in the force-controlled component conditioned on the IM, which is computed using the β value from Equation 6.1. The steps needed to generate fragility functions for LS_i and $LS_{i,Sys}$ are detailed in Section 6.5. By integrating these two fragilities with an appropriate hazard curve, the limit state exceedance risks (e.g. probability of collapse in 50 years) with and without consideration given to force-controlled component failure is obtained. The incremental risk added by force-controlled component (in addition to the total risk) is used as the basis for determining the appropriate ϕ/γ to be used in the capacity-design process.

Assume value of ϕ/γ

Compute $\beta|IM$ and $P(D > C)$ using Equation 1

Develop limit state fragilities w/ and w/o force−controlled component failure i.e. $P(LS_{i,Sys}|IM)$ and $P(LS_i|IM)$

Integrate limit state fragilities with hazard curve to obtain risk e.g. $P(LS_i)_{50yrs}$ and $P(LS_{i,Sys})_{50yrs}$

Compute incremental risk due to force−controlled component failure, $\Delta P(LS_i)_{50yrs}$

Is $\Delta P(LS_i)_{50yrs}$ below acceptable threshold?

No → Increase value of ϕ/γ

Yes

ϕ/γ is adequate

Figure 6.1. Overview of framework for reliability-based determination of load and resistance factors for capacity-designed components of CRSBF

The plan view of the building cases is shown in Figure 3.2, with two CRSBFs in each direction for 3-story buildings, and four CRSBFs in each direction for 6-, and 9-story buildings, and the elevations of the three building cases are shown in in Figure 3.3(a). To evaluate the effect of force-controlled component failure on system level performance, four sets of models are needed for each building case. For one of the models, the inelastic behavior of the three force-controlled components is excluded ("All-Elastic" in Table 6.1). This model uses linear elastic beam-column elements for the braces, beams and columns. The other models are developed to consider the inelastic response for each type of force-controlled element. The combinations of inelastic versus elastic rocking frame components used in each type of model is summarized in Table 6.1. The models identified as "Brace-NL", "Beam-NL", and "Column-

NL" only consider material nonlinearity in braces, beams, and columns respectively. For the "All-Inelastic" model, material nonlinearity is incorporated in all three force-controlled elements.

For the models where their inelastic response is considered, the beams, columns, and braces are represented using fiber cross sections that incorporate the Giufrré–Menegotto–Pinto material model with 0.3% strain hardening and expected strengths of $R_y F_y$ $(R_y = 1.1$ and $F_y = 308.2 \ N/mm^2)$. Brace buckling is captured by incorporating corotational transformations and initial imperfections.

Table 6.1. Summary of model cases with and without consideration of inelastic response in force-controlled components

Model ID	Braces				Beams		Columns	
	Elastic Elements	Nonlinear Elements	Initial Imperfection	Fracture Considered	Elastic Elements	Nonlinear Elements	Elastic Elements	Nonlinear Elements
All-Elastic	√	x	x	x	√	x	√	x
All-Inelastic	x	√	√	√	x	√	x	√
Brace-NL	x	√	√	√	√	x	√	x
Beam-NL	√	x	x	x	x	√	√	x
Column-NL	√	x	x	x	√	x	x	√

√: Included in model

x: Not included in model

Note that the section sizes of force-controlled members (beams, braces, and columns) are selected based on the maximum permissible demand to capacity ratio. In real projects where efficiency in construction is also considered, more conservative designs may be used. The sizes of the beams, columns, and braces for different load-resistance ratio are listed in Appendix.

6.3.   Seismic Hazard, Ground Motions and Nonlinear Response History Analyses

The results from nonlinear response history analyses are to compute the reliability index (more specifically, D_m) for the force-controlled components (Equation 6.1) and the system-level limit state fragility functions (Equation 6.2). The forty-four (twenty-two pairs) far-field ground motions specified in the FEMA P695 (FEMA 2009) guidelines are used for this

purpose. Figure 6.2(a) shows the response spectra for the suite of unscaled ground motions along with the median response spectra.

To support a risk-based assessment of the impact of force-controlled component failure on system performance, a site-specific hazard curve is incorporated based on Sa_{T1}. The hazard curve for a Los Angeles site (33.58, -118.19) corresponding to the first-mode periods of the three building cases is shown in Figure 6.2(b).
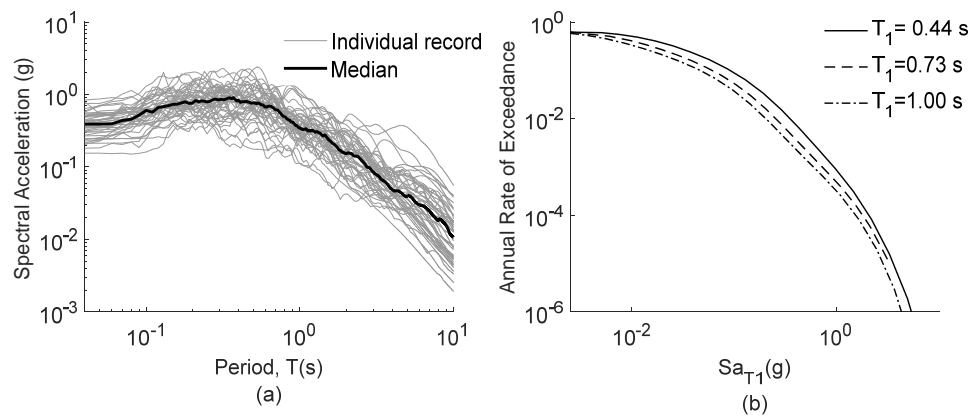
Figure 6.2. (a) Response spectra for FEMA P695 far-field ground motions and (b) hazard curves based on $\boldsymbol{Sa_{T1}}$ corresponding to the first-mode periods of the three building cases

The spectral acceleration corresponding to the first mode period (Sa_{T1}) is used as the ground motion intensity measure (IM). The first three modal periods for the 3-, 6- and 9-story models are summarized in Table 3.2 along with the Sa_{T1} corresponding to the MCE hazard level (S_{MT}).

6.4.   Application of Reliability-Based Capacity Design Methodology

This section applies the reliability-based methodology to the three building cases. As previously noted, the outcome is a quantitative relationship between ϕ/γ and the system-level vulnerability and risk-based performance. Initially, the procedure is described and intermediate results are presented for the case where $\phi/\gamma = 0.9$ ($\phi = 0.9$, $\gamma = 1$) and $\rho = 0$. The results for a range of ϕ/γ values are summarized and discussed and the implications of non-zero ρ

values are also examined. Note that $\phi = 0.9$ is the default resistance factor for steel compression components, which is specified in Chapter E1 of AISC-341 (AISC 2016). The value of γ reflects the hazard-level that is used to determine the design forces for the force-controlled components. In prior studies (e.g., Eatherton and Hajjar 2010; Ma et all 2011; Steele and Wiebe 2016), the MCE hazard level has been used as the default and is therefore associated with $\gamma = 1$ herein. The γ value for other hazard levels is taken as the ratio between the corresponding Sa_{T1} and S_{MT}. Since ϕ is structural-system-agnostic and assessed based on a broad set of considerations not explicitly related to CRBFs, it is assumed that a value of 0.9 will always be used. Therefore, the target ϕ/γ will be achieved by considering γ as the variable parameter. In other words, the hazard level used to determine the force-controlled component design forces will be the control factor that is used to achieve the desired ϕ/γ value.

6.4.1. Computing β and P(D>C)

The value of β and $P(D > C)$ corresponding to $\phi/\gamma = 0.9$ is computed for a range of intensity levels. For this purpose, incremental dynamic analyses (IDAs) are performed using the structural model where the inelastic response of the force-controlled components is not included ("All Elastic" in Table 6.1). In other words, the beams, columns and braces of the rocking frame are modeled using linear elastic elements. The ground motions are scaled individually such that the Sa_{T1} matches the target intensity level, which are increased at increments corresponding to 10% of S_{MT} up to the collapse point. For the rocking frame beams, columns, and braces the maximum axial demand in each story is recorded.

Using the results from the set of forty-four ground motions, the median (D_m) and log-standard deviation (σ_{lnD}) of the demand in each type of element is computed. C_m/C_n is taken as 1.87 (Fell et al. 2006) and σ_{lnC} is taken as 0.15 (Victorsson et al. 2011) for the axial capacity of the members. D_n is computed using the Steele and Wiebe (2016) methodology described

earlier. The D_m/D_n profile for each force-controlled component corresponding to S_{MT} is presented in Figure 6.3. It is observed that the D_m/D_n profile for all three types of elements is fairly uniform and is capped at a value of approximately 1.0, indicating that the Steele and Weibe methodology provides reasonable estimates of the 50th percentile force demands in capacity-designed components.
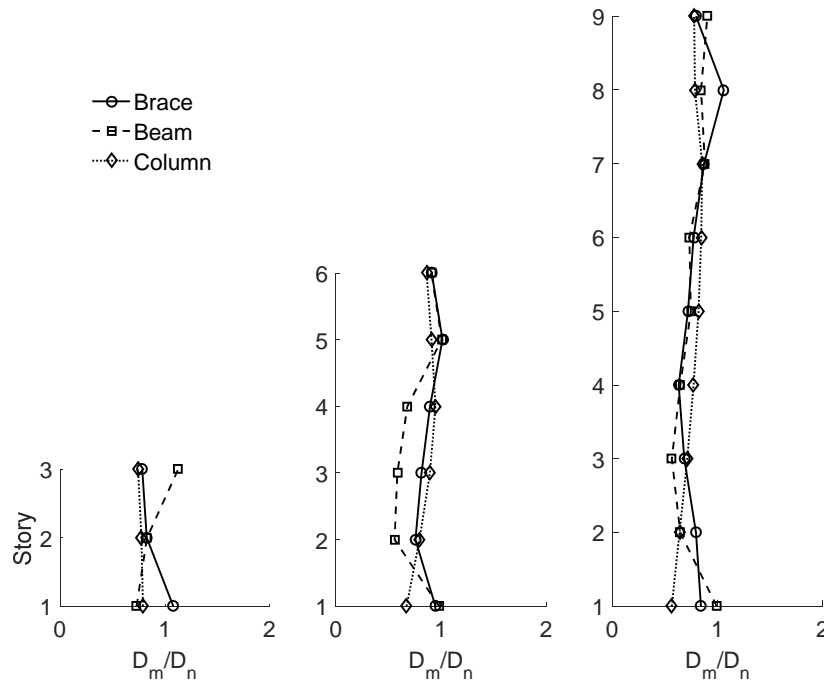
Figure 6.3. Vertical profile D_m/D_n at the MCE level for all force-controlled components

Equation 6.1 is used to compute the value of β conditioned on the intensity-level and component type. The β values are then used to obtain $P(D > C)$ using the following relationship: $P(D > C) = \Phi(-\beta)$. Figure 6.4 shows plots of the maximum-value envelope (i.e. maximum value at each intensity considering all elements in all stories) of $P(D > C)$ versus Sa_{T1} normalized by the S_{MT}, for the axial force in the braces, beams and columns. For the 3-,6-, and 9- story buildings, $P(D > C)$ is generally highest in the beams and braces. For the latter, the MCE level $P(D > C)$ is 0.38, 0.37 and 0.34 for the 3-, 6- and 9-story building, respectively. At the same intensity, the $P(D > C)$ values in the beams are 81% of the brace

values. The columns have the lowest $P(D > C)$ with MCE level values of 0.036, 0.044 and 0.028 for the 3-, 6- and 9-story buildings, respectively. The lower $P(D > C)$ values in the columns relative to the beams and braces is explained by comparing the dispersion in the force demands in the three components which is one of the inputs in Equation 6.1. More specifically, the dispersion in the column force demands (σ_{lnD}) is approximately 30% that of the beams and braces at the MCE level.
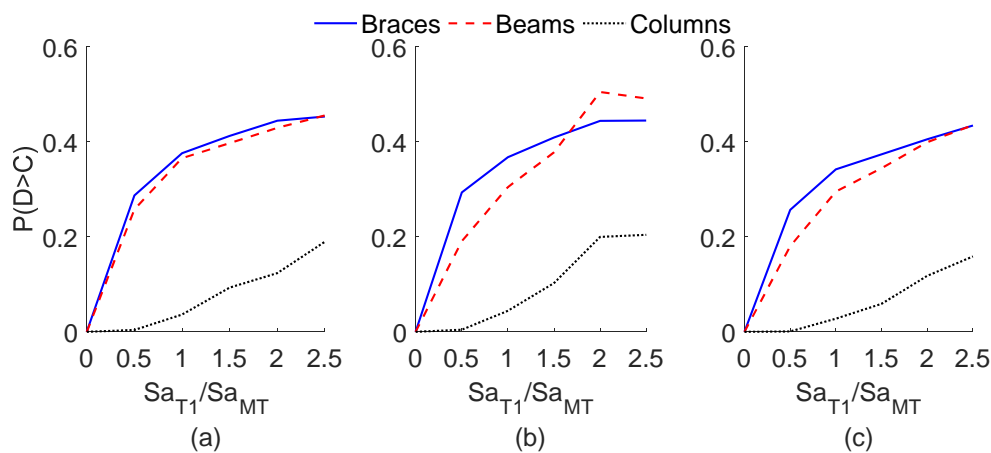
Figure 6.4. Maximum of $P(D > C)$ versus Sa_{T1}/Sa_{MCE} corresponding to axial forces in force-controlled components (a) 3-, (b) 6- and (c) 9-story building cases

6.5. Impact of Force-Controlled Component Failure on System-Level Performance

The impact of force-controlled component behavior on the CRSBF system-level performance is quantified by computing the incremental risk caused by failure of the rocking frame beams, columns and braces. The first step in this sub-process is to develop limit state fragility functions with and without considering failure in each of these components. Collapse and post-earthquake structural safety (or unsafe placard triggered by structural damage) are the two system-level limit states considered. The expectation is that the CRSBF capacity-design criteria will be different for the two limit states. More specifically, if the same acceptable risk-

threshold is assumed, the required ϕ/γ is expected to be smaller (i.e. a more conservative design) for the unsafe placard limit state.

6.5.1. Collapse safety

Collapse fragility functions are developed without considering force-controlled component failure $\left[\text{i.e.}\ P\left(Collapse_{Sys}|IM\right)\right]$ using the same structural model (All-Elastic) and IDA results described earlier. Recall that, for the numerical model corresponding to each building case, the ground motion records are scaled at increments of 10% relative to S_{MT} up to collapse. At each intensity level, the maximum drift demand over all stories is recorded. The collapse criteria is taken as (1) the occurrence of dynamic instability (slope of IDA curve is very small) or (2) the maximum story drift exceeds 10% (Steele and Wiebe 2017). The fraction of collapses at each intensity level is computed and used to obtain the maximum likelihood estimate of the median $\left(\hat{S}_{CT,Sys}\right)$. The record-to-record dispersion value suggested by the FEMA P695 guideline, $\beta_{RTR} = 0.4$, is adopted. The total dispersion in the collapse intensity (β_{TOT}) is taken as the square-root-sum-of-squares combination of β_{RTR} and additional uncertainties that result from the robustness of the design requirements $(\beta_{DR} = 0.2)$, accuracy of test data $(\beta_{TD} = 0.2)$ and model parameters $(\beta_{MDL} = 0.2)$ assuming a "good" rating (FEMA 2009). The spectral shape factor (SSF) is applied to $\hat{S}_{CT,Sys}$ based on the ductility ratios obtained from pushover curves generated using nonlinear static analyses (FEMA 2009). The SSF for the 3, 6, and 9 story CRSBFs are 1.33, 1.39, and 1.46 respectively. Figure 6.5 shows the fragility curve obtained from the All-Elastic model for the three building cases after incorporating SSF and β_{TOT}. The intensity levels on the horizontal axis are normalized by the S_{MT}. The 3-, 6-, and 9-story buildings have adjusted collapse margin ratios $\left(\text{CMR}_{Sys}\right)$ of 3.1, 4.5, 5.0 respectively. Generally, the CMR is higher for taller buildings, which is consistent with the findings of prior studies (e.g. Rahgozar et al. 2016, Steel and Weibe, 2017).
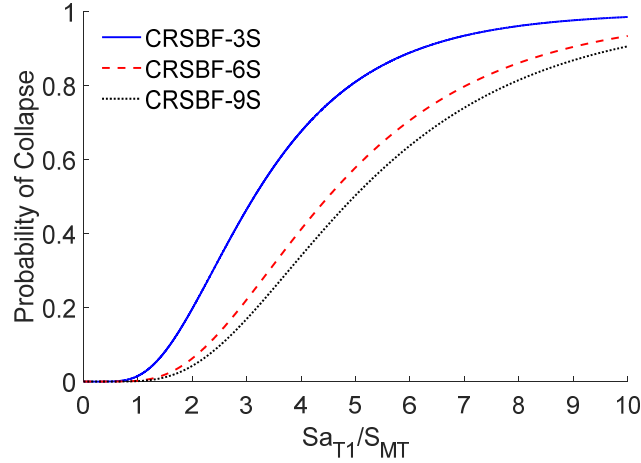
Figure 6.5. Collapse fragility curves for "All-Elastic" 3-, 6- and 9 story buildings cases i.e. force-controlled component failure not considered

Multiple numerical models and analysis cases are needed to compute the incremental collapse fragility caused by force-controlled-component-failure [i.e. $P(Collapse_{D>C}|D > C)P(D > C|IM)$]. A different structural model is needed for each type of component and loading mechanism. For instance, to assess the relationship between brace ϕ/γ and collapse performance, the All-Elastic and Brace-NL models (Table 6.1) are used. Using the All-Elastic model, $P(D > C|IM)$ at each intensity level is obtained from the results shown in Figure 6.4. From these same analyses, the ground motions that do not cause collapse but the brace axial force demand exceeds the nominal capacity are identified. Denoted as $[GMs_{D>C,\overline{Collapse}}|IM]$, this subset of ground motions is used to perform IDAs on the Brace-NL model. At each intensity level, $P(Collapse_{D>C}|D > C)$ is computed as the fraction of collapse cases relative to the $[GMs_{D>C,\overline{Collapse}}|IM]$ record-set. Finally, the incremental collapse fragility caused by brace axial failure is computed as $P(Collapse_{D>C}|D > C)P(D > C|IM)$. This process is repeated using Beam-NL and Column-NL, which consider axial failure in the beams and columns. Figure 6.6 shows collapse fragility curves for all three building cases with and without considering beam, column and brace failure. For the 3-story case, column failure has the largest effect, reducing the adjusted CMR by 14% , while beam failure has a negligible

63

effect on collapse performance. For the 6-story case, the effect of column and beam failure is negligible while brace failure has the greatest effect, reducing the adjusted CMR by 12%. For the 9-story building the overall effect of the force-controlled components failure is negligible. This is explained by the fact that the taller buildings are more susceptible to sidesway collapse caused by higher P-Δ effects.
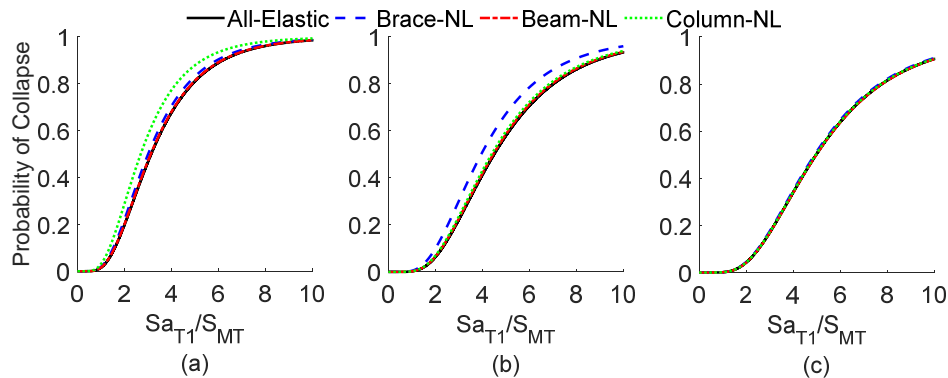
Figure 6.6. Collapse fragility curves with and without consideration of force-controlled component failure for the (a) 3-, (b) 6- and (c) 9-story building cases

6.5.2. Unsafe placard triggered by structural damage (Post Earthquake Structural Safety)

In addition to collapse, we also examine the effect of ϕ/γ on the probability that an unsafe placard is assigned to the building because of structural damage. The framework developed by FEMA P58 (FEMA 2012) is adopted for this purpose. First, the structural components that will be considered as potential *unsafe placard triggers* (UPTs) are identified. NRHAs are then performed and the engineering demand parameters (EDPs) associated with these potential UPT components are recorded. These EDPs are coupled with fragility functions to simulate realizations of component-level damage. A single realization of building damage is described by each UPT being assigned a component-level damage state. The triggering ratio is the fraction of a specific component-type in each damage state that would prompt an unsafe placard (FEMA 2012). For example, the UPT limit state is triggered when 40% of braces are in damage state 2 or 20% are in damage state 3 (FEMA 2012). The probability of an unsafe

placard conditioned on the ground motion intensity is taken as the fraction of building damage realizations for which the triggering ratio for at least one UPT is exceeded.

Note that FEMA P58 groups the elements of a braced frame to define the UPT. In other words, the damage state descriptions and triggering ratios are defined for the entire frame and not the individual elements (beams, columns and braces). Therefore, unlike the collapse limit state, the relationship between ϕ/γ and the likelihood of an unsafe placard being assigned is established for the entire frame (as opposed to the individual elements). In addition to the force-controlled braced frame elements, the PT strands and fuse are also considered as UPT components. The damage state IDs, descriptions, median and dispersion of the associated EDP limits and triggering ratios for each UPT-component are summarized in Table 6.2. The EDP limits and triggering ratio for the braced frame are from the FEMA P58 guideline. PT yielding and the onset of strength degradation in the fuse are adopted as UPTs assuming the deterministic EDP limits specified earlier.

Like the collapse limit state, the unsafe placard fragility function without the consideration of force-controlled component failure $\left[\text{i.e.}\, P\left(Unsafe_{Sys}|IM\right)\right]$ is generated using the analysis results from the ALL-Elastic model. The force-controlled components are excluded as UPTs in this assessment case. Using the EDPs from the IDAs described earlier and the damage fragility parameters in Table 6.2, 1000 realizations of building damage are generated using Monte Carlo simulation. The number of realizations is chosen to minimize the variance in the Monte Carlo estimates of $P\left(Unsafe_{Sys}|IM\right)$. Recall that a single realization of building damage corresponds to each UPT component being assigned a damage state. $P\left(Unsafe_{Sys}|IM\right)$ is then computed as the fraction of realizations for which the triggering ratio is exceeded for at least one UPT component. To compute $P(Unsafe|IM)$, the overall process is repeated using the All-Inelastic model.

The unsafe placard fragility caused by force-controlled component failure is directly computed. In other words, instead of computing $P(Unsafe_{D>C}|D > C)P(D > C|IM)$ and adding it to $P(Unsafe_{Sys}|IM)$ (as was done the collapse limit state), $P(Unsafe|IM)$ is obtained directly by applying the assessment process incorporating the grouped force-controlled components as a UPT. For instance, to compute $P(Unsafe|IM)$, the EDPs produced from IDAs on the All-Inelastic model are utilized. Building damage realizations are then generated incorporating braced frame failure as a UPT (in addition to the deformation-controlled components). To perform IDAs, ground motions are scaled until an unsafe placard is triggered for at least half of the ground motions. Unsafe placard fragility functions developed with and without considering all force-controlled components, are shown in Figure 6.7 for the three buildings. As expected, the median intensity level associated with the UPT limit state is much lower (by factors ranging from 2.5 to 2.7) than for collapse. However, Figure 6.7 shows that force-controlled component failure has a negligible effect on the UPT limit state for all three building cases. The lower intensity levels associated with the UPT limit state (compared to collapse) and the generally low $P(D > C)$ values shown in Figure 6.4 (even up to the MCE hazard level) explains the negligible effect of force-controlled component failure observed in Figure 6.7. In other words, the capacity-design procedure that is implemented for the braced frame components minimizes their potential influence on the UPT limit state.

Table 6.2. UPT-components, damage states, EDP limits and triggering ratios

Element	Damage State			EDP Limit		
	ID	Description	Triggering Ratio/Value	Type	Median	Dispersion
Forced- controlled elements i.e. beams, columns and braces	FC-DS-1	Initiation of brace buckling and yielding of gusset plates.	NA[1]	Story Drift Ratio	0.00159	0.7
	FC-DS-2	Brace buckling.	0.4		0.01	0.3
	FC-DS-3	Fracturing of braces and bolts of beam-column connections. Torn gusset plates, and local buckling of frame members.	0.2		0.0178	0.3
PT	PT-DS-1	Yielding of PT strands	1.0	Strain	0.0086	NC[2]
Fuse	FS-DS-1	Onset of strength degradation in fuse	1.0	Shear Def.	0.35	NC

[1]NA: Damage state cannot tirgger an unsafe placard

[2]NC: Disperion not considered
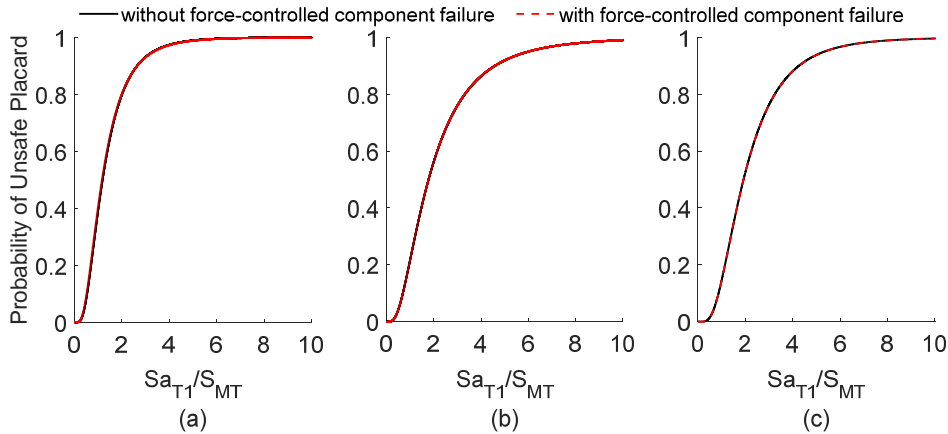
Figure 6.7. Unsafe placard fragility curves with and without the consideration of force-controlled component failure for (a) 3-, (b) 6- and (c) 9-story building cases

Figure 6.8 shows a disaggregation of each building's vulnerability to an unsafe placard assignment based on the type of component for the 3, 6, and 9 story CRSBFs. The vertical axes of these plots represent the probability that an unsafe placard is triggered by each UPT at different intensity levels. These are not mutually exclusive events (i.e. an unsafe placard can be triggered by more than one UPT). As such, the sum of the probabilities across all UPTs is not equal to the probability when all UPTs are considered simultaneously. Figure 6.8 shows that, compared to the PT, the fuse is more likely to trigger an unsafe placard. For the 3-story building case, the probability that an unsafe placard is triggered at the MCE intensity level by the individual components is 50% higher for the fuse compared to the PT. Moreover, this difference increases with the building height. For the 9-story case, the probability that the fuse and PT triggers an unsafe placard at the MCE is 11% and almost zero, respectively. This major

difference can be partially explained by observing (in Figure 6.8) that the effect of PT failure on the unsafe placard limit state decreases significantly going from the 3- to the 9-story building case. More specifically, for the same uplift demand, the PT strain is lower in the taller frame and yielding is much less likely. Consistent with Figure 6.7, the probability of an unsafe placard being triggered by force-controlled component failure is small but increases with the building height. In fact, in the 9-story building case, the effect is slightly higher compared to the PT. The more significant influence of force-controlled component failure on the UPT limit state in taller buildings can be explained by the increase in higher mode effects and reduction in the desirable rigid body rotation behavior.
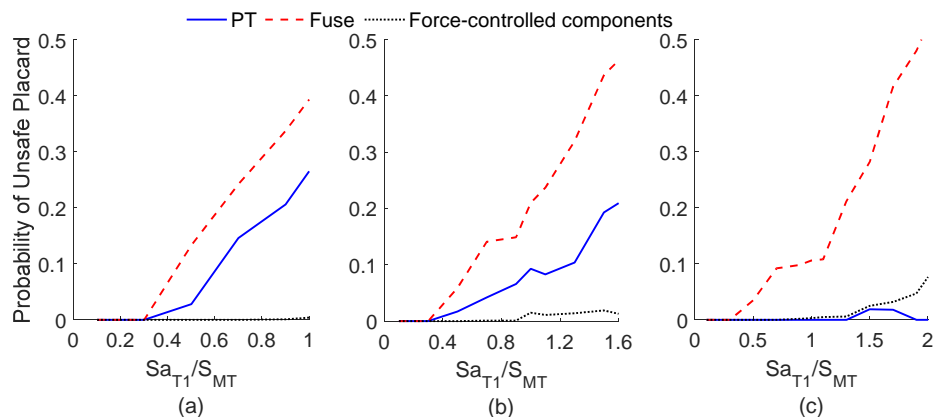
Figure 6.8. Probability of unsafe placard triggered by deformation and force-controlled components for the (a) 3-, (b) 6- and (c) 9-story building cases

6.5.3. Risk-based assessment of impact of force-controlled component failure on system-level performance

The load and resistance factors for the force-controlled components are determined based on the extent to which they contribute to the risk of limit-state (collapse and unsafe placard) exceedance over the service-life of the CRSBF building. The mean annual frequency of limit state exceedance, $\lambda_{LS,i}$, is computed by integrating the respective fragility function with the site-specific hazard curve. The discrete form of this integration can be written as

$$\lambda_{LS,i} = \sum_{All\ IM} P(LS_i|IM) \cdot \left|\frac{d\lambda(IM)}{d(IM)}\right| \cdot \Delta IM \tag{6.3}$$

$\frac{d\lambda(IM)}{d(IM)}$ is the slope of the hazard curve and ΔIM is the intensity measure increment used in the numerical integration. The $\lambda_{LS,i}$ value computed using Equation 6.3 includes the effect of force-controlled component failure. The mean annual frequency of limit state exceedance can be computed without considering force-controlled component failure by replacing $P(LS_i|IM)$ with $P(LS_{Sys,i}|IM)$ in Equation 6.3. Given $\lambda_{LS,i}$, the probability of limit state exceedance over a 50-year service life is computed as

$$P(LS_i)_{50yrs} = 1 - exp(-\lambda_{LS,i} \cdot 50) \tag{6.4}$$

Figure 6.9 shows how each type of force-controlled component affects the 50-year probability of collapse over a range of ϕ/γ values where $\frac{\phi}{\gamma} = 0$ corresponds to the case where force-controlled component failure is not considered and $\frac{\phi}{\gamma} = 0.9$ is the value that is the basis of current design standards (i.e. ASCE 7-16 and AISC 341-16). Recall that $\frac{\phi}{\gamma} = 0.9$ corresponds to $\gamma = 1$ and $\phi = 0.9$. Also, the $\gamma = 1$ represents the case where MCE-level demands are used to design the force-controlled components. Using the relationship between the γ and the hazard level used to design the force-controlled components described earlier and assuming ϕ is always equal to 0.9, the return period for each $\frac{\phi}{\gamma}$ value (shown in the lower horizontal axis) is shown in the upper horizontal axis. As such, the target $\frac{\phi}{\gamma}$ can be described in terms of the return period of the hazard level used to design the force-controlled components.

As expected, the collapse risk generally increases with the value of ϕ/γ. Recall that higher values of ϕ/γ corresponds to lower γ values and hazard levels (less conservative force-controlled component design). For 3-story building, column failure has a significant effect on

collapse risk, which is consistent with Figure 6.6. For 6-, and 9-story buildings beam failure has a modest effect on collapse risk at higher $\frac{\phi}{\gamma}$ values. As indicated earlier, taller buildings are more susceptible to P-Δ-triggered or sidesway collapse compared to shorter buildings, which reduces the overall influence of force-controlled component failure for this limit state. The 50-year collapse risk for all three cases remains below the 1% threshold that is implied in modern design codes and standards (e.g. ASCE, 2016).
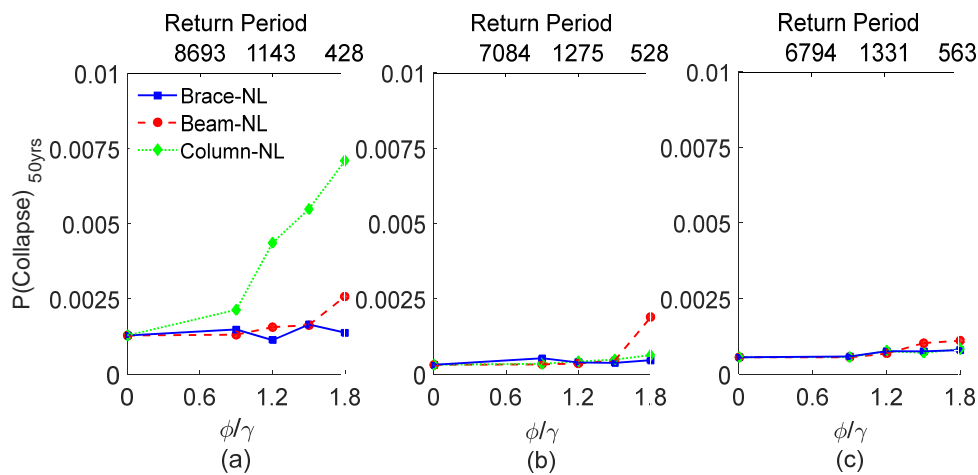
Figure 6.9. Effect of ϕ/γ (and corresponding return period) on the probability of collapse in 50 years for the (a) 3-, (b) 6- and (c) 9-story building cases

The effect of ϕ/γ on the probability that the CRSBF building is assigned an unsafe placard within a 50-year period is shown in Figure 6.10. Similar to Figure 6.9, $\phi/\gamma = 0$ corresponds to the case where force-controlled component failure is not considered and the return period corresponding to each ϕ/γ is shown in the upper horizontal axis. When force-controlled component failure is not considered, the 50-year probability of an unsafe placard is 3.1%, 1.5% and 1.1% in the 3-, 6- and 9-story building cases, respectively. For the 3-story building, there is a dramatic increase in the effect of force-controlled component failure on the 50-year probability of an unsafe placard between ϕ/γ values of 1.2 and 1.8. However, for the taller building cases, there is not an appreciable change in the effect of force-controlled component

70

failure on the UPT limit state as ϕ/γ increases. At first glance, the much greater effect of force-controlled component failure on UPT risk in the 3-story building (compared to the 6- and 9-story) appears to be inconsistent with the results in Figure 6.8, which shows that force-controlled components are more likely to trigger an unsafe placard in taller buildings. However, Figures. 6.8 and 6.7 also show that the triggering effect of the PT and fuse "masks" that of the force-controlled components for the UPT limit state. Moreover, because the shorter buildings are dominated by first mode (or rigid-body-rotation) behavior, the increasingly nonlinear response caused by force-controlled component failure leads to higher roof drift demands, PT strains and fuse deformations. In contrast, because of the greater contribution of higher modes in taller buildings, while force-controlled component nonlinearity leads to higher story drifts, the effect on roof drift demands, PT strains and fuse deformations is smaller.

The 50-year probability of an unsafe placard when $\frac{\phi}{\gamma} = 0.9$ (the value implied by the current design codes and standards) is 3.5%, 1.5% and 1.1% for the 3-, 6- and 9-story building cases, respectively. Note that, unlike collapse, current design codes and standards do not consider the risk of an unsafe placard and therefore no limit is provided. However, given that the CRSBF is being developed as a high-performance seismic system, this limit state should be given high priority when developing design guidelines.
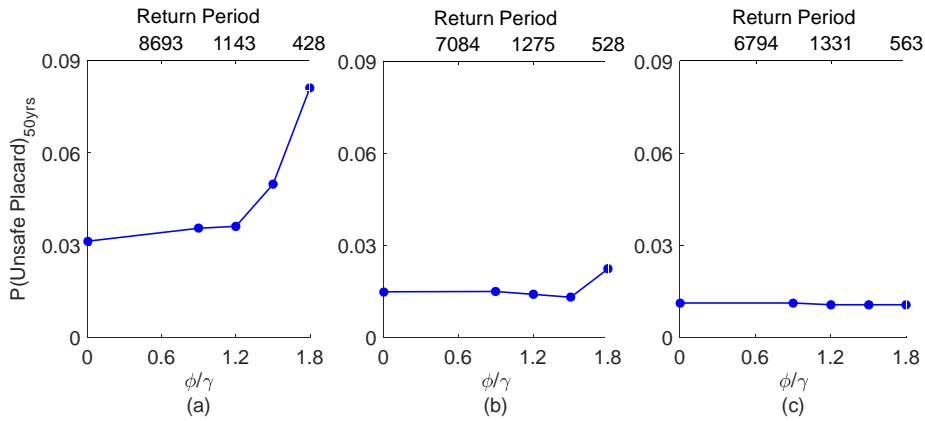
Figure 6.10. Effect of ϕ/γ (and the corresponding return period) on the probability of an unsafe placard being assigned within a 50-year period for the (a) 3-, (b) 6- and (c) 9-story building cases

6.5.4. Effect of assumed demand-capacity on system-level risk-based performance

In the previous assessments of the effect of force-controlled component failure on system-level performance, the correlation between the demand and capacity was assumed to be zero. In this section, the effect of non-zero demand-capacity correlation is examined. More specifically, the ratio of the 50-year collapse probability at $\frac{\phi}{\gamma} = 0.9$ between the cases where $\rho = 0$ and $\rho = 1$ $\left[P(Collapse)_{50yrs,\rho=0}/P(Collapse)_{50yrs,\rho=1} \right]$ is computed and shown in Figure 6.11. Based on Equation 6.1 and assuming all other variables are unchanged, a higher ρ would lead to an increase in β and a reduction in probability of failure at the component-level i.e. a smaller $P(D > C)$. This is consistent with the results in Figure 6.11, which shows that $P(Collapse)_{50yrs,\rho=0}/P(Collapse)_{50yrs,\rho=1}$ is approximately 1.0 or higher. Recall that the dispersion in the beam and brace demands are significantly higher than the column. This higher dispersion "masks" the effect of the non-zero ρ value. However, for the columns, the effect of the non-zero demand-capacity correlation is more pronounced because of the lower dispersion. The higher column demand dispersion in the taller buildings also explains why the effect of the non-zero demand-capacity correlation diminishes as the building height increases.

72

Ultimately, it should be noted that the effect of demand-capacity correlation on collapse risk is minimal, reducing $P(Collapse)_{50yrs}$ by a maximum of approximately 15%.
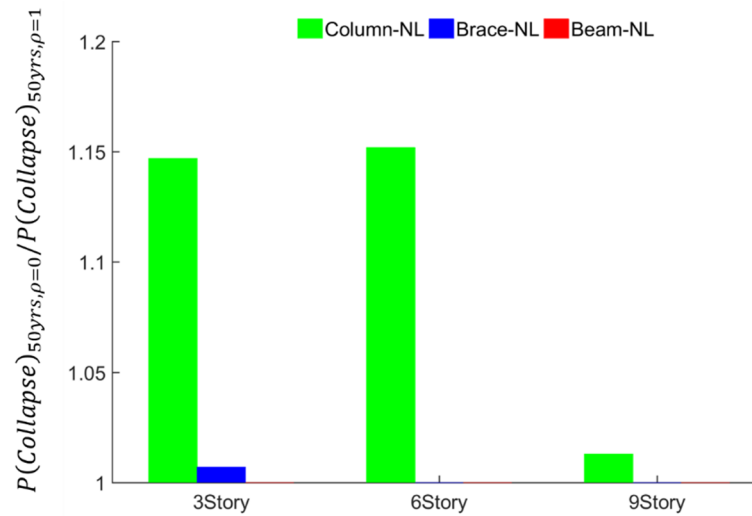
Figure 6.11. Ratio of the probability of collapse in 50 years when $\rho = 0$ $\left(P(\text{Collapse})_{50yrs,\rho=0}\right)$ to the value when $\rho = 1.0$ $\left(P(\text{Collapse})_{50yrs,\rho=0}\right)$ for the (a) 3- (b) 6- and (c) 9-story building cases

6.6.   Conclusion

To achieve the desired goal of reducing building downtime and functional disruption, earthquake-damage to the forced-controlled components in controlled rocking steel braced frames (CRSBFs) should be minimal. Towards this end, a reliability-based approach to designing CRSBF force-controlled components (i.e. frame beams, columns and braces) is presented. Central to the proposed methodology is establishing an explicit link between the failure of these components and the CRSBF system-level performance. Collapse and post-earthquake structural safety (or unsafe placard assignment) are the two considered system-level limit states. A case study is presented whereby the newly developed methodology is applied to 3-, 6- and 9-story building cases.

The effect of frame beam, column and brace failure on the vulnerability to collapse and unsafe placard triggering (UPT) was first assessed for a resistance and load factor ratio of $\frac{\phi}{\gamma} =$

0.9 (the value implied by current standards). The effect of column failure on the collapse vulnerability of 3-story building was stronger compared to the beams and braces. Whereas for the 6-story building, brace failure had largest effect, and for the 9-story building, force-controlled component failure did not have significant effect on collapse performance. The effect of force-controlled component failure on the UPT limit state was found to be negligible for all three cases at $\frac{\phi}{\gamma} = 0.9$. The ratio of adjusted collapse margin ratio (CMR) with and without considering force-controlled component failure ranged from 0.86 to 1.0 at $\frac{\phi}{\gamma} = 0.9$, while the same ratio for the UPT limit state ranged from 0.98 to 1.0. Furthermore, a disaggregation of the UPT vulnerability showed that the deformation-controlled components (fuse and PT) were much more likely to trigger an unsafe placard compared to the force-controlled components. For both limit states, the effect of force-controlled component failure was found to be lower for taller buildings.

A risk-based assessment of the effect of force-controlled component failure was conducted for $\frac{\phi}{\gamma} = 0.9, 1.2, 1.5$ and 1.8. For the full range of considered ϕ/γ values, the 50-year collapse probability remained below the 1% threshold prescribed by current building codes even when force-controlled component failure was considered. When force-controlled component failure is not considered, the probability that an unsafe placard is triggered within a 50-year period ranges from 1.1% in the 9-story to 3.1% in the 3-story building. For the $\frac{\phi}{\gamma} = 0.9$ case, the 50-year probability of exceeding the UPT limit state remained unchanged (relative to when force-controlled component failure is ignored) in the 9-story building but increased to 3.5% in the 3-story building. The force-controlled component demand-capacity correlation was found to minimally affect their relationship to system-level performance.

Appendix

Table A.1. List of columns, braces, and beams

Model	Story	φ/γ=0.9 Column sections	Brace sections	Beam sections	φ/γ=1.2 Column sections	Brace sections	Beam sections
CRSBF-3S	1	W14x99	W14x99	W14x61	W14x90	W14x82	W14x48
	2	W14x90	W14x61	W14x43	W14x68	W14x43	W14x34
	3	W14x22	W14x90	W14x38	W14x22	W14x74	W14x30
CRSBF-6S	1	W14x193	W14x132	W14x53	W14x145	W14x99	W14x48
	2	W14x159	W14x82	W14x53	W14x132	W14x61	W14x48
	3	W14x145	W14x61	W14x53	W14x99	W14x53	W14x43
	4	W14x99	W14x61	W14x43	W14x90	W14x53	W14x38
	5	W14x74	W14x61	W14x43	W14x61	W14x48	W14x34
	6	W14x22	W14x90	W14x34	W14x22	W14x68	W14x30
CRSBF-9S	1	W14x370	W14x193	W14x68	W14x283	W14x145	W14x61
	2	W14x342	W14x99	W14x68	W14x257	W14x82	W14x61
	3	W14x311	W14x90	W14x68	W14x233	W14x74	W14x53
	4	W14x283	W14x82	W14x61	W14x211	W14x61	W14x48
	5	W14x233	W14x74	W14x53	W14x176	W14x61	W14x43
	6	W14x193	W14x74	W14x53	W14x145	W14x61	W14x43
	7	W14x145	W14x68	W14x43	W14x109	W14x61	W14x38
	8	W14x99	W14x61	W14x68	W14x90	W14x53	W14x53
	9	W14x22	W14x120	W14x34	W14x22	W14x90	W14x30

Model	Story	φ/γ=1.5 Column sections	Brace sections	Beam sections	φ/γ=1.8 Column sections	Brace sections	Beam sections
CRSBF-3S	1	W14x68	W14x68	W14x43	W14x61	W14x61	W14x38
	2	W14x61	W14x43	W14x34	W14x53	W14x38	W8x21
	3	W14x22	W14x61	W8x24	W14x22	W14x61	W8x21
CRSBF-6S	1	W14x120	W14x90	W14x43	W14x99	W14x74	W14x38
	2	W14x99	W14x61	W14x43	W14x90	W14x53	W14x38
	3	W14x90	W14x43	W14x34	W14x82	W14x43	W14x30
	4	W14x68	W14x43	W14x30	W14x61	W14x43	W14x30
	5	W14x53	W14x43	W14x30	W14x48	W14x38	W8x18
	6	W14x22	W14x61	W8x24	W14x22	W14x53	W8x21
CRSBF-9S	1	W14x233	W14x120	W14x48	W14x193	W14x99	W14x43
	2	W14x211	W14x68	W14x48	W14x176	W14x61	W14x43
	3	W14x193	W14x68	W14x43	W14x159	W14x61	W14x43
	4	W14x176	W14x61	W14x43	W14x145	W14x53	W14x38
	5	W14x145	W14x53	W14x43	W14x120	W14x43	W14x34
	6	W14x120	W14x53	W14x43	W14x99	W14x48	W14x34
	7	W14x90	W14x53	W14x34	W14x82	W14x43	W14x30
	8	W14x74	W14x43	W14x43	W14x61	W14x43	W14x34
	9	W14x22	W14x90	W8x24	W14x22	W14x74	W8x21

CHAPTER 7:   Effect of Model Uncertainty on Multi-Limit State Performance Assessment

The performance-based earthquake engineering (PBEE) methodology (FEMA 2012) was established to provide owners and users with actionable information about the seismic risk to constructed facilities. The PBEE framework integrates seismic hazard characterization, structural response estimation and damage assessment to quantify earthquake impacts in terms of stakeholder-centered decision-variables (e.g. economic losses, number of fatalities, building recovery time). A key aspect of the methodology is the explicit inclusion and propagation of uncertainty throughout the different phases of assessment. In the structural response estimation stage, the considered uncertainties are generally placed in one of the following two categories: ground motion (or record-to-record) and modeling. The former is considered a type of aleatory uncertainty because it results from the inherent randomness in the frequency content of the ground motion records. Ground motion uncertainty is generally considered by utilizing a significant number of records in the structural response estimation. However, while there are still outstanding questions on issues such as the appropriate number of ground motions to be used in response history analyses (Baltzopoulos et al. 2019; Gehl et al. 2015), record-to-record uncertainty is routinely considered in PBEE assessments (e.g. Bradley, 2010).

Modeling uncertainty is a form of epistemic uncertainty because it arises from limitations in the data and knowledge that is used to construct the numerical model. According to Bradley (2013), there are four types of model uncertainty. Type 1 model uncertainties are attributed to the lack of complete knowledge about the measured value of physical quantities or "basic" parameters (e.g. the yield and modulus of elasticity of steel, the dead load on a structure). There is also uncertainty in the relationship between physical quantities and constitutive models (Type 2). Types 3 and 4 reflect the uncertainties in the suitability of the adopted constitutive

76

and system level modeling approaches, respectively. Level 1 and Level 2 uncertainties are generally considered by performing nonlinear response analyses on a suite of structural models with randomly sampled (using Monte Carlo simulation or Latin Hypercube sampling) basic and constitutive model parameters, respectively (e.g. Dolsek, 2009; Liel et al. 2009; Yin and Lee, 2010; Gokkaya et al. 2016). Evaluating the effects of Level 3 and Level 4 uncertainty is much less common because it requires nonlinear response analyses on a set of numerical model realizations that vary based on the adopted constitutive relationships and system and/or component idealization strategy (e.g. Aslani, 2005; Browning et al. 2000).

While record-to-record uncertainty was considered in theprior numerical analysis studies, none of them incorporated model uncertainty.

This chapter quantifies the effect of both record-to-record and Level 1 model uncertainty on the structural response and performance assessment of the CRSBF. Latin hypercube sampling is used to generate nonlinear structural model realizations for 3-, 6- and 9-story CRSBFs to account for the uncertainty in the basic model parameters. Multiple stripe analyses ($MSAs$) are performed on each structural model realization using sets of ground motions that are selected to match the target spectra associated with different hazard levels i.e. hazard-consistent ground motions. The probability distribution of different engineering demand parameters ($EDPs$) (e.g. peak residual and transient drift demands, strain in PT and shear deformation in fuse) and system-level performance limits (e.g. immediate occupancy, repairability, collapse prevention) are quantified incorporating both record-to-record and model uncertainties. After giving an overview of the adopted methodology, the design information for the considered building cases is presented. The nonlinear structural modeling and ground motion selection procedure is discussed followed by the analyses and performance assessment details and a discussion of the results.

7.1.   Overview of Methodology

The methodology for quantifying and comparing the effects of record-to-record and Type 1 model uncertainty (denoted as model uncertainty for the remainder of the chapter) on the seismic response and limit state performance of the CRSBF is illustrated in Figure 7.1. The basic structural parameters to be considered as random variables $(X_i; i = 1,2, \dots N_{RVs})$ are specified. Note that N_{RVs} is the total number of considered random variables. The dead load on the rocking frame (P_D), fuse yield strength (f_{yf}), and initial post-tensioning force (F_{PT}), which are known to affect the rocking response of the CRSBF, are taken as random variables. The yield strength of the beams, braces and columns (f_y), are also defined as random variables. In total, there are $N_{RVs} = 4$ random variables. The probability distributions (i.e., the type of distribution and the parameters that define the distribution) of the random variables is also determined.   Latin hypercube sampling (LHS) is used to sample N_m realizations of each random variable while making the appropriate assumptions about their correlation (or lack thereof). For each of the sampled $X_i's$, a nonlinear structural model is constructed using the Open System of Earthquake Engineering simulation (OpenSees) (McKenna, 1999).

$MSAs$ are performed on each structural model realization where record-to-record uncertainty is incorporated by using hazard-consistent sets of ground motions for the nonlinear response history analyses. In other words, a different record-set is selected at each intensity to match the target spectra corresponding to the associated hazard level. The probability distribution of $EDPs$ including the peak residual (RDR) and transient story drift ratio (SDR), PT strain (ε_{PT}) and shear deformation in the fuse (γ_{fuse}) corresponding to each stripe analysis is computed. System-level performance is also probabilistically assessed using the immediate occupancy (IO), repairability (RP) and collapse prevention (CP) limit states. Risk-based performance metrics are also quantified by obtaining site-specific hazard curves for the three

building cases and integrating them with the limit state fragility curves. A structural model that is based on the mean values of the random variables is constructed and analysed using $MSAs$ to isolate the effect of record-to-record uncertainty. Additionally, a disaggregation of model uncertainty is performed by generating sets of numerical models with one parameter randomized while mean values are used for the others.
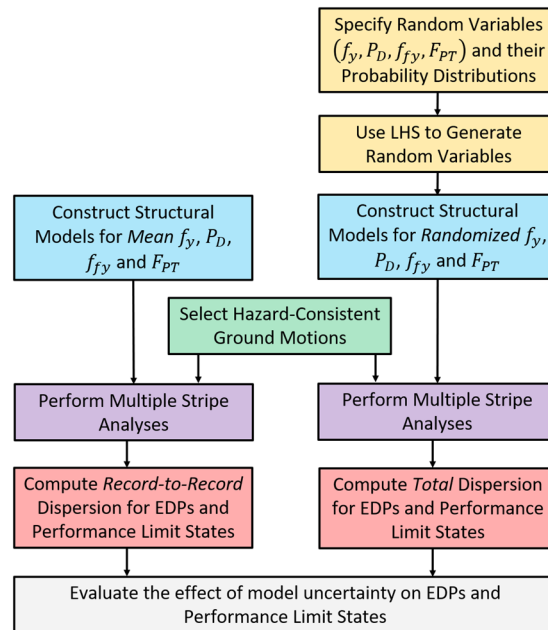
Figure 7.1. Overview of methodology used to quantify the record-to-record and modeling uncertainty in the CRSBF seismic response and performance

The uncertainty quantification methodology is applied to 3-, 6- and 9-story CRSBF building cases. The typical plan dimensions is shown in Figure 3.2 with two rocking frames in each direction of the 3-story building and the 6- and 9-story buildings have four CRSBFs in each direction. The X brace configuration shown in Figure 3.3(b) is considered.. The design of the building and structural modeling are described in Chapter 2 and Chapter 3 respectively. The member sizes of the buildings are listed in Appendix.

7.2.   Seismic Hazard Analysis and Ground Motion Selection

The Los Angeles site (33.58, -118.19) that is the basis of the seismic design parameters is also used in the hazard analysis and ground motion selection. The United States Geological Survey (USGS) unified hazard tool (https://earthquake.usgs.gov/hazards/interactive/) and OpenSHA "HazardCurveGUI" application (Field et al. 2003) is used to perform disaggregation at the following hazard levels: 10% in 50 years, 2% in 50 years, 2.5% in 100 years, 1.4% in 100 years, 2% in 200 years, and 1% in 200 years. A period of 0.75 seconds, which approximately corresponds to the mean ASCE 7-16 period (ASCE, 2016) of the three building cases, is used as the basis of the deaggregation. Using a single period enables the use of the same sets of ground motions for the three building cases (recall that a different set is selected at each hazard level) . The disaggregation information is used with the Campbell and Bozorgnia ground motion model (Campbell and Bozorgnia, 2014) to obtain uniform hazard target spectra and the associated dispersions at each hazard level. Six sets of ground motions (one for each hazard level) whose mean spectra provides a reasonable match with the target (Jayaram et al. 2011) are then selected. The period-dependent record-to-record variability is also preserved in the selected ground motions sets. Figure 7.2 shows the spectra for the six sets of ground motions (74 per set) including their mean respective targets and the 95% confidence interval. The USGS tool is also used to obtain the period-dependent hazard curves for the three buildings, which are shown in Figure 7.3.
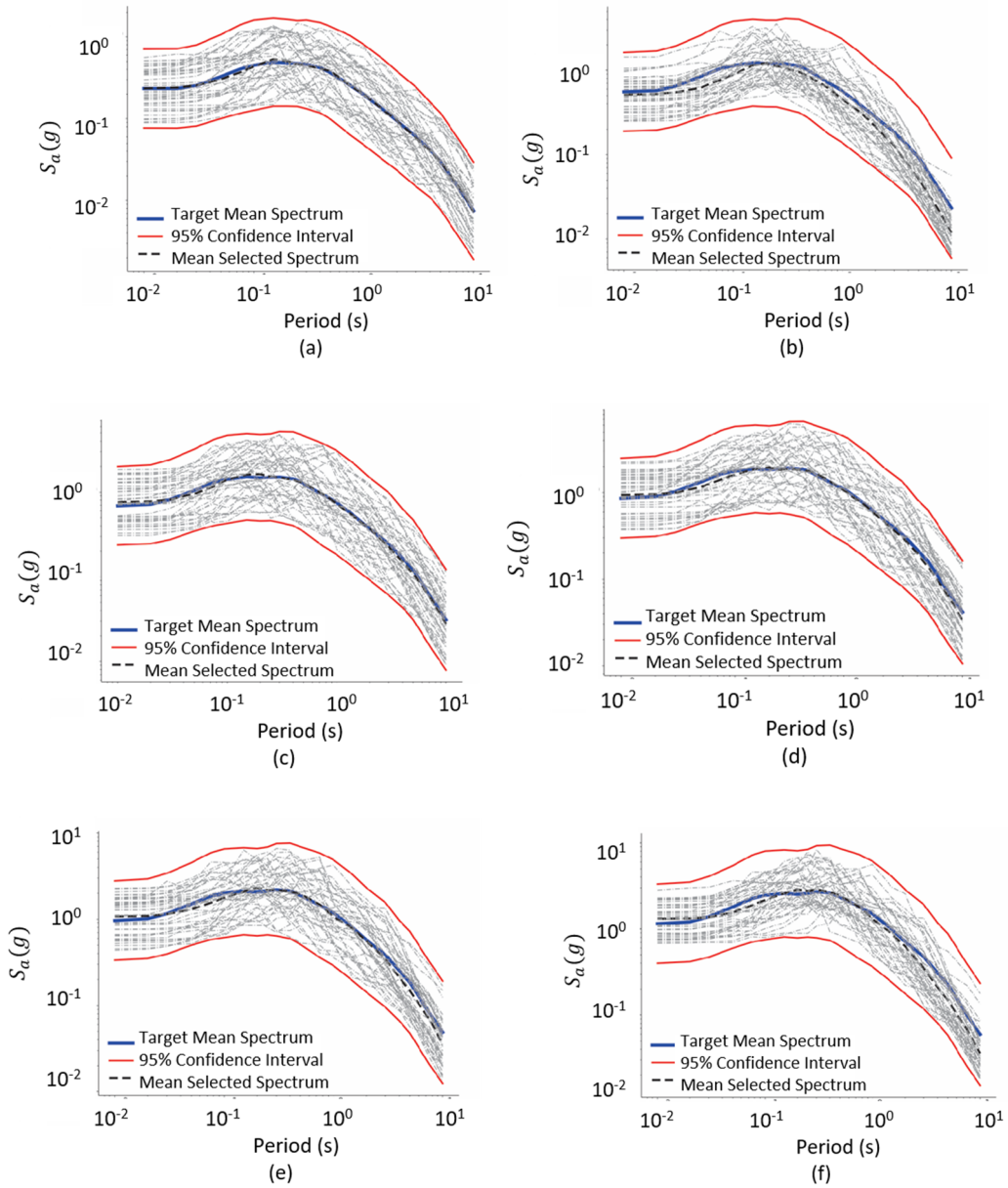
Figure 7.2. Spectra for selected suites of ground motions and their respective targets corresponding to the (a) 10% in 50 years, (b) 2% in 50 years (c) 2.5% in 100 years, (d) 1.4% in 100 years, (e) 2% in 200 years and (f) 1% in 200 years
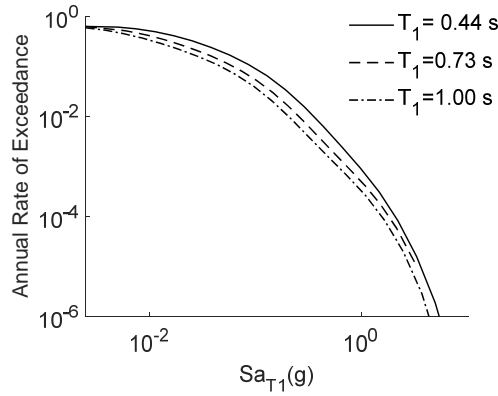
Figure 7.3. Period-dependent hazard curves corresponding to the three CRSBF building cases

7.3.   Uncertainty Characterization for Structural Model Parameters

Table 7.1 shows the four basic parameters that are considered as random variables in the nonlinear structural models. All are modeled using a lognormal distribution (Moradi et al. 2018) and their respective parameters (central tendency and dispersion) are also shown in Table 7.1. The P_D, f_{yf} and F_{PT} have been shown to influence the response and performance of the CRSBF (Moradi and Burton, 2018). These three parameters are normalized to the tributary seismic weight of the structure. The yield strength of the steel used in the beam, column and brace fiber elements (f_y), is also modeled as a random variable (Liu, 2003). Zero correlation is assumed across different random variables. However, perfect correlation is assumed when sampling multiple instances of a f_y for a single structural model realization. In other words, a single f_y value is sampled for each structural model realization and used in all beams, columns and braces.

Latin hypercube sampling (McKay et al. 1979) is used to generate realizations of structural models while considering the probability distributions of the aforementioned random variables. *LHS* generates realizations of the random variables based on nonoverlapping intervals with equal probability. The correlation structure among the random variables is maintained by

applying stochastic optimization with simulated annealing (Vorechovsky and Novak, 2003). A

total of 1000 *LHS* model realizations are generated at each hazard level.

Table 7.1 . Random variables and their respective distribution parameters

Building	Random Variable	Nominal	Bias	COV
All	f_y	344.7 N/mm^2	1.10	0.05
CRSBF-3S	P_D	$0.08W^1$	1.05	0.10
CRSBF-6S	P_D	$0.17W$	1.05	0.10
CRSBF-9S	P_D	$0.17W$	1.05	0.10
CRSBF-3S	f_{yf}	$0.18W$	1.16	0.06
CRSBF-6S	f_{yf}	$0.32W$	1.16	0.06
CRSBF-9S	f_{yf}	$0.29W$	1.16	0.06
CRSBF-3S	F_{PT}	$0.17W$	1.00	0.05
CRSBF-6S	F_{PT}	$0.32W$	1.00	0.05
CRSBF-9S	F_{PT}	$0.26W$	1.00	0.05

[1]Seismic weight tributary to CRSBF

7.4. Structural analysis and performance assessment considering record-to-record and model uncertainty

7.4.1. Record-to-record uncertainty

MSAs are first performed considering only record-to-record uncertainty. The models used

for this purpose are based on the mean values of the random variables (described as the mean

models in the remainder of the chapter). The empirical distribution of maximum story drift

ratios (SDR_{max}) corresponding to each hazard level is shown in Figure 7.4. The number of

datapoints at each hazard level corresponds to the number of ground motions (74). Recall that

MSA uses a different set of ground motions at each hazard level. The median story drift

corresponding to the 2% in 50 year or MCE hazard level is 1.4%, 1.3% and 1.3% for the 3-, 6-

and 9-story buildings, respectively, which are all below the 2.5% MCE level drift limit used in the CRSBF design. Figure 7.4 also shows that the record-to-record dispersion in SDR_{max} generally increases with the intensity, which is expected since the extent of the nonlinearity in the response increases with the hazard level. Because of the orders of magnitude differences in the SDR_{max}, the logarithmic standard deviation was found to be inappropriate for comparing the dispersion across hazard levels. As such, the 95% confidence interval $\left(CI_{SDR_{max}}\right)$ is used for this purpose, where the size of the interval is positively correlated with the dispersion. For the 3-story building, $CI_{SDR_{max}}$ ranges from 0.3% at the 10% in 50-year hazard level to 1.5% at the highest hazard level. In general, the $CI_{SDR_{max}}$ is found to be comparable across the different building cases. For example, the $CI_{SDR_{max}}$ corresponding to the lowest and highest hazard levels are 0.3% and 1.3% for the 9-story building, which is comparable to that of the 3-story building.
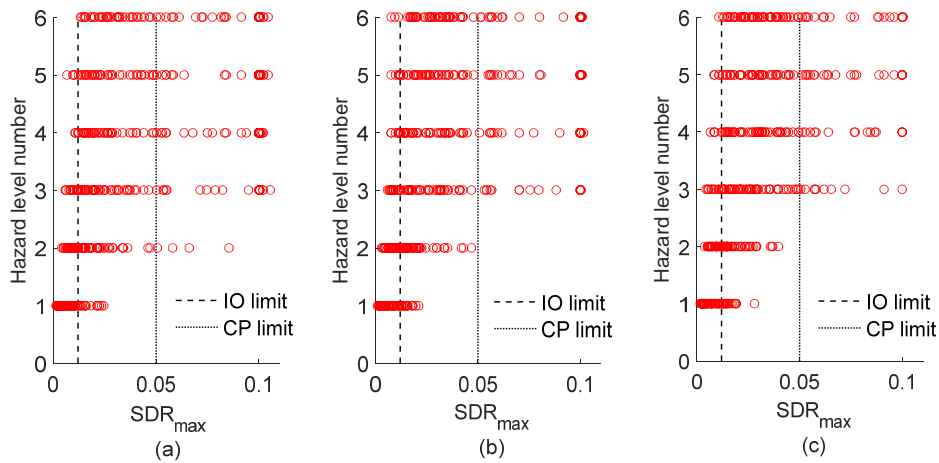
Figure 7.4. Empirical distribution of SDR_{max} from MSA considering only record-to-record uncertainty for (a) 3-story, (b) 6-story and (c) 9-story buildings

Figures 7.5, 7.6 and 7.7 show the empirical distribution of the maximum residual story drift (RDR_{max}), ε_{PT} and γ_{fuse}, respectively. At lower intensities, the residual story drift is negligible (on the order of less than 0.1% at the 2% in 50-year hazard level) as is the associated 95% confidence interval $\left(CI_{RDR_{max}}\right)$. However, at the higher return periods, $CI_{RDR_{max}}$ is

84

generally higher than $CI_{SDR_{max}}$ and the former decreases with the building height. For instance, the $CI_{RDR_{max}}$ at the 1% in 200-year hazard level is 2%, 1.8% and 1.5% for the 3-, 6- and 9-story buildings, respectively. A similar trend is observed for ε_{PT} and γ_{fuse} where the magnitude and dispersion (as reflected in the 95% confidence interval) generally decreases with the building height. This is explained by the greater contribution from higher modes (which reduces the uplift demand) and greater PT length (which reduces the ε_{PT}). The lower ε_{PT} and γ_{fuse} in the taller building is also consistent with the lower RDR_{max} values.
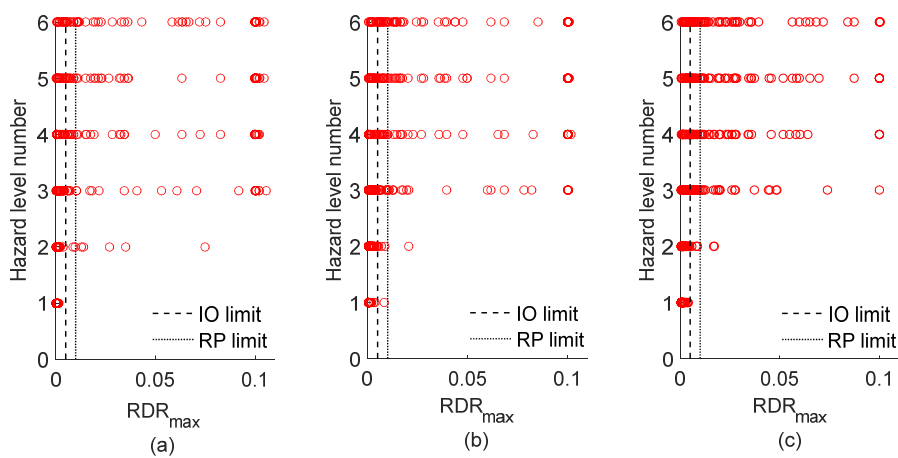
Figure 7.5. Empirical distribution of RDR_{max} from MSAs considering only record-to-record uncertainty for (a) 3-story, (b) 6-story and (c) 9-story buildings
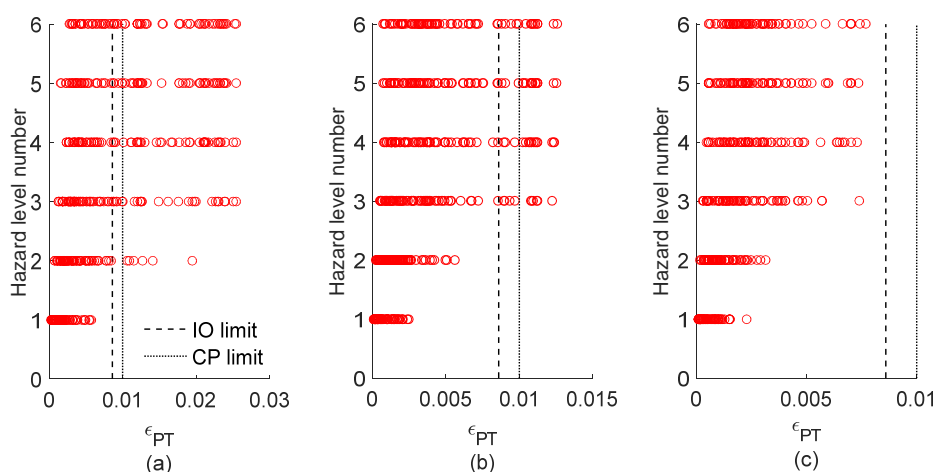
Figure 7.6. Empirical distribution of $\boldsymbol{\varepsilon_{PT}}$ from MSAs considering only record-to-record uncertainty for (a) 3-story, (b) 6-story and (c) 9-story buildings
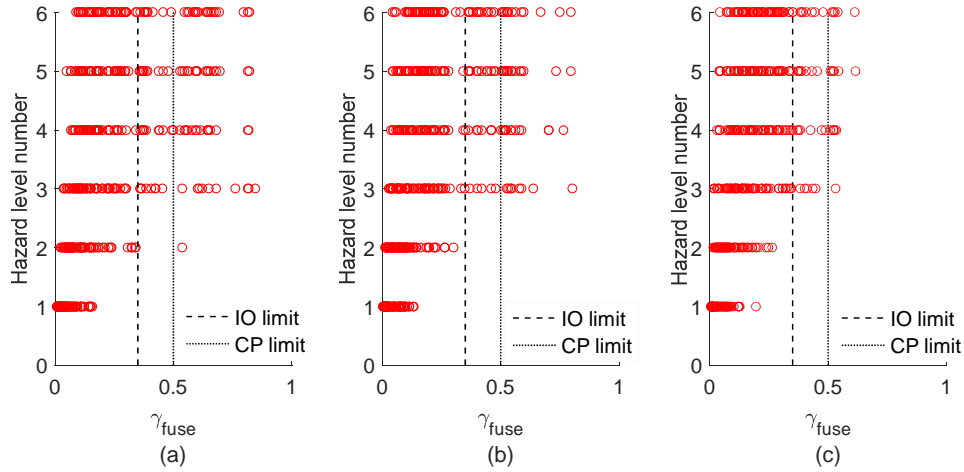
Figure 7.7. Empirical distribution of γ_{fuse} from $MSAs$ considering only record-to-record uncertainty for (a) 3-story, (b) 6-story and (c) 9-story buildings

As summarized in Table 7.2, the four $EDPs$ $(RDR_{max}, SDR_{max}, \varepsilon_{PT}$ and $\gamma_{fuse})$ are used as the basis of the considered limit states or building performance levels. The thresholds for the IO performance level (ASCE, 2017) include PT yielding $(\varepsilon_{PT} = 0.0086)$, the onset of strength degradation in the fuse $(\gamma_{fuse} = 0.35)$ and the residual drift limit for self-centering $(RDR_{max} = 0.005)$. Damage to the gravity framing and non-structural components is implicitly considered by including a drift limit of $SDR_{max} = 0.012$ in the IO performance level. The RP performance level is specified based on the integration of the probability of demolition conditioned on the RDR_{max} and the RDR_{max} conditioned in the intensity level curves (Ramirez and Miranda, 2012). The former is defined by a median value of 0.01 and log standard deviation of 0.3 (FEMA, 2012) and the latter is obtained from the MSA results. A story drift limit of $SDR_{max} = 0.05$ together with the PT strain at the onset of strength degradation $(\varepsilon_{PT} = 0.01)$ and the fuse shear deformation corresponding to complete fracture $(\gamma_{fuse} = 0.5)$, are the response thresholds for the CP performance level (ASCE, 2017).

Table 7.2. Performance levels and their associated EDP thresholds

Performance level	Response demand limit			
	SDR_{max}	RDR_{max}	ε_{PT}	δ_f
IO	0.012 [1]	0.005 [1]	0.0086 [2]	0.35 [2]
RP	NC[a]	0.01 [3]	NC	NC
CP	0.05 [4,5]	NC	0.01 [2]	0.5 [2]

[1] Wiebe and Christopolous (2015a)
[2] Ma et al. (2011)
[3] FEMA 2012
[4] Hwang and Lignos (2017)
[5] ASCE7-16
[a] NC: EDP not considered for the limit state.

Figure 7.8 shows the fragility curves corresponding to the three performance levels for the mean models. Figure 7.8(a) compares the IO fragility curves for the three building cases where Sa_{T1} is normalized by the MCE value (S_{MT}). The 3-, 6-, and 9-story building cases have comparable IO performance. A disaggregation of the EDP triggers showed that the IO performance level is primarily dominated by maximum story drift ratio, which, as discussed earlier, is comparable across the three building cases. For the RP performance level (Figure 7.8(b)), the median Sa_{T1}/S_{MT} for the 3- and 6-story buildings are comparable whereas the median value for the 9-story case is approximately 50% higher. Recall from Table 7.2 that RDR_{max} is the only EDP trigger that is considered for this performance level. Additionally, as discussed earlier, the residual drift demands generally decrease with building height because of the smaller PT strains and fuse shear deformation. Compared to the other two performance levels, there is more variation in the CP median Sa_{T1}/S_{MT} across the three building cases (Figure 7.8(c)). The 9-story building has a median Sa_{T1} that is more than three times the S_{MT}. Whereas the median Sa_{T1}/S_{MT} is 1.5 and 1.9 for the 3- and 6-story cases, respectively. This result is generally consistent with prior studies which showed that the collapse margin ratio of CRSBFs generally increase with building height (e.g. Steele and Weibe, 2016). Table 7.3 summarizes the median Sa_{T1}/S_{MT} and record-to-record dispersion (logarithmic standard deviation, β_{RTR}) for the three performance levels and building cases. Consistent with the

observations in Figures 5.4 through 5.7, the dispersion generally increases with the severity of

the performance level. It is also observed that β_{RTR} is generally higher for the taller buildings.
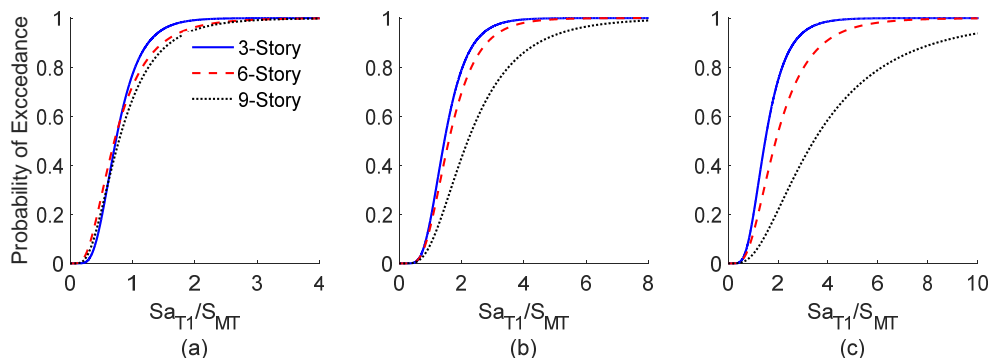
Figure 7.8. Fragility curves corresponding to the (a) IO, (b) RP and (c) CP performance
levels for the three building cases when only record-to-record uncertainty is considered

Table 7.3. Summary of median Sa_{T1}/S_{MT} and β_{RTR} for the three performance levels and
building cases

| Building | IO | | RP | | CP | |
ID	Sa_{T1}/S_{MT}	β_{RTR}	Sa_{T1}/S_{MT}	β_{RTR}	Sa_{T1}/S_{MT}	β_{RTR}
CRSBF-3S	0.73	0.42	1.45	0.4	1.49	0.45
CRSBF-6S	0.71	0.57	1.59	0.45	1.91	0.55
CRSBF-9S	0.78	0.56	2.21	0.55	3.44	0.69

7.4.2. Effect of model uncertainty on response demands and building performance levels

To consider both record-to-record and model uncertainty, each of the 1000 LHS realizations

is randomly matched with one of the 74 ground motions at each hazard level. To isolate the

effect of model uncertainty on the response demands, Figure 7.9 plots the ratio between the

total and record-to-record dispersion for the three $EDPs$ used to define the performance levels

$\left(\beta_{EDP_T}/\beta_{EDP_{RTR}}\right)$ versus the hazard level. Based on the results shown in Figure 7.9, modeling

uncertainty increases the dispersion of the 9-story building more than the 3- and 6- story cases

for most of the EDPs. This is especially true for RDR_{max} where modeling uncertainty increases

the log-standard deviation by as much as 20%. For the other $EDPs$ (SDR_{max}, ε_{PT}, and γ_{fuse}),

the log-standard deviation increased by approximately 8% in the 9-story building. There is no

consistent trend between the hazard level and the effect of model uncertainty on the log-standard deviation.
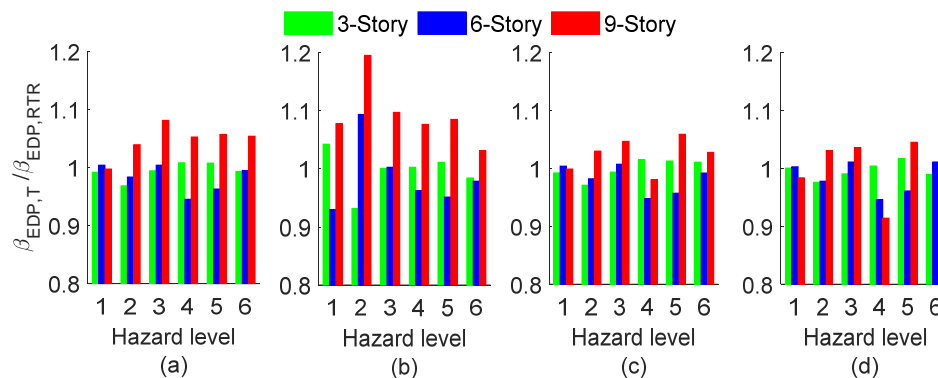
Figure 7.9. $\beta_{EDP_T}/\beta_{EDP_{RTR}}$ versus the hazard level for (a) SDR_{max}, (b) RDR_{max}, (c) ε_{PT} and (d) γ_{fuse}

Figure 7.10 shows the fragility curves for the three performance levels and building cases when both record-to-record and modeling uncertainty are considered, and the lognormal parameters are summarized in Table 7.4. The latter has been shown to affect both the median and dispersion of limit state intensities (e.g. Victorsson et al. 2011). To examine the effects on both, the ratio between the normalized (by S_{MT}) median limit state intensities with and without model uncertainty $\left(\theta_{LS_T}/\theta_{LS_{RTR}}\right)$ and the ratios associated with the dispersions $\left(\beta_{LS_T}/\beta_{LS_{RTR}}\right)$, are shown in Figure 7.11. The results show that, for the 9-strory building and RP limit state, model uncertainty increases both the median limit state intensity and the dispersion. It is also observed that the effect of model uncertainty on the dispersion is twice that of the median. More specifically, modeling uncertainty increases the log-standard deviation RP intensity by 33% compared to 17% for the median. For the CP limit state, modeling uncertainty increases the dispersion by 7% for the 9-story building whereas the effect on the 3- and 6-story cases is negligible.
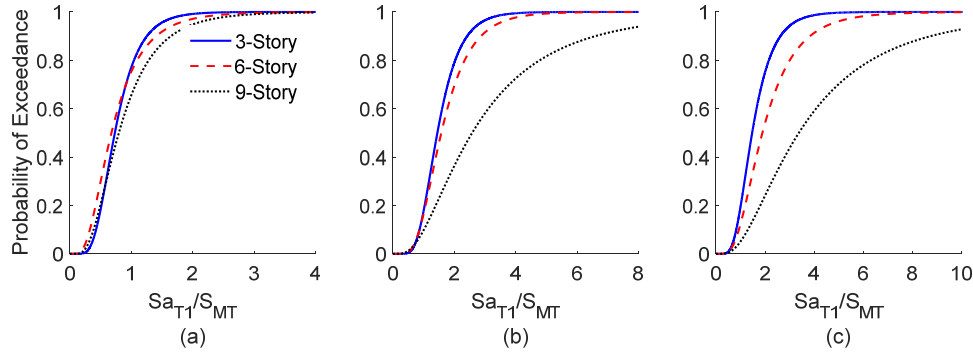
Figure 7.10. Fragility curves corresponding to the (a) IO, (b) RP and (c) CP performance levels for the three building cases when record-to-record and modeling uncertainties are considered

Table 7.4. Summary of median Sa_{T1}/S_{MT} and β_T for the three performance levels and building cases

| Building | IO | | RP | | CP | |
ID	Sa_{T1}/S_{MT}	β_T	Sa_{T1}/S_{MT}	β_T	Sa_{T1}/S_{MT}	β_T
CRSBF-3S	0.73	0.42	1.45	0.4	1.47	0.45
CRSBF-6S	0.68	0.57	1.58	0.47	1.89	0.55
CRSBF-9S	0.8	0.56	2.58	0.73	3.37	0.74
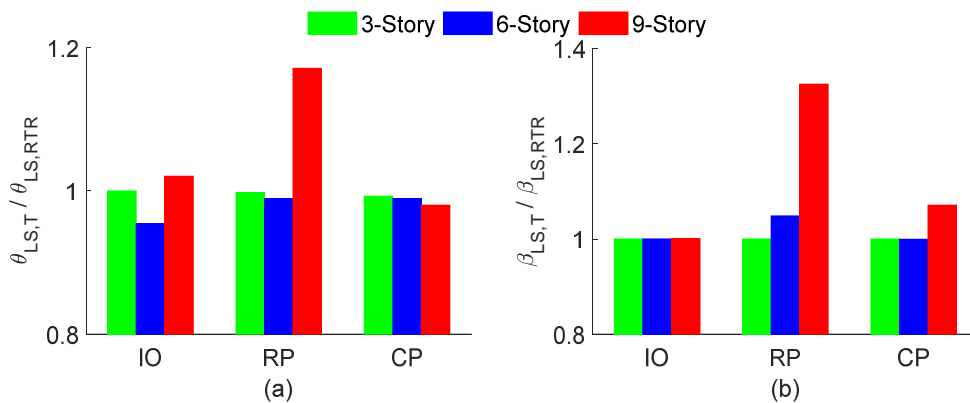
Figure 7.11. Bar charts showing (a) $\theta_{LS_T}/\theta_{LS_{RTR}}$ and (b) $\beta_{LS_T}/\beta_{LS_{RTR}}$ for the three limit states and building cases

To support a risk-based assessment of the effect of modeling uncertainty on the CRSBF performance, site-specific hazard curves based on Sa_{T1} are obtained. The hazard curves for the same Los Angeles site used as the basis of the ground motion selection corresponding to the first-mode periods of the three building cases are shown in Figure 7.3. The mean annual

frequency of limit state exceedance (λ_{LS}) is computed by integrating the respective fragility function with the site-specific hazard curve. Then, the probability of limit state exceedance over a 50-year service life $(P_{LS,50yr})$ is computed using λ_{LS} and assuming a Poisson distribution. Figure 7.12 shows the ratio between the λ_{LS} with and without the consideration of model uncertainty $(P_{LS,50yr_T}/P_{LS,50yr_{RTR}})$. Consistent with earlier results, the effect of modeling uncertainty is highest for the 9-story building. However, a key departure from the earlier results is that, unlike the limit state median and dispersion, the effect of modeling uncertainty on the service life CP performance is comparable RP where the $P_{LS,50yr_T}/$ $P_{LS,50yr_{RTR}}$ values are 1.27 and 1.29, respectively.
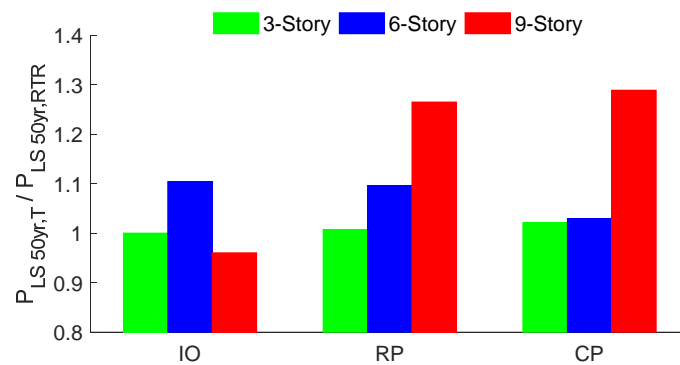
Figure 7.12. Bar chart showing $P_{LS,50yr_T}/P_{LS,50yr_{RTR}}$ for the three limit states and building cases

7.4.3. Disaggregation of model uncertainty

Disaggregation of the dispersion is an effective way to identify which random variables contribute the most to the model uncertainty. This is achieved by repeating the $MSAs$ using the LHS model realizations considering each random variable individually. In other words, the LHS model realizations are generated by randomizing individual variables while using the mean value for others. The disaggregation is only performed for the 9-story building where model uncertainty is shown to have the most significant effect on the limit state performance. Figure 7.13 compares the $P_{LS,50yr_T}/P_{LS,50yr_{RTR}}$ values when the random variables

$(P_D, f_{yf}, F_{PT}$ and $f_y)$ are considered individually. For the IO limit state, the uncertainty in the fuse yield strength is shown to have the greatest effect on service life performance. The uncertainty associated with the dead load on the rocking frame has the highest effect on the RP service life performance. This can be explained by examining the self-centering ratio equation $\left(SC = \frac{F_{PT} + 2P_D}{f_{yf}} \right)$ that is used in the CRSBF design. A greater dead load means that there is less reliance on the fuse for overturning moment strength, which leads to lower residual drifts. For the service life CP performance, the uncertainty in the yield strength of the beams, columns and braces has the greatest effect. This is because yielding of these elements only becomes a concern at higher demands and more severe limit states.
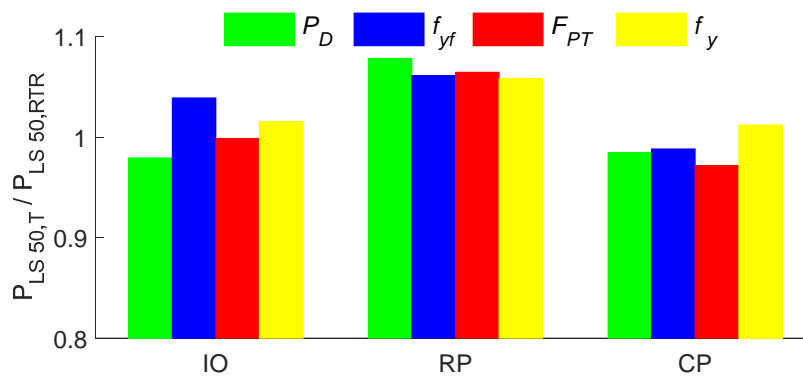
Figure 7.13. Bar chart showing $P_{LS,50yr_T}/P_{LS,50yr_{RTR}}$ for the 9-story building when the random variables are considered individually.

7.5.   Summary and Conclusion

In this study, modeling uncertainty is propagated and quantified to investigate its effect on the seismic response demands and performance of controlled rocking steel braced frames (CRSBFs). Those design parameters that have been shown to have a strong influence on the seismic performance of CRSBFs are modeled as random variables, including the yield strength of the braced frame members $\left(f_y \right)$, the dead load (P_D) on the rocking frame, the initial post-tensioning (PT) force $\left(F_{PT} \right)$ and the fuse yield strength $\left(f_{yf} \right)$. The uncertainty in these four parameters is propagated by generating randomized realizations using Latin Hypercube

Sampling (LHS), which are then used to construct nonlinear structural models for 3-, 6-, and 9-story building cases. Multiple stripe analyses ($MSAs$) are performed for each model realization using six sets of hazard-consistent ground motions. The impact of modeling uncertainty is evaluated for the immediate occupancy (IO), repairability (RP) and collapse prevention (CP) performance levels as well as the CRSBF structural response demands. The triggers for the limit states are based on the maximum transient (SDR_{max}) and residual story drift ratio (RDR_{max}), the PT strain (ε_{PT}), and the fuse shear deformation (γ_{fuse}).

Record-to-record dispersion was isolated by performing $MSAs$ on models constructed with the mean values of the considered random variables. Using the 95% confidence interval (CI) as the measure of dispersion, the record-to-record dispersion for all four engineering demand parameters ($EDPs$) increased with the hazard level. However, while the magnitude and record-to-record dispersion of SDR_{max} was found to be comparable across the different building cases, for RDR_{max}, ε_{PT}, and γ_{fuse}, there was as overall decrease in the demand level and CI as the building height increased. The effect of model uncertainty on the SDR_{max} dispersion in the 3- and 6-story buildings was found to be negligible. For the 9-story building, the log-standard deviation of SDR_{max} increased by up to 8% when modeling uncertainty was included. Among the four $EDPs$, modeling uncertainty had the largest impact on the RDR_{max} dispersion, increasing the log-standard deviation by a maximum of 20%. For ε_{PT}, and γ_{fuse}, modeling uncertainty increases the log-standard deviation by as much as 7%.

For the 3- and 6-story buildings, the median and dispersion (log-standard deviation) of the fragility curves for all three limit states were minimally affected by model uncertainty. Whereas for the 9-story building, modeling uncertainty increased the median and dispersion of the RP fragility curve by 17% and 33%, respectively. To evaluate the effect of model uncertainty on the service life performance, the limit states fragility curves were integrated with the hazard

curves corresponding to a Los Angeles site and the periods of the three building cases. The probability of limit state exceedance in 50 years for IO and RP increased by approximately 10% for the 6-story building when model uncertainty was considered. The impact on the RP and CP for the 9-story building was more significant with the 50-year probability of exceedance being increased by approximately 30% for these two limit states. A disaggregation of the effect model uncertainty by random variable for the 9-story building showed that the IO, RP and CP performance levels are most impacted by the fuse yield strength, dead load on the rocking frame and yield strength in the braced frame elements (beams, columns and braces), respectively.

Appendix

Table A.1. List of beams, braces, and columns sections

Model	Story	Column sections	Brace sections	Beam sections
CRSBF-3S	1	W14x99	W14x109	W14x43
	2	W14x99	W14x61	W14x43
	3	W14x99	W14x99	W14x43
CRSBF-6S	1	W14x120	W14x99	W14x30
	2	W14x120	W14x61	W14x34
	3	W14x120	W14x43	W14x43
	4	W14x90	W14x53	W14x30
	5	W14x90	W14x53	W14x34
	6	W14x90	W14x82	W14x30
CRSBF-9S	1	W14x193	W14x132	W14x30
	2	W14x193	W14x68	W14x30
	3	W14x193	W14x68	W14x30
	4	W14x193	W14x61	W14x30
	5	W14x193	W14x61	W14x30
	6	W14x193	W14x61	W14x30
	7	W14x109	W14x61	W14x30
	8	W14x109	W14x61	W14x43
	9	W14x109	W14x90	W14x30

CHAPTER 8: Quantifying Earthquake-Induced Social and Environmental Impacts

This chapter presents an evaluation of seismic performance of CRBFs in terms of earthquake-induced economic loss and environmental impact (energy consumption and greenhouse gas emission) over the service life of the buildings. The optimal design parameters that will minimize the life cycle impacts (upfront plus service life) is also determined. Surrogate models are used to establish a relationship between the structural design parameters and earthquake impacts. The engineering demand parameters (EDPS) from nonlinear response history analyses (NRHAs) are used as inputs into the earthquake impact assessments.

Very little research has been performed on quantifying the life cycle earthquake impacts of CRSBF buildings. Dyanati et al. (2017) compared the annualized economic losses of concentric braced frames (CBFs) and the CRSBF system. Losses due to drift-sensitive component damage was found to be lower in CRSBF compared to CBF. The opposite was found to be true for acceleration-sensitive component damage. The overall losses for a 6-story building case was smaller in the CRSBF compared to the CBF, however, the opposite was found to be true for a 10-story building.

8.1.   Performance-Based Assessment and Design Optimization Overview

Figure 8.1 shows an overview of the seismic performance assessment and design optimization methodology. Central to the overall framework is the development of surrogate models that can reasonably approximate the combined upfront (initial construction of CRSBF only) and earthquake-induced impacts over a predefined structural design domain (structural parameter ranges and combinations). The goal of the design optimization is to minimize the

earthquake-induced impacts associated with both initial construction (of only the CRSBF) and the building service life.
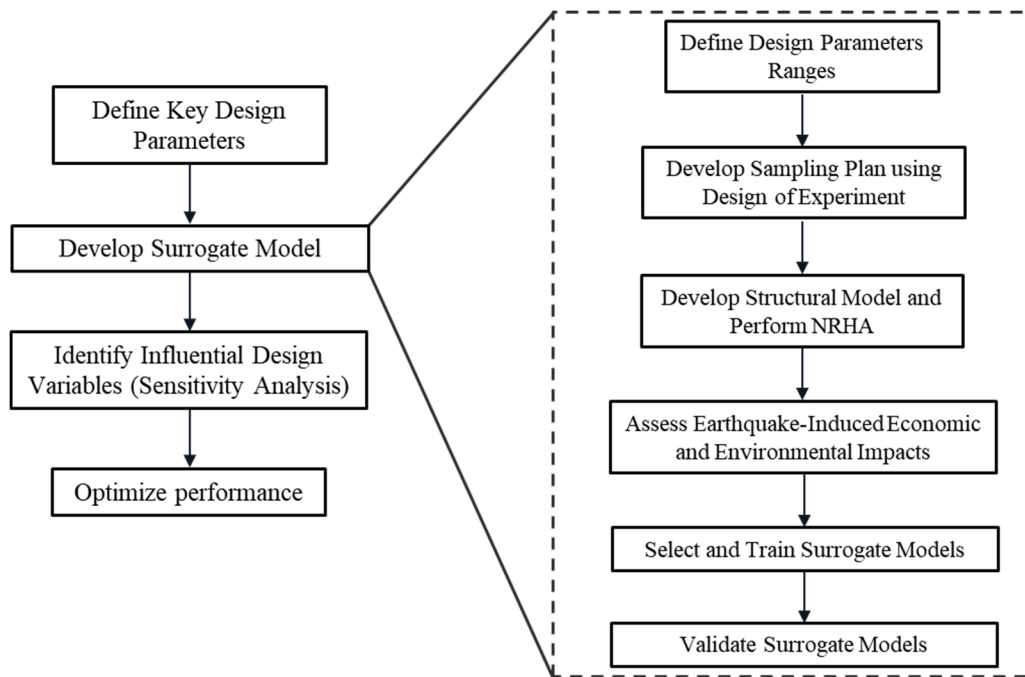
Figure 8.1. Overview of performance-based assessment and design optimization methodology

The first step is to define the key input parameters. The design variables specified in Chapter 5 (Table 5.1) are also used in this chapter. They include the dead load on each column of CRSBF (P_D), initial PT force (F_{PT}), fuse yield strength (F_{yf}), frame aspect ratio (bay width to height ratio of CRSBF) (B/H), and fuse strain hardening ratio (α). The three first parameters (P_D, F_{PT}, and F_{yf}) are normalized by seismic weight of the buildings to make them unitless.

As it was noted in Chapter 5, the sampling plan development is used to determine the design cases. Each design case is associated with a combination of the discrete factor levels of the design parameters (Table 5.2).

Once the design cases are defined, nonlinear response history analyses (NRHAs) are performed and then statistical link between the identified input parameter (design key parameters) and seismic performance of the CRBFs is developed by surrogate models.

Earthquake-induced impacts (economic losses and environmental effects) are defined based on the cost of repairing earthquake damage to structural and non-structural components. The FEMA P58 methodology (FEMA 2012) is used to assess the earthquake-induced impacts. Life cycle assessment (LCA) method is used to assess environmental impacts of the buildings using Athena LCA tool (Weber et al. 2009).

Note that the initial cost of only the structure is added to the earthquake-damage occurring during the building's service life. The non-structural building components are excluded from the optimization because the assumption is that they are constant across all design cases. This assumption also enables an isolation of the effect of the CRSBF design and behavior of the building service life performance.

Selecting the type of the surrogate model is the next step, which involves choosing the type of model that represents the relationship between the design variables and the performance of the structure. The surrogate models constructed using the training data and tested using designs that are unseen by the training data. The latter is used to assess the predictive capabilities of the surrogate model. Once the surrogate model is finalized, the performance-based optimization is implemented.

8.2.   Ground Motions and Nonlinear Response History Analyses

The sampling points are based on 43 design cases for each of the 3-, 6-, and 9-story buildings i.e. a total of 129 cases (Table 5.2). The baseline building case for the 3-, 6-, 9- story CRSBF buildings are associated with the center levels of the input variables (Table 5.1). The building cases are numbered 1 through 129 and the baseline building cases numbers 43, 86, and 129 for the 3-, 6-, and 9-story buildings, respectively. The typical plan dimension is shown in Figure 3.2 with two rocking frames in each direction, and the X-braced frame configuration

97

shown in Figure 3.3b is considered. The design of the building and structural modeling are described in Chapter 2 and Chapter 3, respectively.

The ground motions used for structural analyses are the far-field ground motion records specified in the FEMA P695 guidelines (FEMA 2009), which were also used in Chapter 6 (Figure 6.2). The spectral acceleration at the effective period of the CRSBF (T_e) is used as the ground motion intensity measure. The effective period of the CRSBF (T_e) is computed using the procedure outlines in Section 5.4. Ground motions are scaled individually such that their spectral acceleration at T_e (Sa_{Te}) matches the MCE-level elastic design spectrum ($Sa_{Te,MCE}$). Incremental dynamic analyses are performed for each ground motion using increments corresponding to 20% $Sa_{Te,MCE}$ until collapse occurs. An additional analysis case is performed at 5% $Sa_{Te,MCE}$ to consider the responses, damage, and losses at low hazard levels in the numerical integration. The maximum drift ratio in each story, the peak acceleration corresponding to each floor level and residual drift demand in each story, are obtained from each analysis. The analysis results are also used to generate the collapse fragility curve parameters (median and log standard deviation) assuming lognormal distribution using the maximum likelihood method (Baker, 2015). The collapse intensity is defined when the slope of the IDA curve is very small or the intensity that caused story drift ratio of the structure exceeds 10%. The building is assumed to be irreparable when the residual story drift ratio exceeds 1%. The median collapse intensities are also multiplied by the spectral shape factor (*SSF*) based on the FEMA P695 simple method. Moreover, uncertainties associated to the robustness of the design requirements, the accuracy of the test data, and the accuracy of the numerical model are added to the record-to-record variability of collapse. According to FEMA P695, these uncertainties are assigned to 0.1, 0.2, 0.35, and 0.5 for "superior", "good", "fair", and "poor" ranks, respectively. In this study, the uncertainties associated with the "good" rating

are considered for the robustness of the design requirements, the accuracy of the test data, and the accuracy of the numerical model uncertainties.

8.3.   Service-Life Earthquake-Impact Assessment

For each of the 129 sampling points or input parameter combinations, the earthquake induced-impacts (economic losses or environmental effect) corresponding to each ground motion intensity level is obtained by applying the FEMA P58 methodology. Incremental Dynamic Analysis (IDA) to collapse using the 44 FEMA P695 (FEMA, 2009) ground motions is performed for each design case and the associated engineering demand parameters (EDPs) including the maximum story drift ratio, peak floor acceleration, and residual drift ratio are recorded. The EDP exceedance probabilities ($P(EDP_i > edp \mid IM)$) are then combined with component-level damage fragility curves $P(DM=dm \mid EDP_i)$ and component-level consequence (economic or environmental impact) functions $E[EI_i \mid DM]$ to generate earthquake impacts $E[EI_i \mid IM]$ for each components:

$$E[EI_i | IM] = \int_0^\infty E[EI_i | EDP] |dP(EDP > edp | IM)| \qquad (8.1)$$

$$E[EI_i | EDP] = \sum_{k_i=1}^{m_i} E[EI_i | DM_{k_i}] P[DM_{k_i} | EDP] \qquad (8.2)$$

where k_i is the number of the damage states, DM_{ki} is the damage state k_i, and m_i is number of the considered components. The economic loss or environmental impact of each design case or sampling point is taken as the sum of the impacts from the structural and non-structural components:

$$E[EI_T | NC \cap R, IM] = \sum_{i=1}^N E[EI_i | IM] \qquad (8.3)$$

$E[EI_T|NC \cap R, IM]$ is the earthquake impact conditioned on the damaged but non-collapsed structure (repair(R)). Recall that the structural response demands used in Equation 8.1 comes from the ground motions that do not cause collapse.

Note that in order to compute the total economic loss or environmental impact, collapse and demolition need to be considered. Total probability theorem is used to incorporate the probability of collapse and demolition conditioned on ground motion intensity:

$$E[EI_T|IM] = E[EI_T|NC \cap R, IM]P(NC \cap R|IM) + \mathbf{K} \\ E[EI_T|NC \cap D, IM]P(NC \cap D|IM) + E[EI_T|C, IM]P(C|IM)$$

(8.4)

Where R, D, and C refer to repaired, demolition, and collapse limit states of the structure. $E[EI_T|NC \cap D, IM]$ is the total expected earthquake-induced impacts of the non-collapsed structure when the residual story drift ratio exceeds 1% (demolition), and $E[EI_T|C, IM]$ is the expected earthquake-induced impacts of the collapsed structure. Note that $E[EI_T|NC \cap D, IM]$ and $E[EI_T|C, IM]$ are taken as the cost and environmental impact (greenhouse gas emissions (CO_2) or energy consumption) associated with the initial construction of the building.

8.3.1. Economic loss assessment

The Seismic Performance Prediction Program (SP3) (https://www.hbrisk.com) is used to perform the intensity-based loss assessment. Table 8.1 summarizes the damageable structural and non-structural components for each story that are considered in the economic loss assessment.

Table 8.1. Damageable components and quantities used in the economic loss assessment

Building component	Unit	EDP	Quantity per story
CRSBF	Each	SDR[a]	4
Gravity connections	Each	SDR	104
Curtain walls	30 ft2	SDR	180
Partition walls	100 ft	SDR	10
Wall partition finishes	100 ft	SDR	0.8
Suspended ceiling	250 ft2	PFA[b]	40
Independent pendant lighting	Each	PFA	30
Traction elevator	Each	PFA	2, 3, 4[c]
Potable water piping	1000 ft	PFA	1.7
Potable water pipe bracing	1000 ft	PFA	1.7
HVAC ducting	1000 ft	PFA	1
Fire sprinkler water piping	1000 ft	PFA	2
Fire sprinkler drop	x 100	PFA	0.9

[a]*SDR* Story drift ratio

[b]*PFA* Peak floor acceleration

[c]Entire building, 2, 3, and 4 for 3-, 6-, and 9-story buildings respectively.

Note that, for the elements of the braced frame (beams, columns, and braces), the drift demand due to rigid body rotation are excluded from the damage assessment. All economic losses are normalized by the building's replacement cost excluding the demolition cost, which includes the removal of debris, is taken as 25% of the initial construction cost (FEMA 2012). The cost of the building is taken to be 252 US dollars, 257 US dollars, and 257 US dollars for 3-story, 6-story, 9- story buildings, respectively (Seismic Performance Prediction Program (SP3) (https://www.hbrisk.com)).

More robust CRSBF designs will ultimately lead to reduced service-life earthquake impacts, however, the upfront environmental and economic costs will be greater. This tradeoff between enhanced robustness and increased initial impacts is considered by quantifying an environmental and economic "cost premium" that will be added to the service-life earthquake impacts. For each sampling point, this cost premium is defined as the initial-construction-impact (environmental and economic) of the controlled rocking braced frame members

normalized by that of the entire building, C_{CRBF}. Figure 8.2(a), (b), and (c) show the C_{CRBF} for the 43 design cases of the 3-story, 6-story, 9- story buildings respectively.
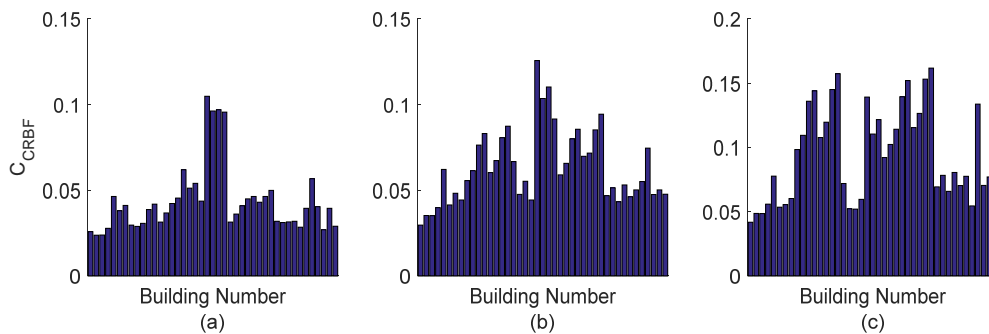
Figure 8.2. Distribution of normalized (by building replacement cost) upfront cost of the controlled rocking braced frame (C_{CRBF}) for (a) 3-story (b) 6-story (c) 9-story design cases

The upfront cost of the controlled rocking braced frames ranges from 2.4% to 10.5% , 3.0% to 12.6%, and 4.2% to 16.2% for 3-story, 6-story, and 9-story buildings respectively. It's not surprising that building (or sampling point) 1, which corresponds to the lower-level value (Table 5.2) for all five input parameters, has the lowest C_{CRBF}. In contrast, the highest C_{CRBF} corresponds to building 21, which has lower level values for all the input parameters except the fuse yield strength (F_{yf}) and strain hardening ratio (α). According to Equation 3.12,, the number of PT needs to be increased at higher values of the ultimate fuse force (F_{uf}) to account for the inelastic strain hardening of the energy dissipating fuse. The effect of the ultimate force on SC* is more appreciable when the dead load and PT force, which provide overturning resistance, are small. Increasing the number of PT strands increases the ultimate force on the frame and leads to an increase in the braced frame member sizes. Increasing the bay width of the CRSBF (while the other variables are constant) leads to an increase in the number of PT strands (Equation 3.8) which in turn leads to a higher PT ultimate force and larger member sizes. However, increasing the length of the beams will increase the length and number of the fuse links (Equation 3.10) which will decrease the fuse stiffness (Equation 3.11) and ultimate

fuse strength. Therefore, there is no specific correlation between the bay width of the rocking frame and C_{CRBF}.

Site-specific seismic hazard curves based on the equivalent SDOF period (Chapter 5) are shown in Figure 8.3 for the baseline 3-story, 6-story, and 9-story design cases, which correspond to the "center-level" parameter values ((i.e. $P_D/W = 0.225$, $F_{pt}/W = 0.225$, $F_{yf}/W = 0.4$, $B/H = 0.35$, and $\alpha = 0.04$).
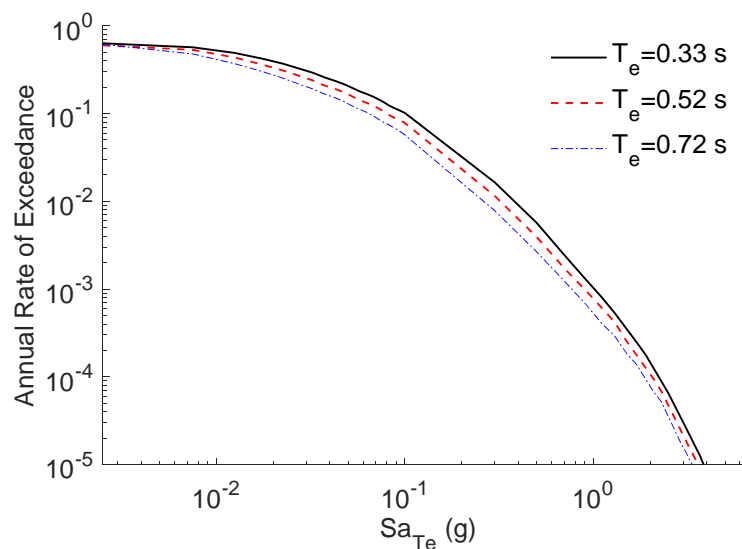
Figure 8.3. Hazard curves corresponding to the "center level" sampling points for the 3-story, 6-story, and 9-story buildings

The normalized expected losses (by the replacement cost) conditioned on the ground motion intensity for the center-level sampling point (Table 5.1) is shown in Figure 8.4 for the 3-story, 6-story, and 9-story buildings. The initial cost of construction is 7,257,600 US dollars, 14,803,200 US dollars, and 22,204,800 US dollars for 3-story, 6-story, and 9-story buildings, respectively.

The economic losses conditioned on the intensity level, $E(L|Sa_{Te})$ are disaggregated based on contributions from collapse, demolition, structural damage, drift-sensitive non-structural damage (DS-NS) and acceleration-sensitive non-structural damage (AS-NS) which are listed

in Table 8.1. Figure 8.4 shows that, for the baseline designs subjected to lower intensity levels (less than Sa_{DBE}, which is 1g, 1g, and 0.8g for the 3-story, 6-story, and 9-story, respectively) where annual rates of hazard exceedance are highest, the DS-NS components (mostly by curtain walls) contribute significantly to the losses in the 3-story building. Whereas, in tall buildings, the AS-NS components (mostly by elevator) have higher contribution at lower intensities.

The normalized total expected loss for the baseline buildings at Sa_{MCE} (1.5(g), 1.5(g), and 1.25(g) for the 3-story, 6-story, and 9-story, respectively) is 0.34, 0.20, and 0.17 for 3-story, 6-story, and 9-story respectively, showing an inverse correlation with the building height. The disaggregated losses (i.e. collapse, demolition, structural, DS-NS, and AS-NS) are shown in Figure 8.5 for all three baseline cases. The collapse and demolition losses for the baseline 6-story is less than the 3-story and 9-story building cases across all intensity levels. However, the structural, DS-NS, and AS-NS are larger at higher intensity levels. Except for collapse and demolition, the disaggregated losses in the 6-story baseline case is larger than the 3-story and 9-story models at the MCE level. Note that rigid body rotation is most prevalent in the 3-story building, which results in higher story drifts. Therefore, although Figure 8.4 shows that the economic losses in the 3-story building are higher than the 9-story at low intensities, this is not the case at higher intensity levels (See Figure 8.5).
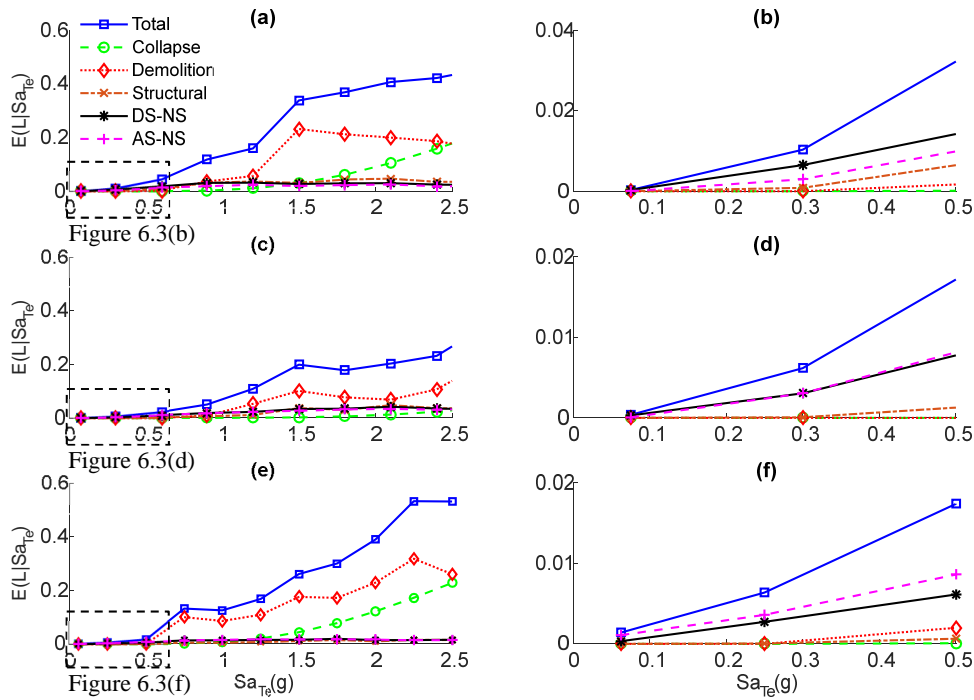
Figure 8.4. Normalized (by replacement values) and disaggregated economic losses of (a,b) 3-story (c,d), 6-story, and (e,f) 9-story conditioned on the ground motion intensity for the "center-level" sampling point
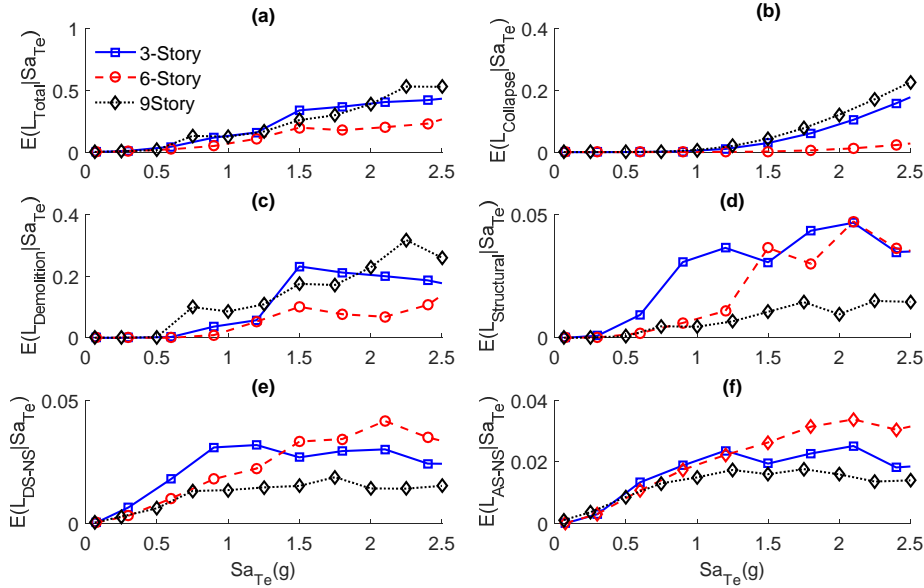
Figure 8.5. Comparison of (a) total expected economic loss due to (b) collapse, (c) demolition, (d) structural, (e) DS-NS, and (f) AS-NS of 3-story, 6-story, and 9-story buildings conditioned on the ground motion intensity for the "center-level" sampling point

The mean annual frequency of earthquake-induced impacts, $E[EI_T]_{1yr}$, is computed using the expected earthquake impact conditioned on ground motion intensity and site-specific hazard curve:

$$E[EI_T]_{1yr} = \int_0^\infty E(EI_T|IM = im).\,d\lambda(IM) = \int_0^\infty E(L|IM).\left|\frac{d\lambda(IM)}{d(IM)}\right| d(IM) \tag{8.5}$$

Intensity level-based disaggregation of the economic losses for the baseline design cases of the 3-story, 6-story, and 9-story buildings (center-level of sampling points) is shown in Figure 8.6. The mean annual economic losses is computed as the area under the disaggregation curve.
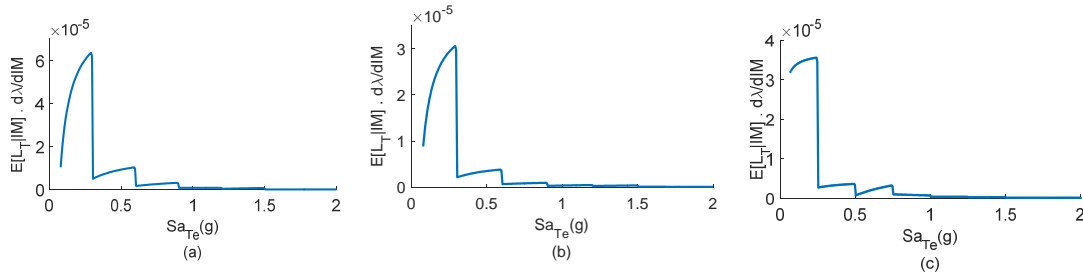
Figure 8.6. Disaggregation of economic loss assessment for the (a) 3-story (b) 6-story (c) 9-story baseline design cases

The earthquake-induced building impacts over an assumed 50-year service life is computed using an annual discount rate of 5%, a value that is within the range commonly used in engineering decision making (2.5–6%) (Lee and Ellingwood 2015).

$$E(EI_{50yr}) = \sum_{yr=1}^{50} E[EI_T]_{1yr}\,(1 + 0.05)^{-yr} \tag{8.6}$$

The 50-year service life, $E(L_{50yr})$ economic losses (normalized by the initial cost of the building) for the 129 buildings designed based on the five different input parameters (P_D/W, F_{pt}/W, F_{yf}/W, B/H, and α) are computed using Equation 8.6 while considering the aforementioned discount rate. The normalized disaggregated service-life impacts for all

106

sampling points are presented in the form of bar charts in Figure 8.7. As noted earlier, 43 sampling points (or design parameter combinations) are used for each building height.

Figure 8.7(a) shows that the earthquake-induced economic losses for the 3-story building cases range between 2.0% to 6.6% of the building replacement cost. For the 6-story cases (Figure 8.7(b)), that range is between 0.8% to 3.5% . In other words, for the adopted sampling plan, the selected input parameters can change the service-life economic losses by a factor of up to 3.3 and 4.4 for the 3-story and 6-story buildings, respectively, which demonstrates an increase in the variability of the economic loss within the sampling space as the height of the structure increases.
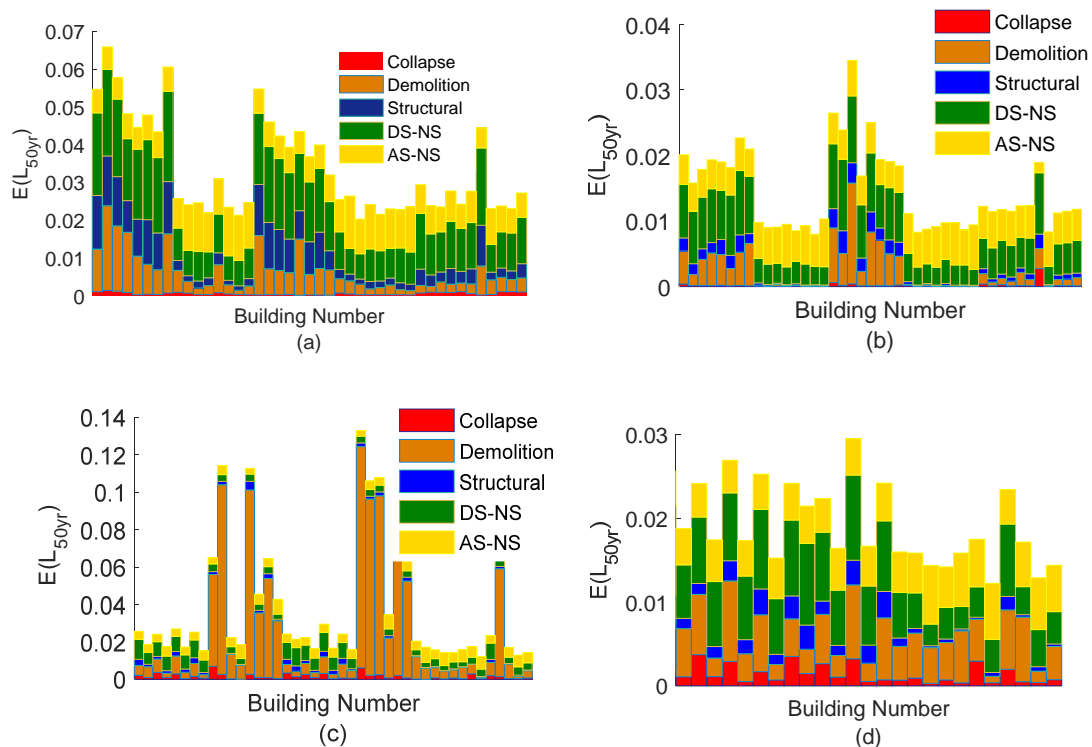
Figure 8.7. Normalized (by replacement values) and disaggregated service-life impacts for all sampling points for the (a) 3-story, (b) 6-story, and (c,d) 9-story design cases

There is also significant variation in the distribution of losses across the different categories. Collapse and demolition have a smaller effect than the other categories over all sampling points of the 3-story and 6-story cases. However, Figure 8.7(c) shows that for some 9-story models, demolition contributes significantly to the total loss. The design cases with

aspect ratio of 0.5 have a span of approximately 60ft in the 9-story buildings, which is impractical and leads to large residual drifts. Figure 8.7(d) shows the 9-story designs after eliminating the 17 designs with aspect ratio of 0.5. Figure 8.7(a), (b), and (d) show that the economic loss is dominated by nonstructural components and the effect of DS-NS damage is more than AS-NS damage in the 3-story building, this less ture in the 6- and 9-story cases. As was demonstrated in Figure 8.4(b), (d), and (f), nonstructural-damage dominates at low-to-moderate intensities, which are associated with high hazard levels.

Figure 8.8 shows the distribution of disaggregated losses. The trends across the different design cases (sampling points) are similar for the 3-story, 6-story, 9-story models. In Figure 8.8, the 9-story buildings with aspect ratio of 0.5 (17 cases) are not included. As shown in Figure 8.8(a), the total loss in the 3-story cases is generally more than the 6- and 9-story cases, which is mostly due to damage to drift sensitive components (structural and DS-NS). The economic loss due to collapse for most of the 9-story cases is higher than the 3-, and 6-story cases, and the contribution from demolition is almost the same across the different building heights.
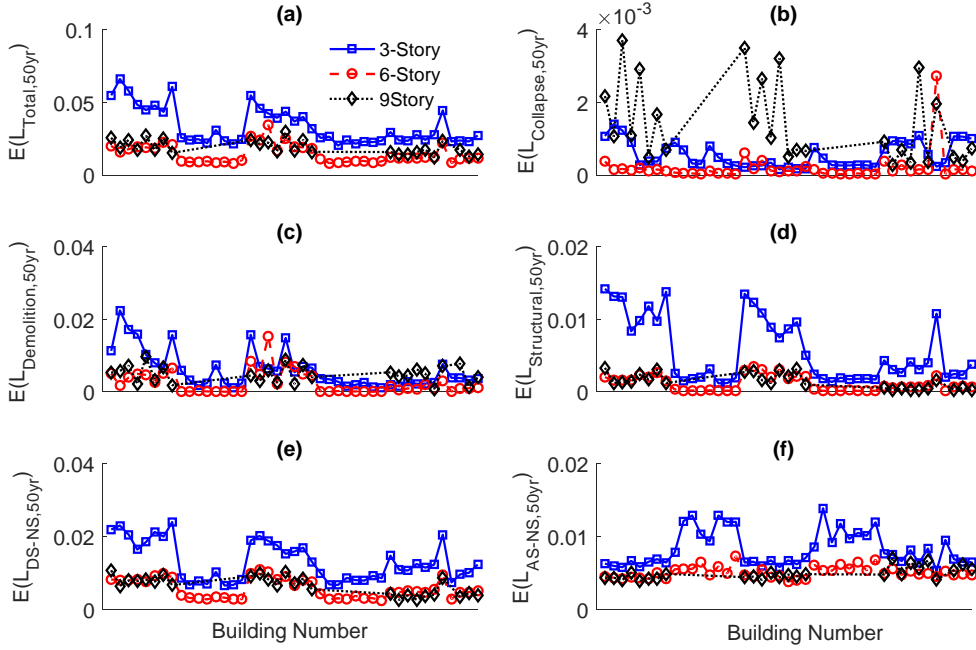
Figure 8.8. Service life economic loss disaggregation for the 3-story, 6-story, and 9-story design cases

8.3.1.3. Sensitvity analysis for earthquake-induced economic losses

The influence of the input parameters (i.e. P_D/W, F_{pt}/W, F_{yf}/W, B/H, and α) on the total and disaggregated losses (demolition, collapse, structural, DS-NS, and AS-NS) shown in Figure 8.7 and 8.8 is discussed in this section.

8.3.1.3.1. Effect of input parameters on demolition loss

Demolition loss is based on residual drift. The ability of controlled rocking braced frames to reduce residual drift is related to the self-centering ratio ($SC = \dfrac{M_{up}}{M_{fsy}} = \dfrac{F_{PT} + 2P_D}{F_{fuse,y}}$).

Generally, increasing normalized dead load (P_D/W) will decrease the demolition loss. Higher dead loads add to the overturning resistance and increases self-centering.

109

Figure 8.8 shows that increasing normalized PT initial force (F_{pt}/W) generally decreases the demolition loss. This is consistent with the role of the PT to restore the CRBF to its original position after earthquake shaking.

Increasing the normalized fuse yield strength (F_{yf}/W) in some cases decreased the demolition loss, as this increases the number of PT strands, which leads to higher SC^* values (Equation 3.12). However, in some cases, when the dead load and PT force are at the maximum level, increasing the fuse strength does not require the addition of PT strands, and demolition losses are not significantly affected since lower shaking levels contribute most to the service life economic loss. Also, in some cases the number of PT strands was increased when the fuse strength was increased (especially structures with higher height) but the demolition loss was not significantly impacted. This can be explained by the fact the increase in overturing moment in taller buildings is greater than the added overturning resistance from the PT because there is less rigid body rotation behavior.

The effect of aspect ratio (B/H) is greater than all the other input parameters. More specifically, increasing aspect ratio significantly reduces the demolition loss. By increasing the bay width of the CRBF, the number of PT strands increases (Equation 3.8). The length and number of fuse links (Equation 3.10) also increases with the bay width, which leads to a greater SC^*. In addition, in some cases, an increase in the number of PT strands is needed to have SC^* greater than unity, which adds to the overturning resistance. Moreover, the effect of the aspect ratio on demolition is smaller for taller buildings.

By increasing the fuse strain hardening ratio (α) in the 3-story cases, the demolition loss is reduced because the ultimate fuse strength is increased, so the number of PT strands is increased to achieve $SC^* \geq 1$ (Equation 3.12). However, in the 6- and 9-story buildings, the demolition loss increases with the strain hardening ratio. This because the nonlinearity in fuse

is greater in tall buildings at lower IM levels and the contribution of the fuse to overturning resistance exceeds that of the PT strands, which inhibits self-centering.

8.3.1.3.2. Effect of input parameters on collapse

Generally, increasing the dead load (P_D/W) reduces the collapse loss. This is not surprising since the dead load provides   overturning resistance moment and reduces the story drift ratio. Higher PT forces (F_{pt}/W) also reduces the collapse losses. In most cases, the fuse yield strength (F_{yf}/W) does not a have significant effect on the collapse loss. However, increasing F_{yf}/W leads to increasing a greater number of PT strands to achieve SC*≥1 (Equation 3.12), which reduces drift demands at   lower intensities. Similar to demolition, the aspect ratio has the greatest influence on collapse losses. The effect of the fuse strain hardening ratio on collapse is the same as demolition loss.

8.3.1.3.3. Effect of input parameters on structural components loss

Structural component repair costs are sensitive to story drifts. Increasing the normalized dead load (P_D/W) decreases structural components loss because of the additional overturning resistance.

Increasing the normalized post-tensioning force (F_{PT}/W) in most cases decreases structural damage, as the stiffness of the structure increases. In a few 3-story design cases, increasing F_{PT}/W reduces the number of PT cables, especially when the fuse strength is large in order to achieve SC*≥1, which leads to smaller member sizes and greater structural components losses.

Increasing the normalized fuse yield strength (F_{yf}/W) decreases the structural components loss and the effect is more significant than F_{PT}/W. The fuse strength affects the braced frame member sizes on both directly, by increasing the demands used in capacity design, and indirectly, by increasing the number of PT stands (and associated fore)needed to achieve

$SC^*{\geq}1$, which also increases the demands used in capacity design . Similar to the demolition loss, the aspect ratio has greatest influence on the structural components loss relative to the other parameters. More specifically, increasing the aspect ratio reduces the structural components loss.

Increasing the fuse strain hardening ratio (α) decreases structural components loss because it increases its ultimate strength and also increases the number of PT stands in order to achieve $SC^*{\geq}1$, which in turn leads to larger member sizes.

8.3.1.3.4. Effect of input parameters on non-structural components loss

The effect of the input parameters on drift-sensitive nonstructural components is the same as structural components (both are drift sensitive components). The effect of the input parameters on acceleration-sensitive nonstructural components is opposite to that of the drift-sensitive nonstructural components. That reasoning is demonstrated in section 8.5, where it was shown that a stiffer structure leads to lower drifts but greater acceleration.

8.3.1.3.5. Effect of input parameters on service-life economic loss

The effect of the input parameters on service-life economic losses $E(L_{50yr})$ is discussed in this subsection. Generally, increasing dead load (P_D/W) will decrease the economic loss ($E(L_{50yr})$) in all the 3-story, 6-story, and 9-story design cases. Whereas in most cases, the initial PT force (F_{PT}/W) has a negligible effect on the total loss. Increasing the fuse yield strength (F_{yf}/W) generally decreases the total loss in the 3-story design cases, since it leads to more PT strands, which reduces the losses in most categories most of the aggregated losses. The effect of F_{yf}/W on the 6-story and 9-story losses is not as substantial as the 3-story cases. This is explained by the fact that, in taller buildings, increasing F_{yf}/W does not require additional PT strands because the dead loads are large enough. .

Increasing the fuse strain hardening ratio (α) decreases the total loss in the 3- and 6-story cases, but increases the losses in the 9-story buildings. Increasing the aspect ratio (*B/H*) decreases the total losses.

8.3.2. Environmental impacts

The effect of the environmental impacts for buildings located in areas of high seismic risks should also be studied to ensure consideration of the entire building's life-cycle effect and consequences of damage repairs (Feese et al. 2014). The initial CRSBF construction (material extraction, material transportation, and etc.) as well as the repair and replacement activities that follow earthquake are considered in the environmental impact assessment.

The Athena Life Cycle Analysis (LCA) software (Athena, 2014) is used to assess the environmental impacts in terms of the fossil fuel consumption (units of mega-joules, MJ) as a proxy for the total primary energy consumption and the amount of greenhouse gas emissions as a proxy for the climate change potential (units of tons of CO_2 equivalents).

The inputs to the Athena LCA estimator are the quantities of the structural and nonstructural building components, and the outputs are the fossil fuel consumption (MJ) and climate change potential (tons of CO_2). Table 8.2 lists the Athena input parameters which includes structural and non-structural components, and the outputs are GWP (global warming potential, CO_2 (tons)) and energy consumption (MJ).

Table 8.2. Athena input parameters

Building component	Unit	Quantity per story	Weight per story (tons)
Gravity connections	Each	104	0.5
Curtain walls	30 ft^2	180	900
Partition walls	100 ft	10	13,000
Suspended ceiling	250 ft^2	40	10,000
Potable water piping	1000 ft	1.7	12.5
HVAC ducting	1000 ft	1	7.35
Fire sprinkler water piping	1000 ft	2	14.7

The initial construction of the controlled rocking braced frame is also included in the environmental impact assessment. The environmental impacts due to earthquake damage are normalized by the building replacement impact. The environmental impacts are obtained from the damage ratio of the building components (ratio of a building component damage cost to the initial cost of the component), therefore, the distribution of CO_2 and Energy are similar to C_{CRBF} (Figure 8.2).

Figures 8.9 and 8.10 show the normalized energy consumption, $E(Energy|Sa_{Te})$, and greenhouse gas emissions, $E(GWP|Sa_{Te})$ conditioned on Sa_{Te} for the center-level sampling point (see Table 5.1) (i.e. $P_D/W = 0.225$, $F_{pt}/W = 0.225$, $F_{yf}/W = 0.4$, $B/H = 0.35$, and $\alpha = 0.04$). The energy consumption for the initial construction of the building is 5,901,308 MJ, 11,802,442 MJ, and 17,703,570 MJ for the baseline 3-story, 6-story, and 9-story buildings, respectively. The greenhouse gas emissions associated with the initial construction of the building is 524,092 tons, 1,048,156 tons, and 1,572,239 tons for 3-story, 6-story, and 9-story buildings, respectively.

Figure 8.9(a),(c) and 8.10(a),(c) show that the DS-NS components contribute the most to the environmental impacts (energy consumption and greenhouse gas emissions) of the 3-story and 6-story buildings. Figure 8.9(e) and 8.10(e) show that demolition has the highest contribution to energy consumption for the 9-story building at higher intensities. However, Figure 8.9(f) and 8.10(f) shows that, at lower intensity levels where the annual rates of exceedance are highest, the DS-NS components (mostly by curtain walls) have the highest contribution. The normalized energy consumption at Sa_{MCE}, (1.5(g), 1.5(g), and 1.25(g) for the 3-story, 6-story, and 9-story baseline case, respectively are 0.50, 0.42, and 0.22. For greenhouse gas emissions, the associated normalized values are 0.57, 0.5, and 0.24 for 3-story, 6-story, and 9-story baseline cases, respectively. Similar to the economic loss, the environmental impacts at the MCE level is smaller for taller buildings (Figure 8.4).

Similar to economic loss (Figure 8.5), Figure 8.11 and 8.12 show that the environmental impacts due to collapse and demolition in the 9-story design cases are higher than that of the 3-story and 6-story cases. In addition, energy consumption, at high intensity levels, due to structural, DS-NS, and AS-NS in the 6-story buildings is larger than 3-story and 9-story buildings.

The 50-year service life of environmental impacts (energy consumption and green gas emission) for the 129 buildings designed based on the five different input parameters (P_D/W, F_{pt}/W, F_{yf}/W, B/H, and α) are computed using Equation 8.6. The primary energy consumption during 50 years of building life is normalized by the initial energy consumption of the building, and similarly, greenhouse gas emission during the 50 year service life is normalized by the emissions corresponding to the initial construction. The normalized disaggregated service-life energy consumption and greenhouse gas emissions for all sampling points are presented in the form of bar charts in Figure 8.13 for 3-story, 6-story, and 9-story, buildings.
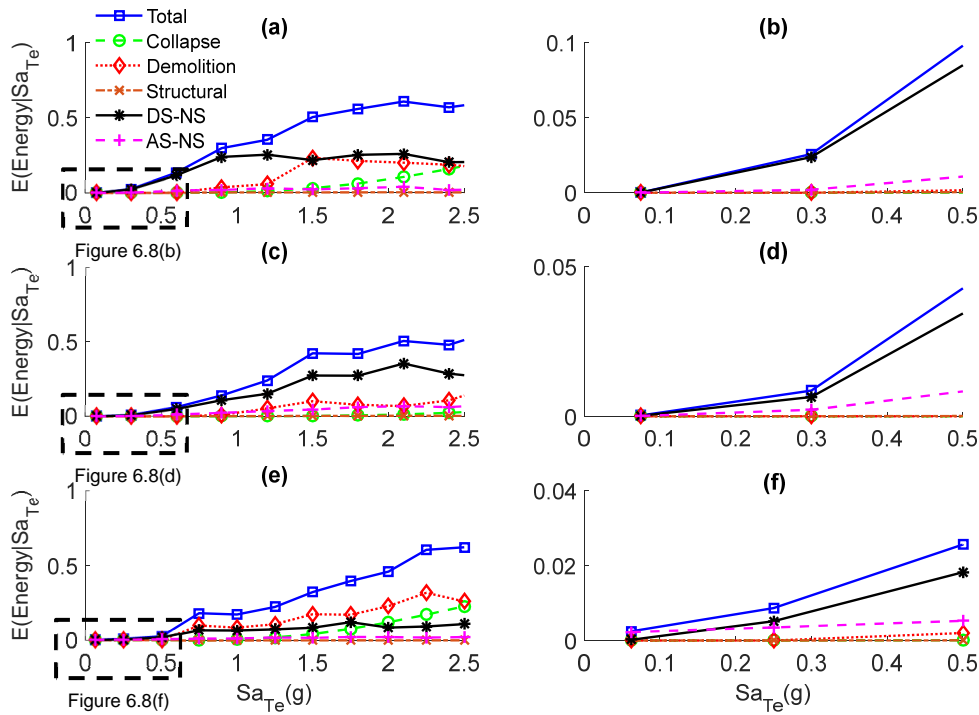
Figure 8.9. Normalized and disaggregated energy consumption for the 3-story (a,b), 6-story (c,d), and 9-story cases (e,f) conditioned on the ground motion intensity for the "center-level" sampling point
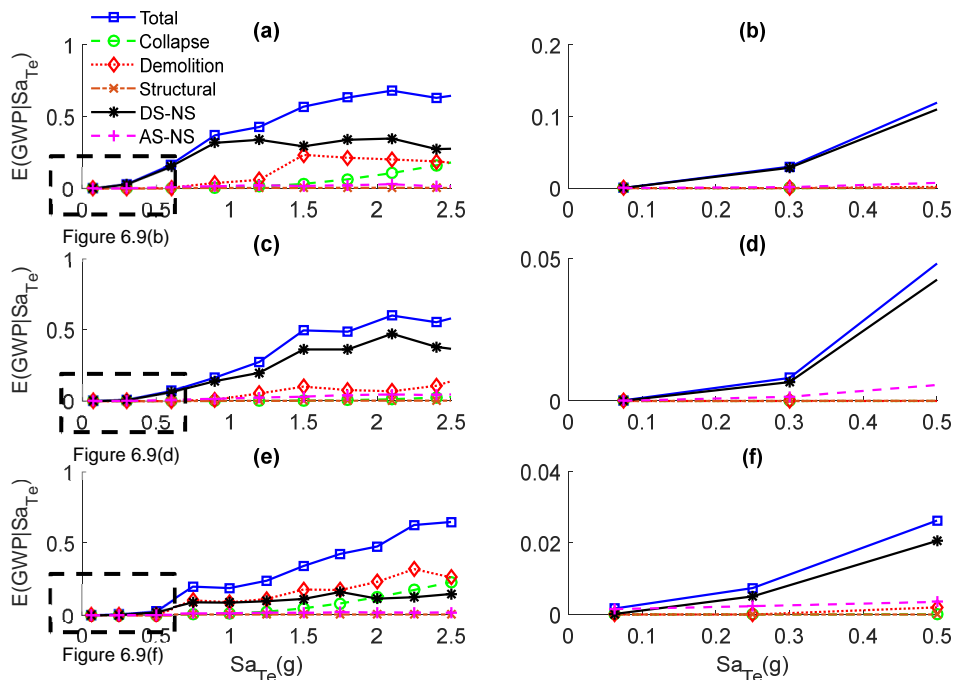
Figure 8.10. Normalized and disaggregated greenhouse gas emission (CO_2) for the 3-story (a,b), 6-story (c,d), and 9-story buildings (e,f) conditioned on the ground motion intensity for the "center-level" sampling point
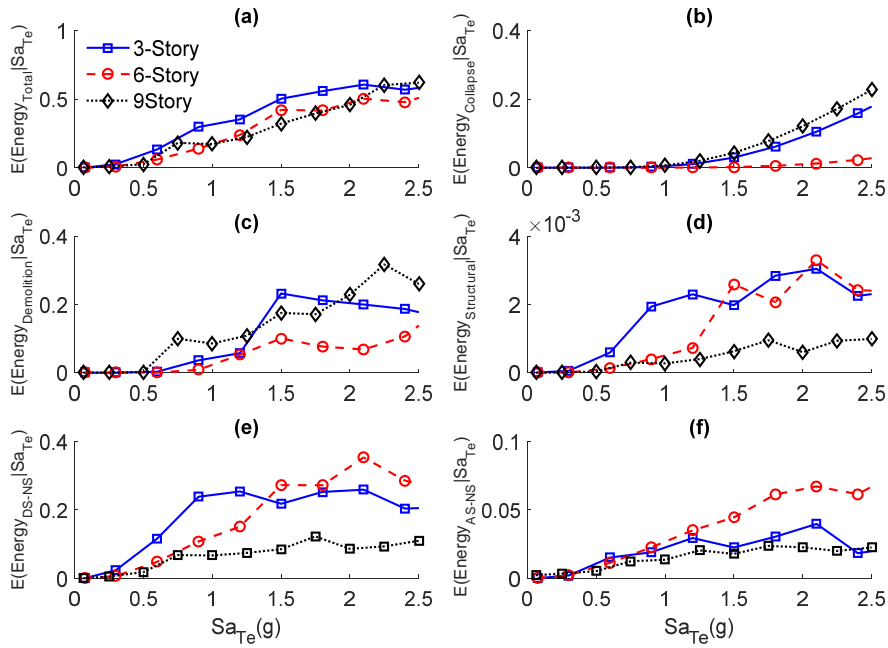
Figure 8.11. Comparison of the expected energy consumption due to collapse, demolition, structural, DS-NS, and AS-NS of 3-story, 6-story, and 9-story buildings conditioned on the ground motion intensity for the "center-level" sampling point
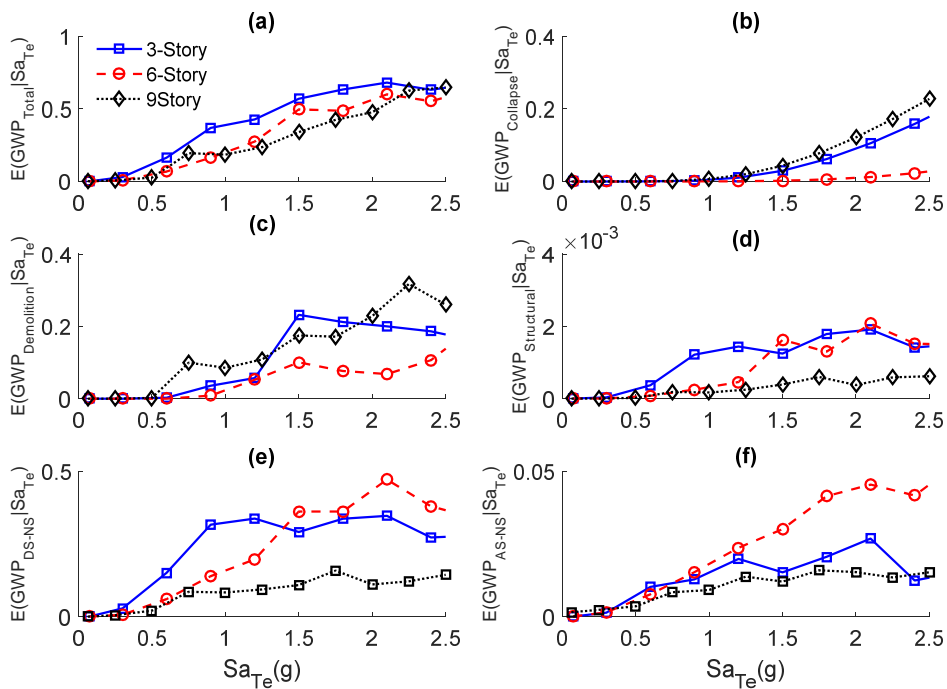
Figure 8.12. Comparison of the expected global warming potential due to collapse, demolition, structural, DS-NS, and AS-NS for the 3-story, 6-story, and 9-story buildings conditioned on the ground motion intensity for the "center-level" sampling point

The normalized service life energy consumption, $E(Energy_{50yr})$ ranges between 9.5% to 42%, 3% to 18%, and 4% to 16% for the 3-story, 6-story, and 9-story building cases, respectively. As was done earlier, the results for the 17 9-story design cases with aspect ratio of 0.5 have been excluded (but it was shown in the Figure 8.12). Therefore, the input parameters can change the service life energy consumption by a factor of 4.4, 5.6, and 4.1 for the 3-story, 6-story, and 9-story buildings, respectively. This result shows that the dispersion in the energy consumption increases with the building height. Additionally, the input parameters can change the service life CO_2 emissions by a factor of 5.6, 8.13, and 5.6 for the 3-story, 6-story, and 9-story buildings, respectively. The variation in the environmental impacts (energy consumption and greenhouse gas emissions) is larger than the economic loss (Figure 8.7), and the variation in the greenhouse gas emissions is larger than the energy consumption across all building heights. Therefore, the greenhouse gas emissions are more sensitive to the selected CRBF design parameters compared to the energy consumption and economic loss. As it was shown in Figure 8.7, the economic losses are dominated by AS-NS or DS-NS. However, Figure 8.13 shows that service life environmental impacts (energy consumption and CO_2 emissions) are always dominated by DS-NS components. However, it should be noted that some of the non-structural components used in the economic loss assessment were not considered in the environmental impact because of lack of the relevant data in Athena (Table 8.2). The environmental impact trend is the same as economic loss (minimum and maximum occurred in the same models).
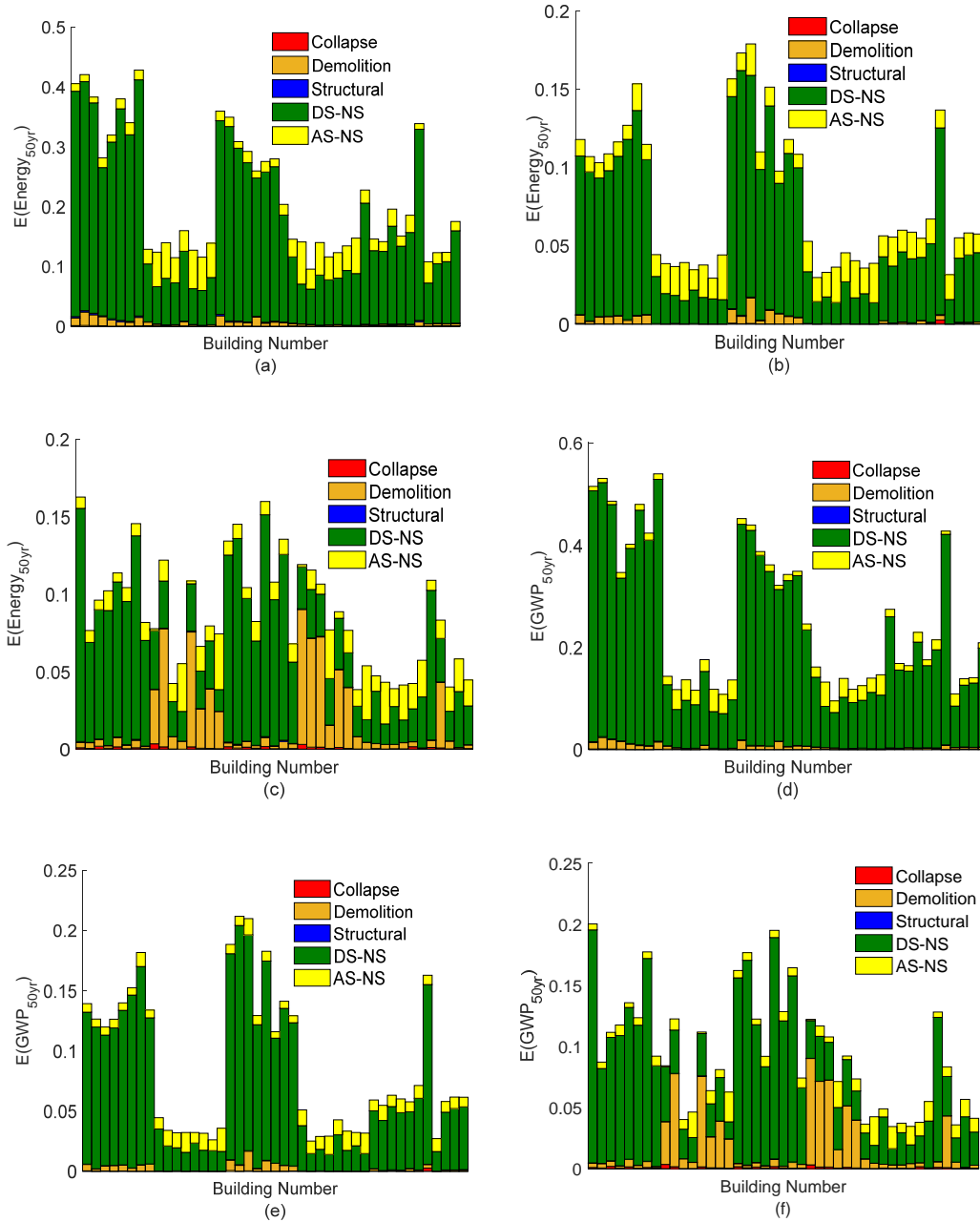
Figure 8.13. Normalized and disaggregated service-life energy consumption (initial construction + earthquake damage) for all sampling points for the (a) 3-story, (b) 6-story, and (c) 9-story and CO2 emissions (d) 3-story, (e) 6-story, and (f) 9-story buildings
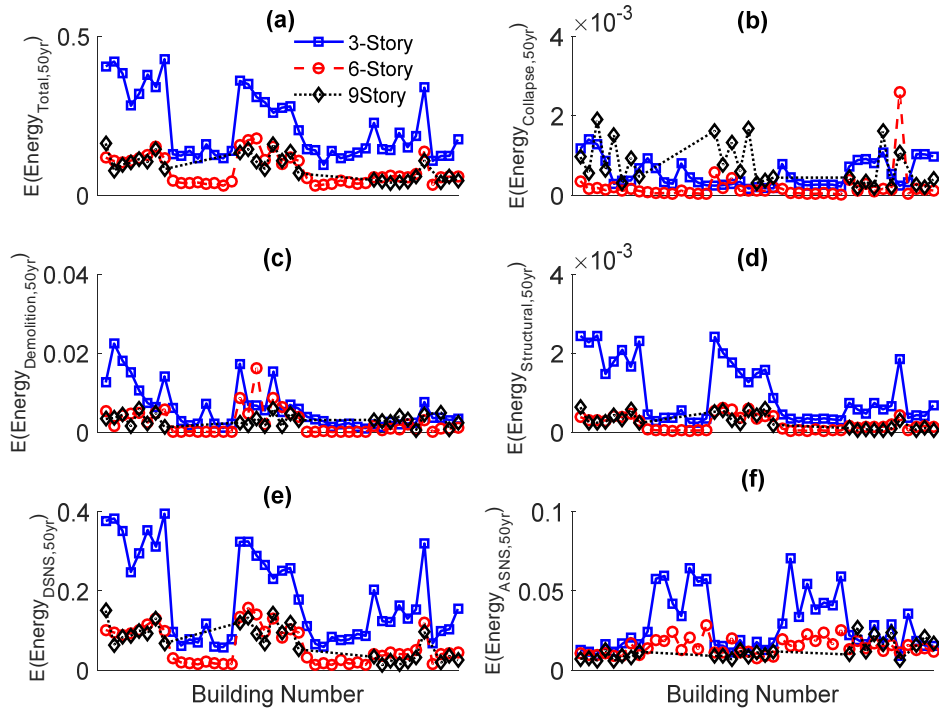
Figure 8.14. Disaggregated service life energy consumption for the 3-story, 6-story, and 9-story cases
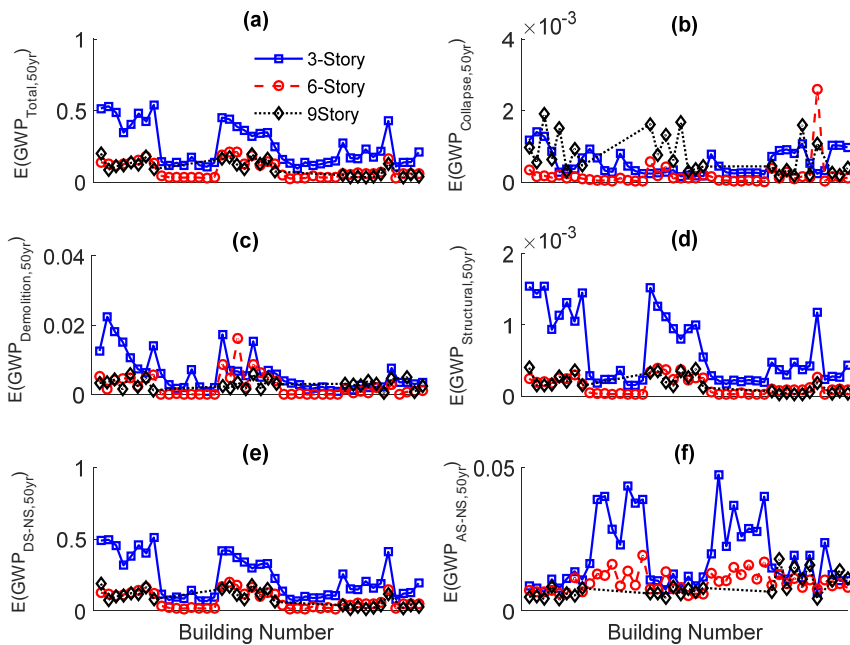
Figure 8.15. Disaggregated service life greenhouse gas emission for the 3-story, 6-story, and 9-story models

Figures 8.14 and 8.15 compares the disaggregation service life environmental impacts for the three building heights across all sampling points. The three building heights show similar trends across the different sampling points.

8.4.   Surrogate Model Development and Verification

Surrogate models are developed and verified for the economic loss and environmental impacts (energy consumption and greenhouse gas emissions). The surrogate models represent the relationship between the input parameters and a response variable ($E(L_{50yr})$, $E(L_{50yr})+C_{CRBF}$, $E(Energy_{50yr})$, $E(Energy_{50yr})+Energy$, $E(GWP_{50yr})$, and $E(GWP_{50yr})+CO_2$), where Energy and CO_2 are the energy consumption and greenhouse gas emission due to construction of the CRBF respectively. As noted earlier, the input parameters are P_D/W, F_{pt}/W, F_{yf}/W, B/H, α, and N, where N is the number of stories 3, 6, and 9. A quadratic polynomial model is used to fit the data generated by the experimental design. The quadratic model for each surrogate model is in the form of Equation 8.7:

$$y = \beta_0 + \sum_{i=1}^{k} \beta_i x_i + \sum_{i=1}^{k}\sum_{j=i}^{k} \beta_{ij} x_i x_j \qquad (8.7)$$

Where the β's are the unknown regression coefficients and the x's are the independent predictors (factors). The "fitnlm" function in Matlab was used to estimate model coefficients (β's) using an iterative generalized least squares algorithm. Two equations are developed for each response variable ($E(L_{50yr})$, $E(L_{50yr})+C_{CRBF}$, $E(Energy_{50yr})$, $E(Energy_{50yr})+Energy$, $E(GWP_{50yr})$, and $E(GWP_{50yr})+CO_2$). One that considers all the sampling points for the 3-story, 6-story, and 9-story buildings (129 data points), and a second that excludes the sampling points that have an impractical bay width ($B/H=0.5$) for the 9-story cases (112 data points). The coefficients of the regression analysis are summarized in Table 8.3, 8.4, and 8.5 for service life economic loss and environmental impacts.

Quantitative measures of the surrogate model's ability to predict economic loss ($E(L_{50yr})$, $E(L_{50yr})+C_{CRBF}$) of the training data are summarized in Table 8.6. The coefficient of determination (R^2) is computed as the ratio of the sum of squares from the surrogate model responses to that of the actual responses. Another quantitative study of prediction model's accuracy is the median absolute relative deviation (*MARD*), which is the median absolute difference between the predicted and actual response normalized by the actual values (Sun et al. 2017). As the Table 8.6 shows, the equation based on the 112 data points are more accurate than the ones developed using the full 129 sampling points for both response variables ($E(L_{50yr})$, $E(L_{50yr})+C_{CRBF}$). The associated R^2 values are 0.9 and 0.93 and the *MARD* values are 0.087 and 0.06 for $E(L_{50yr})$ and $E(L_{50yr})+C_{CRBF}$, respectively.

Table 8.7 summarizes the predictive performance of the service life environmental impacts ($E(Energy_{50yr})$, $E(Energy_{50yr})+Energy$, $E(GWP_{50yr})$, and $E(GWP_{50yr})+CO_2$) equations based on the training data.7. Both equations provide similar and reasonable R^2 and *MARD* which are larger than 0.9 and less than 0.2, respectively. Also, it is shown that the predictive equations with *MARD* less than 0.1 are obtained when the environmental impacts associated with the initial construction is considered i.e. $E(Energy_{50yr})+Energy$ and $E(GWP_{50yr})+CO_2$.

To further assess the predictive performance of the surrogate models, additional models with heights that are different from the ones used to develop the training data (3, 6, and 9) are created. Table 8.4 lists the testing sampling points, which are 8 4-story design cases and 5 8-story design cases. The testing sampling points (P_D/W, F_{pt}/W, F_{yf}/W, B/H, α), which are selected based on the practical and rational values for the 4-story and 8-story cases and are listed in Table 8.8. All the testing input parameters are within the range of the training input parameters except the normalized dead load (P_D/W), which, for some cases (models 1, 2, 3, 9, and 10) is less than the minimum training range (0.15). Nonlinear structural models of the CRSBFs with the factor combinations specified for the testing models are analyzed and the

actual impact values are compared with the predictions from surrogate models. Table 8.9 lists normalized absolute errors (absolute difference between actual and predicted response normalized by the actual response) of the economic loss ($E(L_{50yr})$, $E(L_{50yr})+C_{CRBF}$) for both equations. It shows that the equations developed excluding the data associated with the impractical aspect ratios (0.5) for the 9-story cases provide more accurate results for both impacts. Also, the prediction for $E(L_{50yr})+C_{CRBF}$ for some cases is more precise than $E(L_{50yr})$. The median normalized errors for the 13 testing models for $E(L_{50yr})$ are 0.43 and 0.18 for the equations with and without the impractical 9-story cases, respectively. For $E(L_{50yr})+C_{CRBF}$, the associated values are 0.16 and 0.05, respectively. The models with normalized dead load outside of the training data range (Models 1, 2, 3, 9, and 10) provide good predictions, especially for $E(L_{50yr})+C_{CRBF.}$

Tables 8.10 and 8.11 show the errors in the environmental impacts considering the models with and without the sampling points corresponding to the impractical aspect ratios. The accuracy of the environmental impacts for testing models are similar to that of the training models. The median errors for the 13 testing models for $E(Energy_{50yr})$ is 0.32 and 0.31, for $E(Energy_{50yr})+Energy$ are 0.07 and 0.10, for $E(GWP_{50yr})$ are 0.40 and 0.42, and for $E(GWP_{50yr})+CO_2$ are 0.14 and 0.14, respectively. Similar to the economic loss, the surrogate models predict the initial construction plus service life earthquake damage environmental impact ($E(Energy_{50yr})+Energy$ and $E(GWP_{50yr})+CO_2$) better than when only the earthquake-induced impacts ($E(Energy_{50yr})$ and $E(GWP_{50yr})$) are considered. Figures 8.16 and 8.17 show the actual vs the predicted values of the training and testing models for economic loss and environmental impacts, respectively.

Table 8.3. β_{i}'s and β_{ij}'s for all the response variables for $E(L_{50yr})$ and $E(L_{50yr})+C_{CRBF}$ for EQ(1) and EQ(2)

i	Input parameter, x_i	EQ(1): $E(L_{50yr})$	EQ(1): $E(L_{50yr})+C_{CRBF}$	EQ(2): $E(L_{50yr})$	EQ(2): $E(L_{50yr})+C_{CRBF}$
0	intercept	0.147	0.303	0.178	0.328
1	P_D/W	0.124	0.002	-0.033	-0.167
2	F_{pt}/W	0.181	-0.038	-0.026	-0.250
3	F_{yf}/W	0.055	0.149	-0.071	-0.048
4	B/H	-0.555	-1.246	-0.345	-0.922
5	α	0.675	1.399	0.165	0.577
6	N	-0.031	-0.050	-0.023	-0.038

i	Input parameter, (x_i,x_j)	EQ(1): $\beta_{(i's)}$ "for" $E(L_{50yr})$					
		P_D/W	F_{pt}/W	F_{yf}/W	B/H	α	N
1	P_D/W	0.037					
2	F_{pt}/W	-0.053	-0.038				
3	F_{yf}/W	-0.054	0.163	0.008			
4	B/H	-0.060	-0.337	-0.060	0.623		
5	α	-0.915	-0.383	-1.449	0.442	-2.593	
6	N	-0.014	-0.024	-0.005	0.037	0.042	0.002

i	Input parameter, (x_i,x_j)	EQ(2): $\beta_{(i's)}$ "for" $E(L_{50yr})$					
		P_D/W	F_{pt}/W	F_{yf}/W	B/H	α	N
1	P_D/W	0.054					
2	F_{pt}/W	0.029	-0.021				
3	F_{yf}/W	0.028	0.056	0.017			
4	B/H	0.066	0.017	0.059	0.260		
5	α	-0.448	-0.393	-0.234	0.289	-2.358	
6	N	-0.005	0.001	0.003	0.011	0.031	0.001

i	Input parameter, (x_i,x_j)	EQ(1): $\beta_{(i's)}$ "for" $E(L_{50yr})+C_{CRBF}$					
		P_D/W	F_{pt}/W	F_{yf}/W	B/H	α	N
1	P_D/W	0.157					
2	F_{pt}/W	0.136	0.020				
3	F_{yf}/W	-0.248	0.007	0.133			
4	B/H	0.283	0.266	-0.478	1.439		
5	α	-1.902	-1.197	1.171	-2.288	0.484	
6	N	-0.011	-0.009	-0.001	0.079	0.019	0.003

i	Input parameter, (x_i,x_j)	EQ(2): $\beta_{(i's)}$ "for" $E(L_{50yr})+C_{CRBF}$					
		P_D/W	F_{pt}/W	F_{yf}/W	B/H	α	N
1	P_D/W	0.250					
2	F_{pt}/W	0.279	0.113				
3	F_{yf}/W	-0.194	-0.085	0.185			
4	B/H	0.379	0.538	-0.337	0.962		
5	α	-1.585	-1.137	3.046	-2.473	1.789	
6	N	-0.004	0.010	0.009	0.048	0.006	0.002

Table 8.4. β_i's and β_{ij}'s for all the response variables for E(Energy$_{50yr}$) and E(GWP$_{50yr}$) for EQ(1) and EQ(2)

i	Input parameter, x_i	EQ(1): E(Energy$_{50yr}$)	EQ(1): E(GWP$_{50yr}$)	EQ(2): E(Energy$_{50yr}$)	EQ(2): E(GWP$_{,50yr}$)
0	intercept	1.248	1.588	1.265	1.608
1	P_D/W	-0.572	-0.714	-0.608	-0.742
2	F_{pt}/W	-0.252	-0.336	-0.202	-0.235
3	F_{yf}/W	-0.470	-0.540	-0.532	-0.579
4	B/H	-2.598	-3.395	-2.602	-3.474
5	α	2.890	3.467	2.745	3.486
6	N	-0.153	-0.191	-0.153	-0.195

EQ(1): $\beta_{(i)s}$ "for" E(Energy$_{50yr}$)

i	Input parameter, (x_i, x_j)	P_D/W	F_{pt}/W	F_{yf}/W	B/H	α	N
1	P_D/W	1.157					
2	F_{pt}/W	-0.221	-0.017				
3	F_{yf}/W	0.052	0.763	0.354			
4	B/H	0.417	0.162	0.187	2.001		
5	α	-1.278	-1.848	-3.625	1.674	-32.646	
6	N	-0.014	-0.013	0.007	0.094	0.186	0.008

EQ(2): $\beta_{(i)s}$ "for" E(Energy$_{50yr}$)

i	Input parameter, (x_i, x_j)	P_D/W	F_{pt}/W	F_{yf}/W	B/H	α	N
1	P_D/W	1.104					
2	F_{pt}/W	-0.219	-0.069				
3	F_{yf}/W	0.222	0.686	0.325			
4	B/H	0.385	0.233	0.290	1.943		
5	α	-0.975	-2.861	-3.642	2.259	-33.385	
6	N	-0.017	-0.008	0.014	0.087	0.227	0.008

EQ(1): $\beta_{(i)s}$ "for" E(GWP$_{50yr}$)

i		P_D/W	F_{pt}/W	F_{yf}/W	B/H	α	N
1	P_D/W	1.441					
2	F_{pt}/W	-0.287	-0.094				
3	F_{yf}/W	0.086	0.961	0.338			
4	B/H	0.411	0.247	0.233	2.564		
5	α	-1.491	-2.089	-4.260	2.171	-41.951	
6	N	-0.017	-0.014	0.012	0.127	0.234	0.009

EQ(2): $\beta_{(i)s}$ "for" E(GWP$_{50yr}$)

i		P_D/W	F_{pt}/W	F_{yf}/W	B/H	α	N
1	P_D/W	1.362					
2	F_{pt}/W	-0.262	-0.172				
3	F_{yf}/W	0.286	0.864	0.294			
4	B/H	0.362	0.285	0.334	2.593		
5	α	-1.282	-3.490	-4.564	2.897	-43.056	
6	N	-0.021	-0.011	0.019	0.125	0.286	0.009

Table 8.5. β_i's and β_{ij}'s for all the response variables for $E(Energy_{50yr})+Energy$ and $E(GWP_{50yr})+CO_2$ for EQ(1) and EQ(2)

i	Input parameter, x_i	EQ(1): $E(Energy_{50yr})+Energy$	EQ(1): $E(GWP_{50yr})+CO_2$	EQ(2): $E(Energy_{50yr})+Energy$	EQ(2): $E(GWP_{50yr})+CO_2$
0	intercept	2.105	2.120	2.090	2.120
1	P_D/W	-1.278	-1.153	-1.377	-1.219
2	F_{pt}/W	-1.480	-1.097	-1.457	-1.013
3	F_{yf}/W	-0.023	-0.262	-0.496	-0.557
4	B/H	-6.343	-5.719	-5.684	-5.387
5	α	6.538	5.731	4.526	4.591
6	N	-0.257	-0.256	-0.232	-0.244

Input parameter, (x_i,x_j)	EQ(1): $\beta_{(i's)}$ "for" $E(Energy_{50yr})+Energy$					
	P_D/W	F_{pt}/W	F_{yf}/W	B/H	α	N
P_D/W	1.908					
F_{pt}/W	0.798	0.309				
F_{yf}/W	-1.007	-0.063	1.055			
B/H	2.271	3.446	-2.043	6.393		
α	-6.644	-6.261	10.601	-12.838	-16.306	
N	0.003	0.072	0.033	0.318	0.088	0.011

Input parameter, (x_i,x_j)	EQ(2): $\beta_{(i's)}$ "for" $E(Energy_{50yr})+Energy$					
	P_D/W	F_{pt}/W	F_{yf}/W	B/H	α	N
P_D/W	2.280					
F_{pt}/W	1.135	0.681				
F_{yf}/W	-0.989	-0.046	1.264			
B/H	2.062	3.050	-1.801	5.669		
α	-7.132	-6.832	14.222	-12.231	-11.074	
N	-0.012	0.044	0.050	0.284	0.131	0.010

	EQ(1): $\beta_{(i's)}$ "for" $E(GWP_{50yr})+CO_2$					
	P_D/W	F_{pt}/W	F_{yf}/W	B/H	α	N
P_D/W	1.907					
F_{pt}/W	0.345	0.109				
F_{yf}/W	-0.571	0.448	0.773			
B/H	1.561	2.285	-1.152	5.290		
α	-4.821	-4.827	4.569	-6.835	-31.811	
N	-0.007	0.039	0.028	0.267	0.174	0.012

	EQ(2): $\beta_{(i's)}$ "for" $E(GWP_{50yr})+CO2$					
	P_D/W	F_{pt}/W	F_{yf}/W	B/H	α	N
P_D/W	2.092					
F_{pt}/W	0.578	0.294				
F_{yf}/W	-0.466	0.410	0.877			
B/H	1.403	2.033	-0.964	4.905		
α	-5.103	-5.954	6.522	-6.095	-29.210	
N	-0.018	0.021	0.041	0.248	0.226	0.011

126

Table 8.6. Economic loss surrogate model details

Response variable		R^2	MARD
EQ (1)	$E(L_{50yr})$	0.68	0.25
	$E(L_{50yr})+C_{CRBF}$	0.89	0.11
EQ (2)	$E(L_{50yr})$	0.9	0.087
	$E(L_{50yr})+C_{CRBF}$	0.93	0.06

Table 8.7. Environmental surrogate model details

Response variable		R^2	MARD
EQ (1)	$E(Energy_{50yr})$	0.91	0.16
	$E(GWP_{50yr})$	0.91	0.18
	$E(Energy_{50yr})+Energy$	0.94	0.06
	$E(CO_{2,50yr})+CO_2$	0.93	0.06
EQ (2)	$E(Energy_{50yr})$	0.91	0.15
	$E(GWP_{50yr})$	0.91	0.19
	$E(Energy_{50yr})+Energy$	0.93	0.07
	$E(GWP_{50yr})+CO_2$	0.92	0.07

Table 8.8. Input parameters of verification models

Model	P_D/W	F_{pt}/W	F_{yf}/W	B/H	α	N
1	0.04	0.2	0.25	0.4	0.04	4
2	0.05	0.15	0.2	0.5	0.03	4
3	0.06	0.1	0.15	0.6	0.02	4
4	0.15	0.15	0.3	0.55	0.04	4
5	0.2	0.2	0.35	0.45	0.02	4
6	0.3	0.25	0.45	0.4	0.03	4
7	0.255	0.15	0.4	0.5	0.04	4
8	0.15	0.3	0.4	0.3	0.03	4
9	0.05	0.2	0.3	0.3	0.02	8
10	0.06	0.3	0.35	0.25	0.03	8
11	0.15	0.3	0.45	0.2	0.02	8
12	0.2	0.25	0.4	0.35	0.04	8
13	0.25	0.225	0.5	0.3	0.035	8

Table 8.9. Verification models errors for $E(L_{50yr})+E(L_{50yr})+C_{CRBF}$

Model	Response variable		Error	Model	Response variable		Error
1	EQ(1)	$E(L_{50yr})$	0.31	9	EQ(1)	$E(L_{50yr})$	0.31
		$E(L_{50yr})+C_{CRBF}$	0.28			$E(L_{50yr})+C_{CRBF}$	0.16
	EQ(2)	$E(L_{50yr})$	0.03		EQ(2)	$E(L_{50yr})$	0.41
		$E(L_{50yr})+C_{CRBF}$	0.05			$E(L_{50yr})+C_{CRBF}$	0.14
2	EQ(1)	$E(L_{50yr})$	0.50	10	EQ(1)	$E(L_{50yr})$	0.37
		$E(L_{50yr})+C_{CRBF}$	0.13			$E(L_{50yr})+C_{CRBF}$	0.07
	EQ(2)	$E(L_{50yr})$	0.25		EQ(2)	$E(L_{50yr})$	0.18
		$E(L_{50yr})+C_{CRBF}$	0.16			$E(L_{50yr})+C_{CRBF}$	0.00
3	EQ(1)	$E(L_{50yr})$	1.00	11	EQ(1)	$E(L_{50yr})$	0.49
		$E(L_{50yr})+C_{CRBF}$	0.69			$E(L_{50yr})+C_{CRBF}$	0.12
	EQ(2)	$E(L_{50yr})$	0.06		EQ(2)	$E(L_{50yr})$	0.32
		$E(L_{50yr})+C_{CRBF}$	0.38			$E(L_{50yr})+C_{CRBF}$	0.07
4	EQ(1)	$E(L_{50yr})$	1.00	12	EQ(1)	$E(L_{50yr})$	0.11
		$E(L_{50yr})+C_{CRBF}$	0.32			$E(L_{50yr})+C_{CRBF}$	0.01
	EQ(2)	$E(L_{50yr})$	0.40		EQ(2)	$E(L_{50yr})$	0.10
		$E(L_{50yr})+C_{CRBF}$	0.06			$E(L_{50yr})+C_{CRBF}$	0.04
5	EQ(1)	$E(L_{50yr})$	0.28	13	EQ(1)	$E(L_{50yr})$	0.42
		$E(L_{50yr})+C_{CRBF}$	0.22			$E(L_{50yr})+C_{CRBF}$	0.00
	EQ(2)	$E(L_{50yr})$	0.00		EQ(2)	$E(L_{50yr})$	0.20
		$E(L_{50yr})+C_{CRBF}$	0.11			$E(L_{50yr})+C_{CRBF}$	0.05
6	EQ(1)	$E(L_{50yr})$	0.50				
		$E(L_{50yr})+C_{CRBF}$	0.32				
	EQ(2)	$E(L_{50yr})$	0.10				
		$E(L_{50yr})+C_{CRBF}$	0.17				
7	EQ(1)	$E(L_{50yr})$	0.46				
		$E(L_{50yr})+C_{CRBF}$	0.02				
	EQ(2)	$E(L_{50yr})$	0.23				
		$E(L_{50yr})+C_{CRBF}$	0.04				
8	EQ(1)	$E(L_{50yr})$	0.12				
		$E(L_{50yr})+C_{CRBF}$	0.16				
	EQ(2)	$E(L_{50yr})$	0.18				
		$E(L_{50yr})+C_{CRBF}$	0.02				

Table 8.10. Verification models error for $E(Energy_{50yr})$ and $E(Energy_{50yr})$+Energy

Model		Response variable	Error		Model		Response variable	Error
1	EQ(1)	$E(Energy_{50yr})$	0.36		9	EQ(1)	$E(Energy_{50yr})$	0.49
		$E(Energy_{50yr})$+Energy	0.01				$E(Energy_{50yr})$+Energy	0.25
	EQ(2)	$E(Energy_{50yr})$	0.39			EQ(2)	$E(Energy_{50yr})$	0.51
		$E(Energy_{50yr})$+Energy	0.12				$E(Energy_{50yr})$+Energy	0.20
2	EQ(1)	$E(Energy_{50yr})$	0.66		10	EQ(1)	$E(Energy_{50yr})$	0.32
		$E(Energy_{50yr})$+Energy	0.19				$E(Energy_{50yr})$+Energy	0.07
	EQ(2)	$E(Energy_{50yr})$	0.64			EQ(2)	$E(Energy_{50yr})$	0.31
		$E(Energy_{50yr})$+Energy	0.31				$E(Energy_{50yr})$+Energy	0.05
3	EQ(1)	$E(Energy_{50yr})$	0.27		11	EQ(1)	$E(Energy_{50yr})$	0.31
		$E(Energy_{50yr})$+Energy	0.42				$E(Energy_{50yr})$+Energy	0.05
	EQ(2)	$E(Energy_{50yr})$	0.16			EQ(2)	$E(Energy_{50yr})$	0.29
		$E(Energy_{50yr})$+Energy	0.48				$E(Energy_{50yr})$+Energy	0.06
4	EQ(1)	$E(Energy_{50yr})$	0.70		12	EQ(1)	$E(Energy_{50yr})$	0.41
		$E(Energy_{50yr})$+Energy	0.12				$E(Energy_{50yr})$+Energy	0.07
	EQ(2)	$E(Energy_{50yr})$	0.66			EQ(2)	$E(Energy_{50yr})$	0.42
		$E(Energy_{50yr})$+Energy	0.10				$E(Energy_{50yr})$+Energy	0.09
5	EQ(1)	$E(Energy_{50yr})$	0.10		13	EQ(1)	$E(Energy_{50yr})$	0.47
		$E(Energy_{50yr})$+Energy	0.14				$E(Energy_{50yr})$+Energy	0.02
	EQ(2)	$E(Energy_{50yr})$	0.09			EQ(2)	$E(Energy_{50yr})$	0.45
		$E(Energy_{50yr})$+Energy	0.11				$E(Energy_{50yr})$+Energy	0.01
6	EQ(1)	$E(Energy_{50yr})$	0.07					
		$E(Energy_{50yr})$+Energy	0.20					
	EQ(2)	$E(Energy_{50yr})$	0.05					
		$E(Energy_{50yr})$+Energy	0.17					
7	EQ(1)	$E(Energy_{50yr})$	0.27					
		$E(Energy_{50yr})$+Energy	0.05					
	EQ(2)	$E(Energy_{50yr})$	0.27					
		$E(Energy_{50yr})$+Energy	0.05					
8	EQ(1)	$E(Energy_{50yr})$	0.28					
		$E(Energy_{50yr})$+Energy	0.01					
	EQ(2)	$E(Energy_{50yr})$	0.30					
		$E(Energy_{50yr})$+Energy	0.03					

Table 8.11. Verification models error for $E(GWP_{50yr})$ and $E(GWP_{50yr})+CO_2$

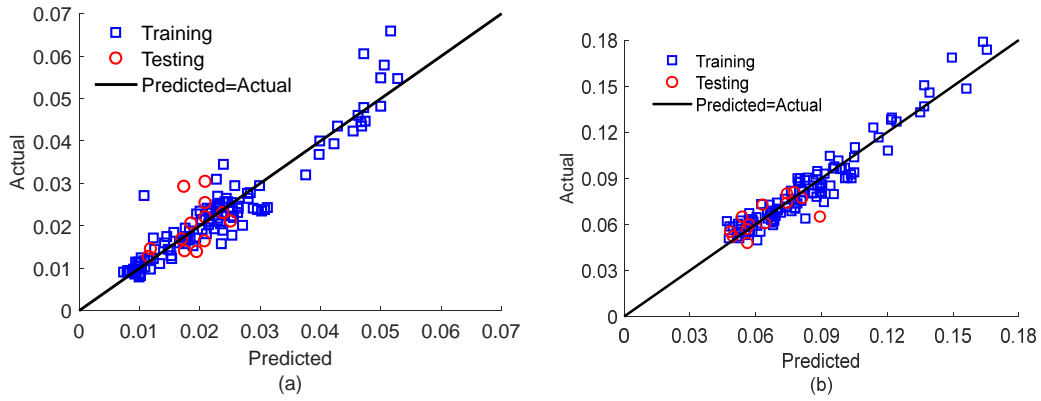| Model		Response variable	Error	Model		Response variable	Error
1	EQ(1)	$E(GWP_{50yr})$	0.40	9	EQ(1)	$E(GWP_{50yr})$	0.51
		$E(GWP_{50yr})+CO_2$	0.14			$E(GWP_{50yr})+CO_2$	0.34
	EQ(2)	$E(GWP_{50yr})$	0.42		EQ(2)	$E(GWP_{50yr})$	0.53
		$E(GWP_{50yr})+CO_2$	0.21			$E(GWP_{50yr})+CO_2$	0.30
2	EQ(1)	$E(GWP_{50yr})$	0.69	10	EQ(1)	$E(GWP_{50yr})$	0.34
		$E(GWP_{50yr})+CO_2$	0.31			$E(GWP_{50yr})+CO_2$	0.15
	EQ(2)	$E(GWP_{50yr})$	0.68		EQ(2)	$E(GWP_{50yr})$	0.33
		$E(GWP_{50yr})+CO_2$	0.40			$E(GWP_{50yr})+CO_2$	0.14
3	EQ(1)	$E(GWP_{50yr})$	0.32	11	EQ(1)	$E(GWP_{50yr})$	0.32
		$E(GWP_{50yr})+CO_2$	0.41			$E(GWP_{50yr})+CO_2$	0.13
	EQ(2)	$E(GWP_{50yr})$	0.22		EQ(2)	$E(GWP_{50yr})$	0.31
		$E(GWP_{50yr})+CO_2$	0.45			$E(GWP_{50yr})+CO_2$	0.13
4	EQ(1)	$E(GWP_{50yr})$	0.87	12	EQ(1)	$E(GWP_{50yr})$	0.46
		$E(GWP_{50yr})+CO_2$	0.23			$E(GWP_{50yr})+CO_2$	0.11
	EQ(2)	$E(GWP_{50yr})$	0.87		EQ(2)	$E(GWP_{50yr})$	0.45
		$E(GWP_{50yr})+CO_2$	0.22			$E(GWP_{50yr})+CO_2$	0.12
5	EQ(1)	$E(GWP_{50yr})$	0.22	13	EQ(1)	$E(GWP_{50yr})$	0.51
		$E(GWP_{50yr})+CO_2$	0.06			$E(GWP_{50yr})+CO_2$	0.10
	EQ(2)	$E(GWP_{50yr})$	0.20		EQ(2)	$E(GWP_{50yr})$	0.50
		$E(GWP_{50yr})+CO_2$	0.05			$E(GWP_{50yr})+CO_2$	0.09
6	EQ(1)	$E(GWP_{50yr})$	0.10				
		$E(GWP_{50yr})+CO_2$	0.11				
	EQ(2)	$E(GWP_{50yr})$	0.12				
		$E(GWP_{50yr})+CO_2$	0.09				
7	EQ(1)	$E(GWP_{50yr})$	0.30				
		$E(GWP_{50yr})+CO_2$	0.00				
	EQ(2)	$E(GWP_{50yr})$	0.31				
		$E(GWP_{50yr})+CO_2$	0.00				
8	EQ(1)	$E(GWP_{50yr})$	0.66				
		$E(GWP_{50yr})+CO_2$	0.24				
	EQ(2)	$E(GWP_{50yr})$	0.67				
		$E(GWP_{50yr})+CO_2$	0.27				

Figure 8.16. Actual versus surrogate-model-predicted impacts: (a) $E(L_{50yr})$ and (b) $E(L_{50yr})+C_{CRBF}$
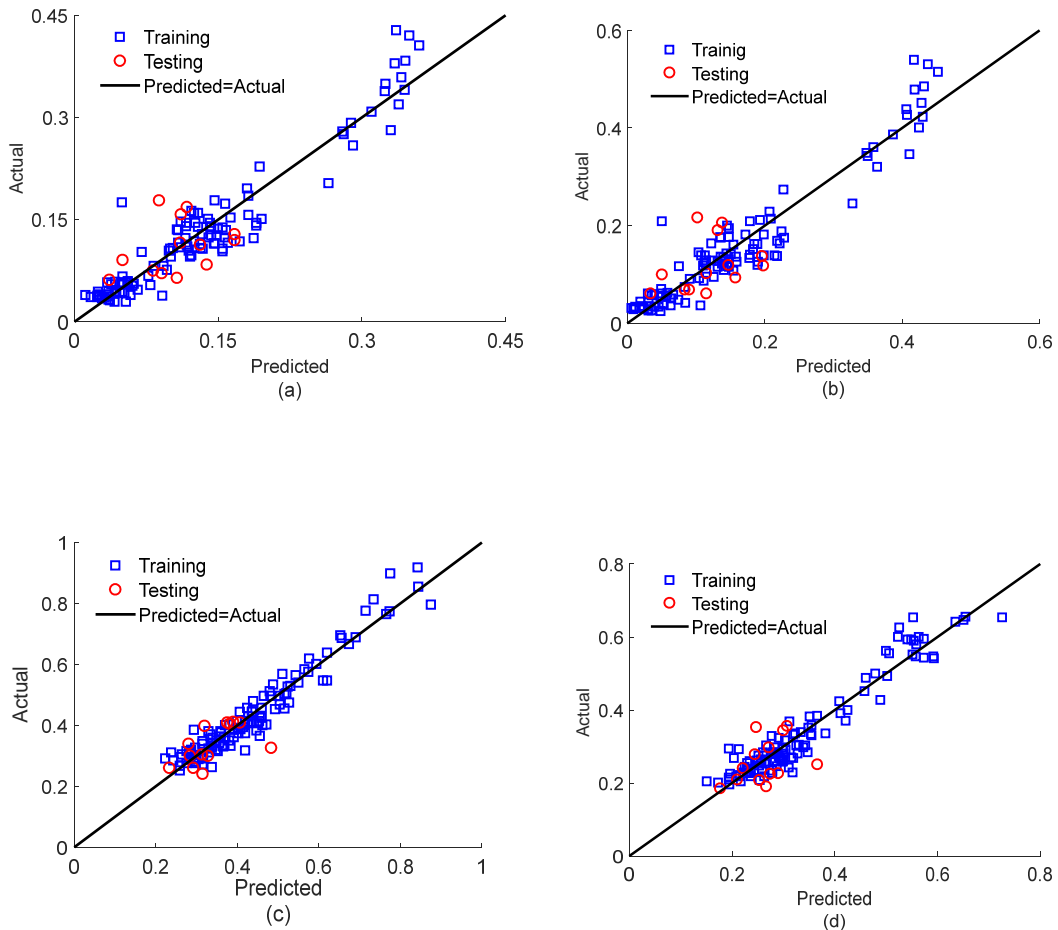

Figure 8.17. Actual versus surrogate-model-predicted impacts: (a) $E(Energy_{50yr})$, (b) $E(GWP_{50yr})$, (c) $E(Energy_{50yr})+Energy$, and (d) $E(GWP_{50yr})+CO_2$

8.5.   Sensitivity of Impacts to Individuals Predictors

In order to further investigate the differences in how the aggregated metrics are affected by the CRSBF design, their sensitivity to variations in the individual structural input parameters is evaluated. The surrogate models (EQ(2)) are used to compute aggregated impacts based on the two metrics, with each input parameter incrementally varied between the upper and lower levels (Table 5.1) while the other four are equal to central level input parameters. Figure 8.18 shows the effects of each input parameter on the aggregated economic loss impact metrics for 3-story, 6-story, and 9-story cases. The horizontal axis is the input parameters (e.g. P_D/W), which is normalized difference between the maximum and minimum values (e.g.

$$\frac{P_D/W - (P_D/W)_{min}}{(P_D/W)_{max} - (P_D/W)_{min}}$$
) such that all the normalized parameters are in the same range of [0,1].

Among all the input parameters, the aspect ratio is observed to have the greatest effect on both $E(L_{50yr})$ and $E(L_{50yr})+C_{CRBF}$. By increasing the height of the structure, the minimum impacts occurs at a lower B/H, and also, for the same building height, the minimum $E(L_{50yr})+C_{CRBF}$ occurs at a lower B/H compared to $E(L_{50yr})$. The B/H corresponding to the minimum $E(L_{50yr})$ is 0.5, 0.43, 0.35 for 3-story, 6-story, and 9-story buildings respectively, and minimum $E(L_{50yr})+C_{CRBF}$ is 0.42, 0.34, and 0.27 for 3-story, 6-story, and 9-story buildings respectively. This result is consistent with the assumption of the maximum aspect ratio for the 9-story models being 0.35. Increasing the aspect ratio adds to the overturning resistance and increasing the braced frame member sizes. Increasing the dead load on the CRBF columns decreases the service life economic loss of the buildings, and its effect is amplified for taller buildings. Increasing the dead load decreases the $E(L_{50yr})$ more than $E(L_{50yr})+C_{CRBF}$, as increasing dead load leads to an increase in the weight of the building. The other parameters do not a have significant effect on $E(L_{50yr})$.
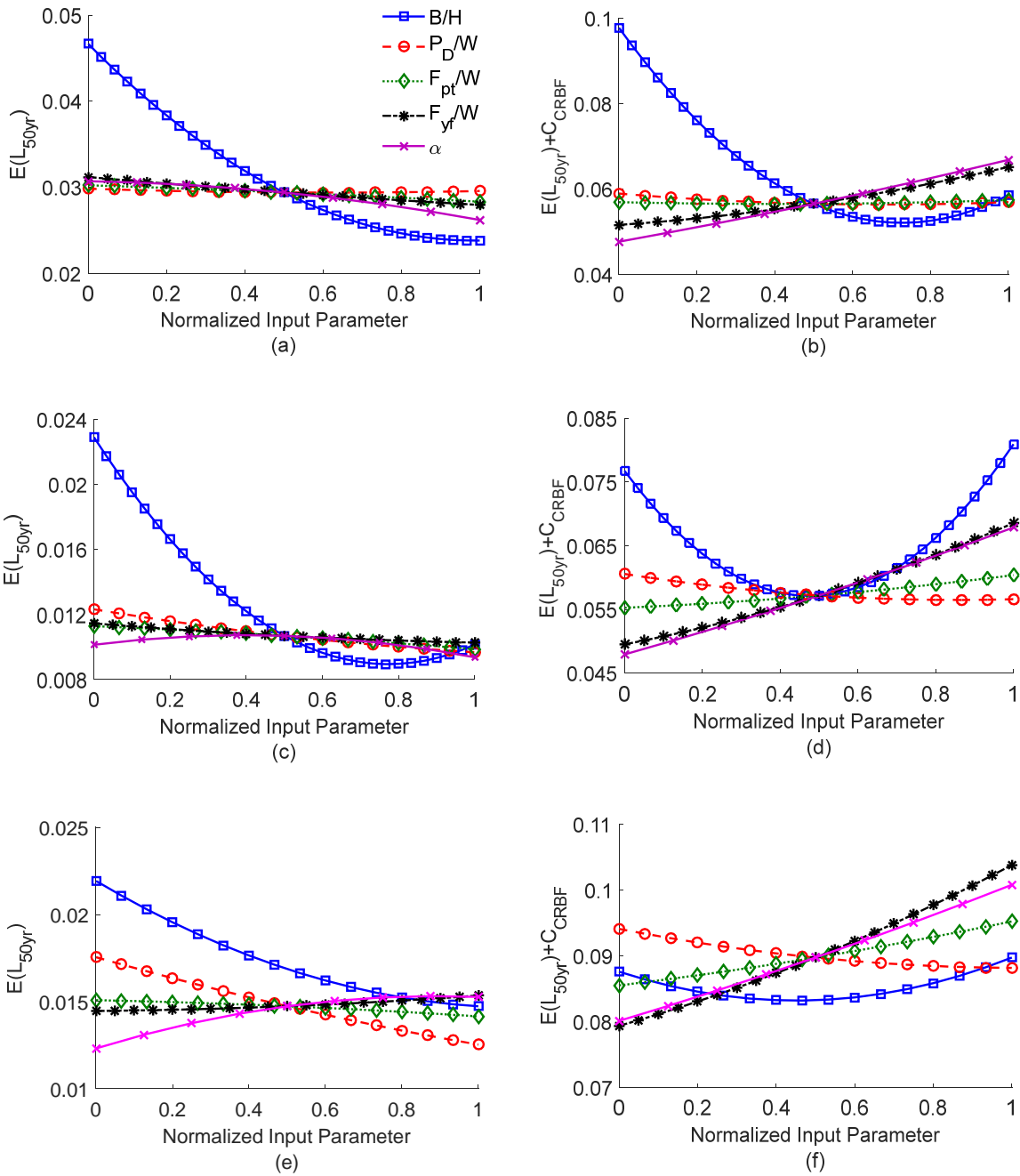
Figure 8.18. Sensitivity of impact metrics to individual structural variations: (a,b) $E(L_{50yr})$ and $E(L_{50yr})+C_{CRBF}$ of 3-story, (c,d) $E(L_{50yr})$ and $E(L_{50yr})+C_{CRBF}$ of 6-story, and (e,f) $E(L_{50yr})$ and $E(L_{50yr})+C_{CRBF}$ of 9-story

Figures 8.19 and 8.20 show the effect of the input parameters on environmental impacts (energy consumption and greenhouse gas emissions). The effect of the input parameters on environmental impacts of the buildings are the same as economic loss. Similar to the economic

loss, by increasing the height of the building, the minimum environmental impacts occurs at a lower B/H. Also, for the same building height, the minimum $E(Energy_{50yr})+Energy$ and $E(GWP_{50yr})+CO_2$ occur at lower B/H than $E(Energy_{50yr})$ and $E(GWP_{50yr})$ respectively. The B/H corresponding to the minimum $E(Energy_{50yr})$ is 0.5, 0.45, 0.35 for 3-story, 6-story, and 9-story cases, respectively, and the minimum $E(Energy_{50yr})+Energy$ is 0.43, 0.35, and 0.28 for 3-story, 6-story, and 9-story cases, respectively. The B/H corresponding to the minimum $E(GWP_{50yr})$ is 0.5, 0.45, 0.35 for 3-story, 6-story, and 9-story models respectively, and minimum $E(GWP_{50yr})+CO_2$ is 0.46, 0.38, and 0.31 for 3-story, 6-story, and 9-story models respectively. Increasing the dead loads decreases the environmental impacts.

The differences in the effect of the aspect ratio on the aggregated earthquake-induced impacts (economic loss and environmental impacts) can be explained by comparing the effect of the DS-NS and AS-NS components on service-life impacts. Figures 8.21 and 8.22 show that, while the impact of the DS-NS components decreases with increasing B/H, the opposite is true for the impacts caused by AS-NS components. Generally, a larger aspect ratio will increase the strength and stiffness of a rocking system, which will lead to higher floor acceleration demands. It is therefore not surprising that the expected service-life impacts caused by damage to AS-NS components increases with the CRSBF aspect ratio. The figures show that for the 9-story buildings, the minimum of DS-NS impacts occurred at B/H=0.43, 0.38 for economic loss ($E(L_{50yr})$) and environmental impacts ($E(Energy_{50yr})$ and $E(GWP_{50yr})$), which as noted earlier, results in a bay width larger than 40ft, which is not reasonable.
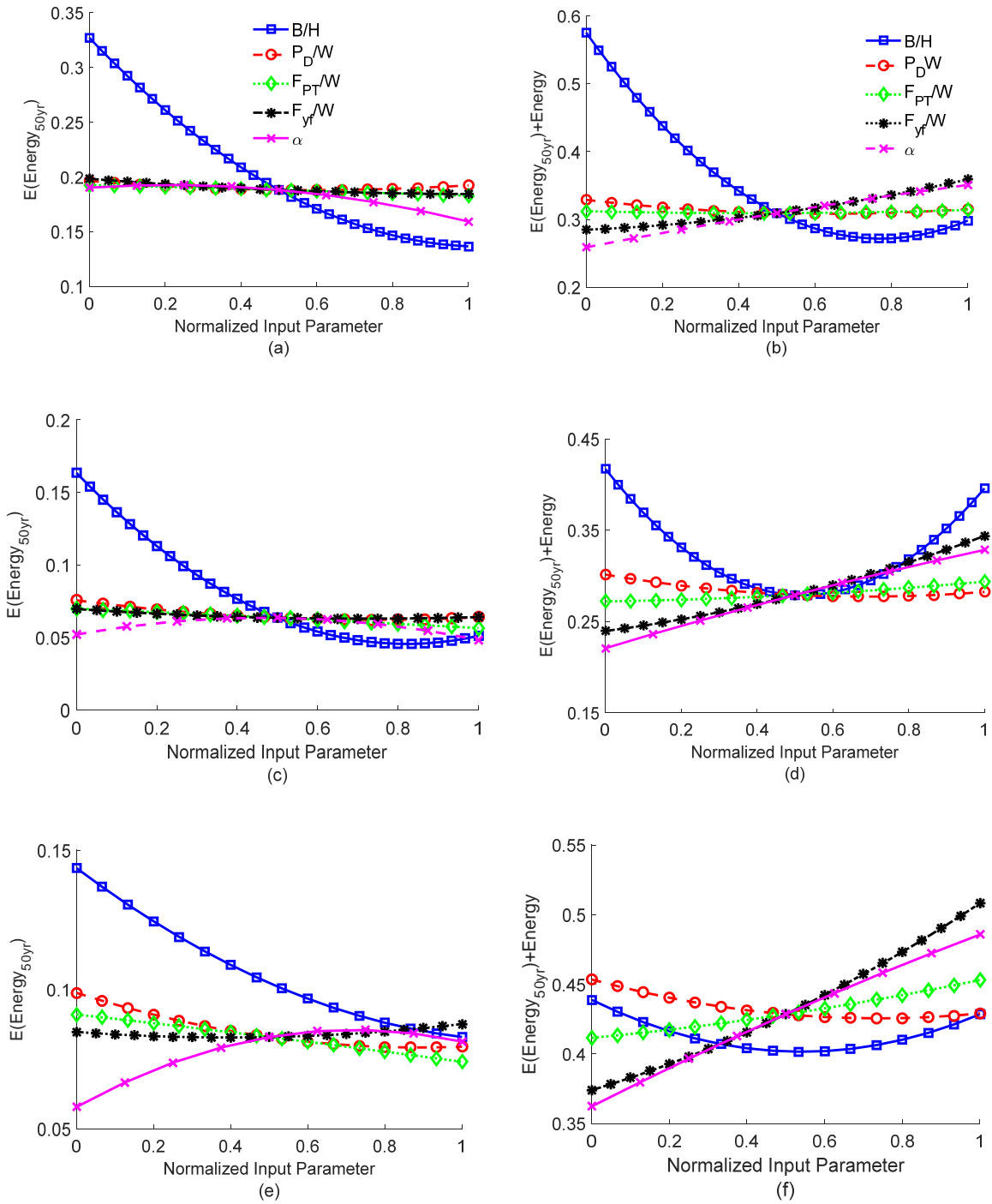
Figure 8.19. Sensitivity of the impact metrics to individual structural parameter variations: (a,b) E(Energy$_{50yr}$) and E(Energy$_{50yr}$)+Energy of 3-story, (c,d) E(Energy$_{50yr}$) and E(Energy$_{50yr}$)+Energy of 6-story, and (e,f) E(Energy$_{50yr}$) and E(Energy$_{50yr}$)+Energy of 9-story

135
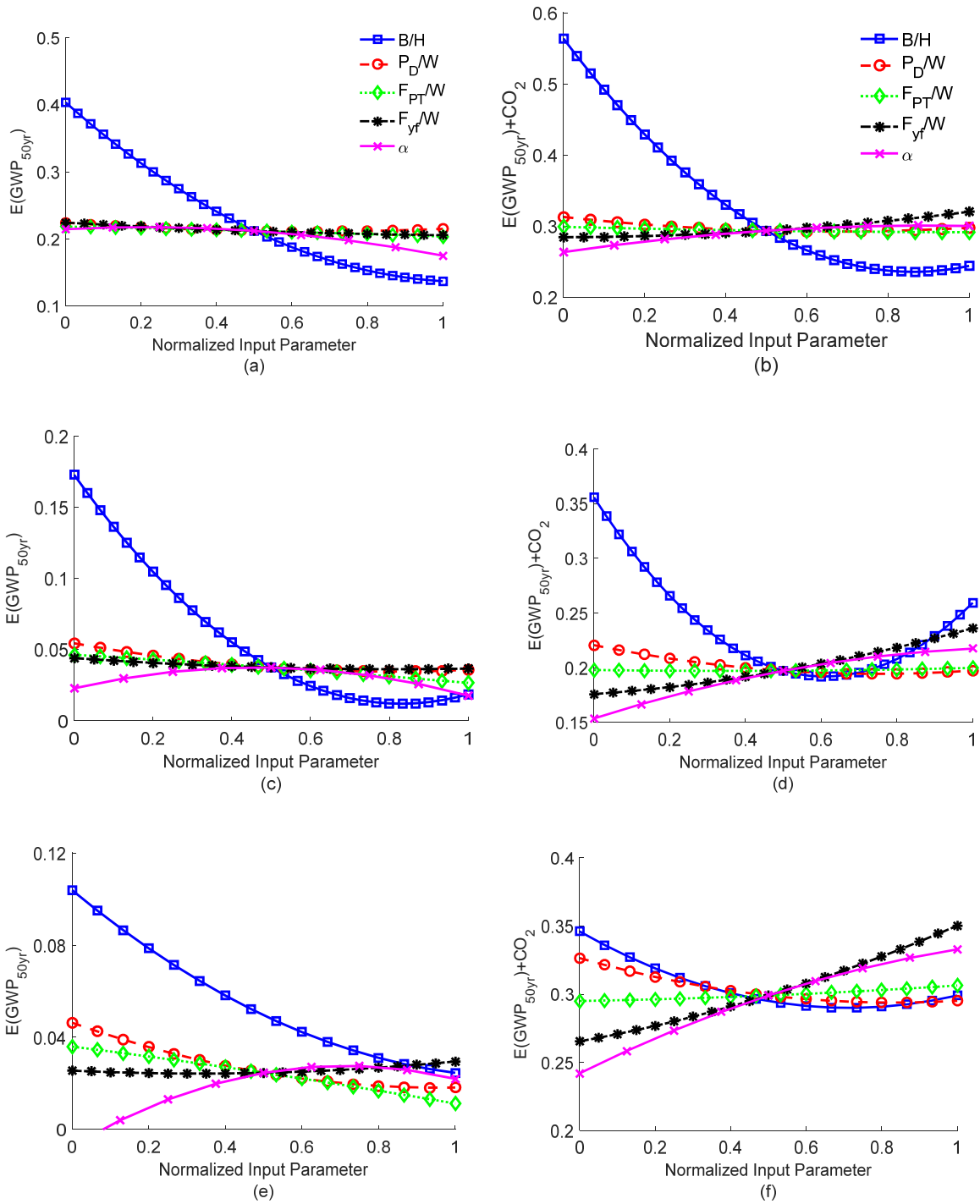
Figure 8.20. Sensitivity of the impact metrics to individual structural parameter variations: (a,b) $E(GWP_{50yr})$ and $E(GWP_{50yr}) +CO_2$ of 3-story, (c,d) $E(GWP_{50yr})$ and $E(CO_{2,50yr})$ $+CO_2$of 6-story, and (e,f) $E(GWP_{50yr})$ and $E(GWP_{50yr}) +CO_2$ of 9-story
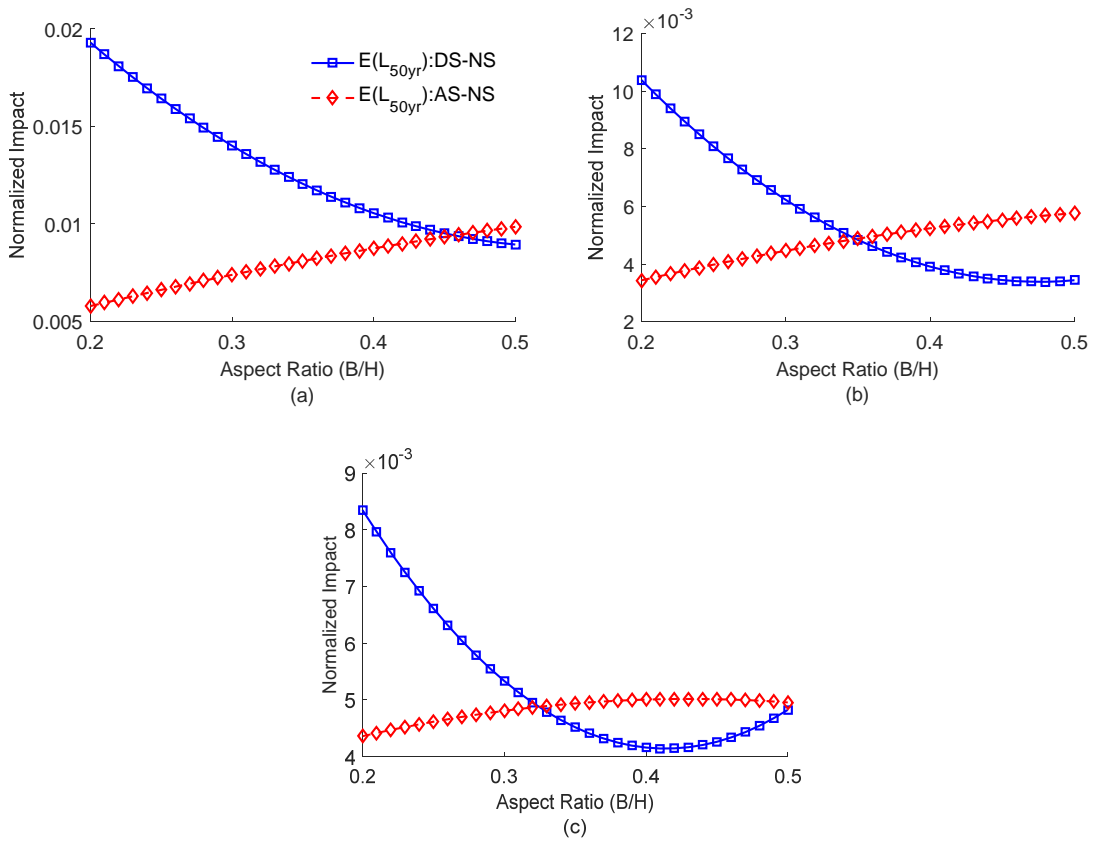
Figure 8.21. Comparing the sensitivity of the E(L$_{50yr}$) due to DS-NS and AS-NS component damage to aspect ratio variations for the (a) 3-story, (b) 6-story, and (c) 9-story buildings
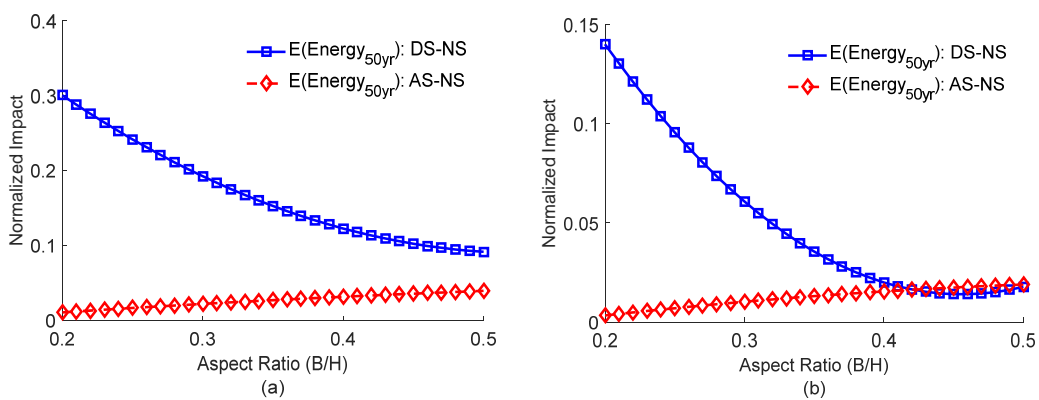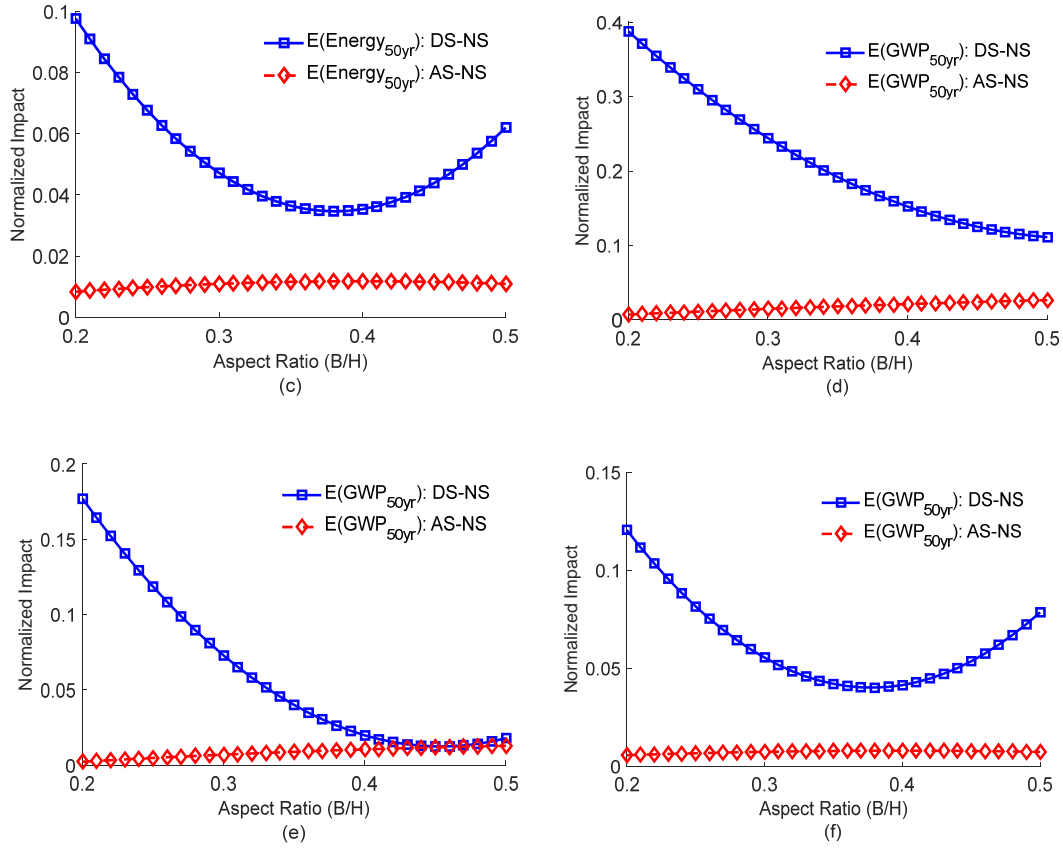
Figure 8.22. Comparing the sensitivity of E(Energy$_{50yr}$) due to DS-NS and AS-NS damage to aspect ratio variations for the (a) 3-story, (b) 6-story, and (c) 9-story buildings and the sensitivity of E(GWP$_{50yr}$) caused by DS-NS and AS-NS component damage to aspect ratio variations for (d) 3-story, (e) 6-story, and (f) 9-story buildings

8.6.   CRSBF Design Optimization

The goal of this section to obtain design parameter values that minimize the earthquake-induced impacts using the surrogate model. Solving five partial differential equations associated with Equation 8.7 for each input parameter (P_D/W, F_{pt}/W, F_{yf}/W, B/H, α) using the coefficients from the surrogate model gives the optimal design parameters.

$$\frac{dy}{dx_i} = \beta_i + \beta_{ii}x_i + \sum_{j=1}^{k} \beta_{ij}x_j \tag{8.8}$$

Both the initial construction and service-life earthquake damage impacts for the 3-story, 6-story, and 9-story buildings are used to find the optimal input parameters, which are listed in Table 8.12. The constraints on the input parameters for the optimization are defined based on the upper and lower levels (Table 5.1). The input parameters listed in Table 8.12 almost match the sensitivity results in Figures 8.18, 8.19, and 8.20.

Table 8.12. Input parameter values corresponding to the minimization of impacts

Minimize	Design parameter value for 3-story				
	P_D/W	F_{PT}/W	F_{yf}/W	B/H	α
$E(L_{50yr})$	0.2	0.3	0.5	0.47	0.06
$E(L_{50yr})+C_{CRBF}$	0.18	0.15	0.41	0.42	0.02
	Design parameter value for 6-story				
	P_D/W	F_{PT}/W	F_{yf}/W	B/H	α
$E(L_{50yr})$	0.3	0.3	0.43	0.41	0.06
$E(L_{50yr})+C_{CRBF}$	0.24	0.15	0.3	0.32	0.02
	Design parameter value for 9-story				
	P_D/W	F_{PT}/W	F_{yf}/W	B/H	α
$E(L_{50yr})$	0.3	0.3	0.3	0.35	0.02
$E(L_{50yr})+C_{CRBF}$	0.3	0.15	0.3	0.23	0.02

Minimize	Design parameter value for 3-story				
	P_D/W	F_{PT}/W	F_{yf}/W	B/H	α
$E(Energy_{50yr})$	0.22	0.3	0.48	0.5	0.06
$E(Energy_{50yr})+Energy$	0.2	0.15	0.42	0.44	0.02
	Design parameter value for 6-story				
	P_D/W	F_{PT}/W	F_{yf}/W	B/H	α
$E(Energy_{50yr})$	0.25	0.3	0.3	0.46	0.02
$E(Energy_{50yr})+Energy$	0.22	0.15	0.3	0.34	0.02
	Design parameter value for 9-story				
	P_D/W	F_{PT}/W	F_{yf}/W	B/H	α
$E(Energy_{50yr})$	0.28	0.3	0.3	0.39	0.02
$E(Energy_{50yr})+Energy$	0.27	0.15	0.3	0.26	0.02

Minimize	Design parameter value for 3-story				
	P_D/W	F_{PT}/W	F_{yf}/W	B/H	α
$E(GWP_{50\ yr})$	0.24	0.3	0.5	0.5	0.06
$E(GWP_{50\ yr})+CO_2$	0.2	0.15	0.45	0.47	0.02
	Design parameter value for 6-story				
	P_D/W	F_{PT}/W	F_{yf}/W	B/H	α
$E(GWP_{50\ yr})$	0.3	0.3	0.34	0.4	0.02
$E(GWP_{50\ yr})+CO_2$	0.23	0.15	0.34	0.38	0.02
	Design parameter value for 9-story				
	P_D/W	F_{PT}/W	F_{yf}/W	B/H	α
$E(GWP_{50\ yr})$	0.3	0.3	0.37	0.36	0.02
$E(GWP_{50\ yr})+CO_2$	0.27	0.15	0.3	0.29	0.02

8.7. Conclusion

The CRSBF service-life performance is quantified based on earthquake-induced economic losses and environmental impacts (energy consumption and greenhouse gas emissions). The optimal structural design parameter values that minimize the upfront (CRSBF only) and earthquake-induced economic and environmental impacts are determined. The considered structural design parameters include the frame aspect ratio (bay width to height ratio), *B/H*, the dead load on each column of the rocking frame, (P_D), initial post-tensioning (PT) force (F_{pt}), fuse strength (F_{yf}), fuse strain hardening ratio (α), and the number of stories in the building. Three input parameters (i.e., P_D, F_{pt}, and F_{yf}) are normalized by the tributary seismic weight (*W*). Nonlinear response history analyses (*NRHAs*) of the CRSBF are used to generate engineering demand parameters (*EDPs*). Earthquake-induced economic losses over the service life the buildings are assessed using the FEMA P58 methodology and the *EDPs* obtained from the NRHAs. The seismic performance prediction program is used to generate the damage cost ratio of building's components (damage cost over the initial cost of the components). This ratio is employed in the Athena software to assess environmental impacts (primary energy consumption and greenhouse gas emissions). The surrogate models are developed and used to establish a statistical link between the structural design parameters and economic loss, energy

consumption, and greenhouse gas emissions. For the intensity-based assessments (i.e. impacts conditioned on ground motion intensity level), at low intensity levels (less than DBE level), where the seismic hazard level is highest, drift sensitive non-structural components (DS-NS) had the greatest influence on economic losses for the 3-story buildings, but for 6-story and 9-story cases, the acceleration sensitive non-structural components (AS-NS) sometimes had the highest contribution. For higher intensities (more than DBE), the residual drift (demolition) dominated the economic loss. Drift sensitive non-structural components (DS-NS) had the greatest influence on both environmental impacts for all buildings at low intensities. For higher intensities drift sensitive non-structural components (DS-NS) had the highest effect on environmental impacts (similar to low intensities) in the 3-story and 6-story buildings, while demolition dominated environmental impacts in the 9-story buildings at higher intensities. For intensities less than the MCE level, structural components, DS-NS, and AS-NS have the largest contribution to earthquake loss and environmental impact in 3-story building compared to 6-story and 9-story buildings. However, for higher intensities (larger than MCE), the aforementioned components (structural, DS-NS, and AS-NS) have a greater effect on the 6-story compared to the 3-story and 9-story buildings. On the other hand, demolition and collapse have the smallest contribution in the 6-story buildings across all intensities.

Normalized earthquake-induced economic losses ($E(L_{50yr})$) ranging between 2.0% to 6.6%, 0.8% to 3.5%, and 1.2% to 2.95% for the 3-story, 6-story, and 9-story buildings, respectively, are obtained. The normalized service life energy consumption, $E(Energy_{50yr})$ ranges between 9.5% to 42%, 3% to 18%, and 4% to 16% for the 3-story, 6-story, and 9-story buildings, respectively. The normalized service life greenhouse gas emission, $E(GWP_{50yr})$ ranges between 9.5% to 53% , 2.6% to 21%, and 3.4% to 20% for 3-story, 6-story, and 9-story buildings, respectively. Therefore, CO_2 emissions over a 50-year service-life is more sensitive to the selected CRSBF design parameters. There was also a higher variation in economic loss and

environmental impacts in taller buildings. Economic loss and environmental impacts over a 50-year service-life of the 3-story buildings are larger than the 6-story and 9-story buildings with the same input parameters.

Surrogate models have been established to predict service-life economic loss and environmental impacts with the initial impact of the CRSBF based on the design input parameters. Among the considered structural design parameters, *B/H* has the largest influence on all the considered impacts. By increasing the building height, the effects of P_D/W and α on $E(L_{50yr})$, $E(Energy_{50yr})$, and $E(GWP_{50yr})$ are amplified with negative and positive correlation, respectively. F_{yf}/W and F_{PT}/W have the smallest effect even on 9-story models. P_D/W and F_{PT}/W have smallest effect on $E(L_{50yr})+C_{CRBF}$, $E(Energy_{50yr})+Energy$, and $E(GWP_{50yr})+CO_2$, while F_{yf}/W and α have largest influence on $E(L_{50yr})+C_{CRBF}$, $E(Energy_{50yr})+Energy$, and $E(GWP_{50yr})+CO_2$ with positive correlation. In addition, by increasing the aspect ratio, the losses due to DS-NS are decreasing while the losses due to AS-NS are increasing. The optimal values of five design key parameters for individually minimizing the aggregated (CRSBF initial plus building service-life) economic and environmental impacts was found to vary by building height.

CHAPTER 9:   Conclusion, Limitations, and Future Work

9.1. Overview

Many studies within the last two decades have sought to improve the security and resilience of the buildings to ensure that they can continue the primary functions (e.g., self-shelter and critical operations) after sever earthquake. Much of that research has focused on developing resilient building systems, which reduce structural damage, repair costs, and downtime after a major earthquake. Controlled rocking steel braced frames are one of the building systems which enhance the seismic performance through its self-centering capabilities and the ability to limit the structural damage to easily replaceable elements. The main components of the controlled rocking braced frame are the vertical post-tensioning cables which provides the self-centering capability and the fuse elements, which serve to dissipate the energy and minimize peak displacement through inelastic deformation.

A number of studies have been carried out to develop rocking steel braced frames with post-tensioning rods and replaceable fuses. However, comparatively much less has been accomplished in formulating performance-based design and assessment methods that can be used by practicing engineers to implement these systems in real buildings and quantify their benefits with regards to life cycle costs and sustainability. The focus of this study is investigating the seismic performance of the controlled rocking steel braced frames and providing methods for predicting the behavior of the CRSBFs during an earthquake. More specifically, the issues that addressed in this study can be summarized as follows.

- Establish links between the design key parameters of the CRSBF and maximum engineering demand parameters (EDPs) through statistical modeling (Chapter 5).

- Investigating the effect of force-controlled components failure on the performance of the CRSBF and develop a methodology for determining load and resistance factors that are consistent with system level performance objectives (Chapter 6)
- Quantifying the effect of modeling uncertainty on the seismic performance of the controlled rocking braced frames (Chapter 7)
- Evaluating the seismic performance of CRSBFs on earthquake-induced economic loss and environmental effect (energy consumption and greenhouse gas emission) over the service life of the building (Chapter 8).

9.2. Findings

9.2.1. Chapter 5: Estimating Maximum Engineering Demand Parameters (EDPs) of Controlled Rocking Steel Braced Frames

In this chapter, a set of statistical equations are proposed for estimating the maximum story drift ratio, maximum peak floor acceleration, and residual drift of controlled rocking steel braced frames. The input variables of proposed equations are five design key parameters and the spectral acceleration at an effective period (equivalent SDOF). The proposed equations demonstrated a reasonable accuracy to predict maximum story drift ratio and peak floor acceleration. The predictive performance for the residual story drift ratio was not as adequate.

9.2.2. Chapter 6: Reliability-Based Design of Force-Controlled Components in Rocking Steel Braced Frames

In this chapter, the effect of force-controlled component failure on the collapse and unsafe placard trigger (UPT) limit states was investigated. It was demonstrated that the effect of column failure is more significant compared to the beams and braces in 3-story buildings. However, brace failure had largest impact for the 6-story building and force-controlled

components did not have a significant effect on collapse performance of 9-story building. The effect of force-controlled components failure on collapse assessment is greater than the unsafe placard trigger limit state. The displacement-controlled components (fuse and PT) were found to be much more likely to trigger an unsafe placard. For both limit states, the effect of force-controlled component failure was found to be lower for taller buildings. The effect of various values of the resistance to load factor ration $\frac{\phi}{\gamma} = 0.9, 1.2, 1.5$ and 1.8, were studied on the 50-year collapse and unsafe placard trigger.

It was found that increasing $\frac{\phi}{\gamma}$ to 1.8, the probability of 50-year collapse remained below the 1% threshold prescribed by current building codes.

9.2.3. Chapter 7: Effect of Model Uncertainty on Multi-Limit State Performance Assessment of Controlled Rocking Steel Braced Frames

The main focus of this chapter was on evaluating the influence of structural model parameter uncertainty on the seismic response and limit state assessment of controlled rocking braced frames (CRSBFs). Three limit states were considered including immediate occupancy (IO), repairability (RP) and collapse prevention (CP) performance. The effect of modeling uncertainty was also studied on four engineering demand parameters, (maximum transient (SDR_{max}) and residual story drift ratio (RDR_{max}), the PT strain (ε_{PT}), and the fuse shear deformation (γ_{fuse})). The record-to-record dispersion of SDR_{max} was found to be comparable across the different building cases, and the effect of modeling uncertainty on the SDR_{max} dispersion in the 3- and 6-story buildings was found to be negligible, however for the 9-story building, modeling uncertainty increased the log-standard deviation of SDR_{max} by about 8%. The 95% confidence interval (CI) for RDR_{max}, ε_{PT}, and γ_{fuse} decreased as the building height

145

increased. Modeling uncertainty had the largest impact on the RDR_{max} dispersion compared to other *EDPs*, increasing the log-standard deviation by a maximum of 20%. For ε_{PT}, and γ_{fuse}, modeling uncertainty increased the log-standard deviation by as much as 7%. In addition, modeling uncertainty had the greatest effect on the *RP* limit state fragility properties of the 9-story, increasing the median and dispersion by 17% and 33% respectively. Moreover, modeling uncertainty increased the probability of limit state exceedance in 50 years by 10%, and 30% for the 6-story and 9-story buildings, respectively.

9.2.4. Chapter 8: Earthquake-Induced Impacts of Controlled Rocking Braced Frames

Economic loss and environmental impacts of CRSBFs are assessed in this chapter. Environmental impacts are based on energy consumption and greenhouse gas emissions. Six design key parameters (*B/H, P_D, F_pt, F_yf,* and *α*) are considered for 3-story, 6-story, and 9-story design cases. The effect of collapse, demolition, structural component and drift sensitive nonstructural (DS-NS) and acceleration sensitive (AS-NS) component damage on intensity-based and 50-year service life losses are studied. It was found that, at lower intensities, the effect of the DS-NS components is largest for shorter building, whereas AS-NS components have the greatest effect the economic losses in taller buildings. However, at low intensity levels, damage to DS-NS components had the largest influence on environmental impacts for all the buildings. At higher intensities, demolition contributes the most to economic loss for all buildings. However for environmental impacts, damage to the DS-NS components have the largest effect whereas demolition dominates for the 9-story building. Earthquake-induced economic loss over a 50-year service-life are lager for the 3-story design cases compared to the 6-story and 9-story buildings with the same input parameters. Surrogate models are proposed and used to establish a statistical link between the structural design parameters and

economic loss, energy consumption, and greenhouse gas emissions over a 50-year service-life. The effect of each key design parameters on earthquake-induced impacts are also investigated. It was found that the aspect ratio has the greatest influence on economic loss and environmental impacts. In addition, the design key parameters are optimized to minimize the earthquake-induced impacts for the CRSBF system over a 50-year service life.

9.3.   Limitations and Future Work

The research presented in this dissertation is focused on developing performance-based design and assessment methods for CRSBFs. All of the studies that used as the basis for this work were based on building cases that range from 3 to 9 stories. As such, it would be difficult to generalize the findings for taller (e.g. 10-stories or more) CRSBFs. This is especially true for the predictive models developed to estimate the structural response demands and life cycle impacts. More studies are needed utilizing taller CRSBFs to expand the applicability of the surrogate models. Additionally, only two sets of ground motions, the FEMA P695 far-field and the PEER TSRP record sets, were used throughout. Additional studies are needed to investigate the effect of specific ground motion characteristics (e.g. duration, vertical ground motions, pulse effects) on the response and performance of CRSBFs.

The periods used to design of CRSBFs and also link the building seismic response and site seismic hazard are based on the spectral acceleration at first-mode periods of the buildings, which may not represent the actual period of rocking systems. The intensity measures that are used in Chapter 6 are also primarily based on the first-mode period of the buildings. In Chapters 5 and 8 the effective period obtained from the proposed method in Chapter 5 from SDOF properties are used, which may not represent the actual period of the structure specially for the taller buildings where the rigid-body rotation behavior assumption may not hold. As discussed in Chapter 5, as the period range of the considered buildings increases (e.g. if both low- and

high-rise buildings are considered), it may be necessary to select multiple sets of hazard-consistent ground motions. Lastly, there is also a need to investigate the effect of other types of model uncertainty (e.g. the chosen constitutive model and the associated parameters) on the performance of CRSBFs.

Only one type of CRSBF configuration (single bay rocking frame with PT and fuse mid-bay ground floor) was considered in the current study. As such, it is unclear that the current findings can be extended to other configurations (e.g. PT at columns, fuses along building height). Future studies can be used to investigate whether the methods and findings from the current study can be extended to other CRSBF configurations. Lastly, only one type of fuse, the butterfly shear link, was considered in the current study. However, other types of fuse assemblies such as buckling restrained braces have been used for CRSBF. Additional studies are needed to determine whether or not the findings from this research agnostic to the type of fuse employed in the CRSBF.

The performance metrics considered in the service life impact assessments in Chapter 8 include earthquake induced economic losses and environmental impacts. Additional studies are needed that include more resilience-related metrics (e.g. functional loss and/or functional recovery) and to understand the implications of different design parameters on the performance outcome of CRSBFs in terms of these metrics.

References

AISC (2017). *American Institute of Steel Construction Manual*. Fifteenth Edition, American Institute of Steel Construction, United States of America.

ASCE/SEI. (2016). *Minimum design loads and associated criteria for buildings and other structures ASCE/SEI 7-16*. Reston, VA.

Aslani, H., and Miranda, E. (2005). "Probability-based seismic response analysis." *Engineering Structures*, 27(8), 1151-1163

Athena. (2014). "The Athena impact estimator." ⟨http://www.athenasmi.org/our-software data/impact-estimator/⟩.

Baker, J. W. (2015). "Efficient analytical fragility function fitting using dynamic structural analysis." *Earthquake Spectra*, 31(1), 579-599.

Baker JW, Lin T, Shahi SK. (2011). "New ground motion selection procedures and selected motions for the PEER transportation research program." *PEER Report* 3011/03, Pacific Earthquake Engineering Research Center, University of California, Berkeley.

Baltzopoulos, G., Iervolino, I., and Baraschino, R. (2019). "Ground motion sample size vs estimation uncertainty in seismic risk". Conference: 13th International Conference on Applications of Statistics and Probability in Civil Engineering (ICASP13)

Baltzopoulos, G., Baraschino, R., and Iervolino, I. (2019). "On the number of records for structural risk estimation in PBEE". *Earthquake Engng Struct Dyn.*; 48: 489– 506. https://doi.org/10.1002/eqe.3145

Bradley, Brendon A. (2010). "A generalized conditional intensity measure approach and holistic ground-motion selection." *Earthquake Engng. Struct. Dyn.*, 39(12), 1321- 1342.

Bradley, Brendon A. (2013). "A critical examination of seismic response uncertainty analysis in earthquake engineering". *Earthquake Engineering & Structural Dynamics*, 42(11), 1717-1729.

Browning, J., Li, Y., Lynn, A., & Moehle, J. (2000). "Performance Assessment for a Reinforced Concrete Frame Building". *Earthquake Spectra, 16*, 541 - 555.

Campbell, K.W. and Bozorgnia, Y. (2014). "NGA-West2 ground motion model for the average horizontal components of PGA, PGV, and 5% damped linear acceleration response spectra". *Earthquake Spectra*. **30**(3): p. 1087-1115.

Celik, Ozan Cem, & Ellingwood, Bruce R. (2010). "Seismic fragilities for non-ductile reinforced concrete frames Role of aleatoric and epistemic uncertainties." *Structural Safety*, 32(1), 1-12.

Christopoulos, C., Filiatrault, A. and Folz, B. (2002). "Seismic response of self-centring hysteretic SDOF systems." *Earthquake Engng. Struct. Dyn.*, 31: 1131-1150.

Christopoulos, C., Pampanin, S and Priestley, m.j. (2003). "Performance-based seismic response of frame structures including residual deformations. Part I: Single-degree of freedom systems." *J EARTHQU ENG*. 7. 97-118. 10.1080/13632460309350443.

Clough, R. W. and Huckelbridge, A. A. (1977). "Preliminary Experimental Study of Seismic Uplift of a Steel Frame." Earthquake Engineering Research Center, Report NO. UCB/EERC-77122.

Dolsek, M. (2009). "Incremental dynamic analysis with consideration of modeling uncertainties." *Earthquake Engineering & Structural Dynamics*, 38(6), 805(825).

Dyanati, M., Huang, Q., & Roke, D. (2017). "Cost-benefit evaluation of self-centering concentrically braced frames considering uncertainties." *Structure and Infrastructure Engineering*, 13(5), 537–553.

Eatherton, M. and Hajjar, J. (2010). "Large-scale cyclic and hybrid simulation testing and development of a controlled-rocking steel building system with replaceable fuses." NSEL-025, Department of Civil and Environmental Engineering, University of Illinois at Urbana-Champaign.

Eatherton, M., and Hajjar, J. (2011). "Residual drifts of self-centering systems including effects of ambient building resistance." *Earthquake Spectra*, 27(3), 719–744.

Eatherton, M., Ma, X., and Krawinkler, H. et al. (2014). "Design concepts for controlled rocking of self-centering steel-braced frames." *J. Struct. Eng.,* 140:4014082.

Feese, C., Li, Y., and Bulleit, W. (2014). "Assessment of Seismic Damage of Buildings and Related Environmental Impacts." *Journal of Performance of Constructed Facilities*. 29. 04014106. 10.1061/(ASCE)CF.1943-5509.0000584.

Fell, B.V., Kanvinde, A.M., Deierlein, G.G., Myers, A.T, and Fu, X. (2006). "Buckling and fracture of concentric braces under inelastic cyclic loading." *SteelTips Series*, Structural Steel Education Council, Moraga, CA.

FEMA (Federal Emergency Management Agency) (2009). "Quantification of building seismic performance factors". FEMA P695. Redwood City, CA

FEMA (Federal Emergency Management Agency) (2012). "Seismic performance assessment of buildings". FEMA P-58, Volumes 1 and 2. Redwood City, CA

Galambos, T.V., Ellingwood, B., MacGregor, J.G. and Cornell, C.A. (1982). "Probability-Based Load Criteria: Assessment of Current Practice." *Journal of the Struct.Division*, ASCE 108 (ST5), pp. 959-977.

Gehl, P., Douglas, J., and Seyedi, DM.(2015). "Influence of the number of dynamic analyses on the accuracy of structural response estimates". *Earthq Spectra*.;31(1):97-113.

Gulkan P, Sozen M. (1974). "Inelastic response of reinforced concrete structures to earthquakes motions." *ACI Journal*; 71:604–610.

Gupta, A., and Krawinkler, H. (1999). "Seismic demands for the performance evaluation of steel moment resisting frame structures." Stanford University, Stanford, CA.

Gokkaya, B, U. (2015). "Seismic Reliability Assessment of Structures Incorporating Modeling Uncertainty and Implications for Seismic Collapse Safety." Stanford University. Civil & Environmental Engineering Department.

Hall, KS., Eatherton, MR., and Hajjar, JF. (2010). "Nonlinear behavior of controlled rocking steel-framed building systems with replaceable energy dissipating fuses." Newmark Structural Engineering Laboratory. University of Illinois at Urbana-Champaign.

Haselton, Curt. (2006). "Assessing Seismic Collapse Safety of Modern Reinforced Concrete Moment Frame Buildings." Dept. of Civil and Environmental Engineering. Stanford, CA: Stanford University.

Helton, J.C. and Davis F.J. (2003). "Latin hypercube sampling and the propagation of uncertainty in analyses of complex systems". *Reliability Engineering & System Safety*; **81**(1):23–69.

Housner, George W. (1963) . *"*The behavior of inverted pendulum structures during earthquakes". Bulletin of the Seismological Society of America, 53 (2). pp. 403-417. ISSN 0037-1106.

Hwang, S.-H., and Lignos, D. G. (2017). "Earthquake-induced loss assessment of steel frame buildings with special moment frames designed in highly seismic regions". *Earthquake Engng Struct. Dyn.*, 46: 2141– 2162. doi: 10.1002/eqe.2898.

Ibarra, Luis F., & Krawinkler, H. (2005). "Global collapse of frame structures under seismic excitations." Tech. rept. John A. Blume Earthquake Engineering Center, Stanford, CA.

Iwan WD. (1980). "Estimating inelastic response spectra from elastic spectra." *Earthquake Engineering and Structural Dynamics*; 8:375–388.

Iwashita, K., Kimura., H., Kasuga., Y., and Suzuki, N. (2002). "Shaking table test of a steel frame allowing uplift." *Journal of Structural and Construction Engineering* (Transactions of AIJ) 561(561):47-54

Jayaram, N., Lin, T., & Baker, Jack W. (2011). "A Computationally Effcient Ground-Motion Selection Algorithm for Matching a Target Response Spectrum Mean and Variance." *Earthquake Spectra*, 27(3), 797-815.

Joó A, Zsarnoczay A, Opoldusz M, Kollar L. (2017). " Applicability of modal response spectrum analysis on rocking structures." 16th World conference on earthquake engineering, Santiago, Chile.

Kowalsky MJ. (1994). "Displacement-based design-a methodology for seismic design applied to RC bridge columns." Master's Thesis, University of California at San Diego, La Jolla, California.

Lee, T., & Mosalam, Khalid M. (2005). "Seismic demand sensitivity of reinforced concrete shear-wall building using FOSM method." *Earthquake Engineering & Structural Dynamics*, 34(14), 1719-1736.

Lee, J. Y., & Ellingwood, B. R. (2015). "Ethical discounting for civil infrastructure decisions extending over multiple generations." *Structural Safety*, 57, 43–52.

Liel, Abbie B., Haselton, Curt B., Deierlein, Greg G., & Baker, Jack W. (2009). "Incorporating modeling uncertainties in the assessment of seismic collapse risk of buildings." *Structural Safety*, 31(2), 197-211.

Liu, J. (2003), "Examination of Expected Yield and Tensile Strength Ratios," Draft Addendum Report, AISC, Chicago, IL.

Ma, X., Krawinkler, H., and Deierlein, G., G. (2011). "Seismic design and behavior of self-centering braced frame with controlled rocking and energy dissipating fuses." John Blume Earthquake Engineering Center, TR 174, Stanford, CA.

Makris, N., and Konstantinidis, D. (2003). "The rocking spectrum and the limitations of practical design methodologies." *Earthquake Engineering & Structural Dynamics*. 32.

Martin, A., Deierlein, G., and Ma, X. (2018). "Capacity Design Procedure for Rocking Braced Frames Using the Modified Modal Superposition." *J. Struct. Eng*., 145. 10.1061/(ASCE)ST.1943-541X.0002329.

McKay, M., Beckman, R., & Conover, W. (1979). "A Comparison of Three Methods for Selecting Values of Input Variables in the Analysis of Output from a Computer Code". *Technometrics*, 21(2), 239-245. doi:10.2307/1268522

McKenna, F.T. (1999). "Object-oriented finite element programming: Frameworks for analysis, algorithms and parallel computing." PhD thesis, University of California, Berkeley, CA.

Midorikawa1, M., Azuhata, T., Ishihara, T., and Wada, A. (2006). "Shaking table tests on seismic response of steel braced frames with column uplift." *Earthquake Engng Struct. Dyn*; 35:1767–1785.

Miranda, Eduardo. (2000). "Inelastic Displacement Ratios for Structures on Firm Sites." *Journal of Structural Engineering-ASCE - J STRUCT ENG-ASCE*. 126. 10.1061/(ASCE)0733-9445(2000)126:10(1150).

Miranda, E. and Ruiz-García, J. (2002). "Evaluation of approximate methods to estimate maximum inelastic displacement demands." *Earthquake Engng. Struct. Dyn*., 31: 539-560. doi:10.1002/eqe.143

Ruiz-Garcia, Jorge & Miranda, Eduardo. (2007). "Probabilistic estimation of maximum inelastic displacement demands for performance-based design." *Earthquake Engineering & Structural Dynamics*. 36. 1235 - 1254. 10.1002/eqe.680.

Moradi, S., and Burton, H. V. (2018). "Response surface analysis and optimization of controlled rocking steel braced frames." *Earthq. Eng*. pp. 24-31.

Moradi, S., Burton, H. V., and Kumar, I. (2018). "Parameterized Fragility Functions for Controlled Rocking Steel Braced Frames." *Engineering Structures*. 176. 254-264. 10.1016/j.engstruct.2018.09.001.

Newmark NM, Hall WJ.(1982). *Earthquake Spectra and Design*. Earthquake Engineering Research Institute, Berkeley, CA, 1982.

Christopoulos, C., and Pampanin, S. (2004). "Towards Performance-based seismic design of MDOF structures with explicit consideration of residual deformations." http://home.iitk.ac.in/~vinaykg/issue14.html. 41.

Pollino, M., and Bruneau, M. (2008). "Seismic Testing of a Bridge Steel Truss Pier Designed for Controlled Rocking." *Journal of Structural Engineering*, Vol. 136, No. 12.

Porter, Keith A., Beck, James L., & Shaikhutdinov, Rustem V. (2002b). "Sensitivity of Building Loss Estimates to Major Uncertain Variables." *Earthquake Spectra*, 18(4), 719-743.

Priestley, M.J.N., Evison, R.J., and Carr, A.J. (1978). "Seismic response of structures free to rock on their foundation." Bulletin of the New Zealand National Society for Earthquake Engineering 11(3):141-150.

Rahgozar N, Moghadam AS, Aziminejad A. (2016). " Quantification of seismic performance factors for self-centering controlled rocking special concentrically braced frame." *The Structural Design of Tall and Special Buildings*; 25(14):700–723.

Rahgozar N, Moghadam AS, Aziminejad A. (2016). " Inelastic displacement ratios of fully selfcentering controlled rocking systems subjected to near-source pulse-like ground motions." *Eng Struct*;108:113–33.

Ramirez, C. M., & Miranda, E. (2012). "Significance of residual drifts in building earthquake loss estimation". *Earthquake Engineering & Structural Dynamics*, 41(11), 1477-1493.

Rathje, Ellen M., Kottke, Albert R., & Trent, Whitney L. (2010). "Influence of Input Motion and Site Property Variabilities on Seismic Site Response Analysis." *J. Geotech. and Geoenvir. Engrg*., 136(4), 607-619.

Roke, D., Sause, Ricles, J.M., and Chancellor, N.B. (2010). "Damage-free seismic resistant self-centering concentrically-braced frames." Report 10-09, Advanced Technology for Large Structural Systems Engineering Research Center: Bethlehem, PA.

Rosenblueth E, Herrera I. (1964). "On a kind of hysteretic damping." *Journal of Engineering Mechanics Division ASCE*; 90:37– 48.

Ruiz-Garcia, Jorge & Miranda, Eduardo. (2003). "Inelastic displacement ratios for evaluation of existing structures." *Earthquake Engineering & Structural Dynamics*. 32. 1237 - 1258. 10.1002/eqe.271.

Ruiz-Garcia, Jorge & Miranda, Eduardo. (2006). "Inelastic displacement ratios for evaluation of structures built on soft soil sites*." Earthquake Engineering & Structural Dynamics*. 35. 679-694. 10.1002/eqe.552.

Seo, C and Sause, R.. (2005). "Ductility demands on self-centering systems under earthquake loading." *ACI Structural Journal*. 102. 275-285.

Steele, T.C., and Wiebe, L. (2016). "Dynamic and equivalent static procedures for capacity design of controlled rocking steel braced frames." *Earthquake Engng Struct. Dyn*. DOI: 10.1002/eqe.2765

Steele, T.C., and Wiebe, L.D.A. (2017). "Collapse risk of controlled rocking steel braced frames with different post-tensioning and energy dissipation designs." *Earthquake Eng. Struct. Dyn*.

Sun, H., Burton, H. V., Zhang, Y., &Wallace, J.W. (2017). "Interbuilding interpolation of peak seismic response demands using spatially correlated demand parameters". *Earthquake Engineering Structural Dynamics*, 47(5), 1168–1188.

Tremblay, R.,Poirier, P.,Bouaanani, N., Leclerc4, M.,Rene,V., Fronteddu, L.,and Rivest, S.(2008). "Innovative Viscously Damped Rocking Braced Steel Frames." The 14th World Conference on Earthquake Engineering.

Uriz, P. (2005). "Towards earthquake resistant design of concentrically braced steel structures." Ph.D. dissertation, Dept. of Civil and Environmental Engineering, Univ. of California, Berkeley, CA.

Uriz, P., Filippou, F. C., and Mahin, S.A. (2008). "Model for Cyclic Inelastic Buckling of Steel Braces." *J. Struct. Eng* 134(4).

Vamvatsikos, D., and Fragiadakis, M. (2010). "Incremental dynamic analysis for estimating seismic performance sensitivity and uncertainty." *Earthquake engineering & structural dynamics,* 39(2), 141(163).

Victorsson, V.K., Deierlein, G.G., Baker, J.W., and Krawinkler, H. (2011). "The Reliability of Capacity-Designed Components in Seismic Resistant Systems." J.A. Blume Technical Report 177, Stanford University, Stanford, CA.

Vorechovsky, M., and Novak, D. (2003). "Statistical correlation in stratified sampling". In ICAPS 9 Proceedings of International Conference on Applications of Statistics and Probability in Civil Engineering, Der Kiureghian A, Madant S, Pestana JM (eds). Millpress: Rotterdam, San Francisco; 119–124.

Wada, A., Qu, Z., Ito, H., Motoyui, S., Sakata, H., and Kasai, K. (2001). "Seismic Retrofit Using Rocking Walls and Steel Dampers." ATC and SEI Conference

Wiebe, L., Christopoulos, C., Tremblay, R., and Leclerc, M. (2013). "Mechanisms to limit higher mode effects in a controlled rocking steel frame 2: Large-amplitude shake table testing." *Earthquake Engng Struct. Dyn*.

Wiebe, L., and Christopoulos, C. (2014a). "Performance-based seismic design of controlled rocking steel braced frames. II: Design of capacity-protected elements." *J. Struct. Eng*., 141 (2014) 04014227.

Wiebe, L., and Christopoulos, C. (2014b). "Performance-based seismic design of controlled rocking steel braced frames. I: Methodological framework and design of base rocking joint." *J. Struct. Eng*., 141(9):040142261–10.

Yin, Yue-Jun, & Li, Yue. (2010). "Seismic collapse risk of light-frame wood construction considering aleatoric and epistemic uncertainties". *Structural Safety*, 32(4), 250-261.

Zhang, Changxuan & Steele, Taylor & Wiebe, Lydell. (2018). "Design-level estimation of seismic displacements for self-centering SDOF systems on stiff soil." *Engineering Structures*. 117. 431-443. 10.1016/j.engstruct.2018.09.067.

Ziemian, R. D., and McGuire, W. (2007). Tutorial for MASTAN2 version 3.0, Jon Wiley & Sons, Inc.